
MASTER'S THESIS

PERFORMANCE BOUNDS FOR ANCHORLESS
COOPERATIVE INDOOR LOCALIZATION
EXPLOITING MULTIPATH

conducted at the
Signal Processing and Speech Communications Laboratory
Graz University of Technology, Austria

by
Gregor Dumphart

Supervisors:
Assoc.Prof. Dipl.-Ing. Dr. Klaus Witrissal
Dipl.-Ing. Erik Leitinger
Dipl.-Ing. Paul Meissner

Graz, March 17, 2014

Abstract

There is high demand for accurate indoor localization for use in logistic, industrial, and commercial systems. However, due to multipath propagation, localization is a difficult task in indoor environments. Available accurate solutions require costly, inflexible infrastructure in terms of several fixed physical anchors.

The multipath-assisted indoor navigation and tracking (MINT) approach assumes a known floor plan, which enables multipath-assisted localization through mapping multipath components to virtual anchors. So, cost can be saved by reducing the number of required fixed physical anchors. Cooperative MINT (Co-MINT) is an advanced, more flexible concept that allows for anchorless localization. It assumes several cooperating mobile agents equipped with ultra-wideband (UWB) transceivers that perform monostatic and bistatic measurements, share these observations, and estimate the agent positions jointly. A proof of concept has been presented in a recent work, but a quantitative assessment of the localization performance was not given.

The goal of this master thesis is to obtain a performance bound for Co-MINT. In a first step, the dependence of multipath propagation delays on the room geometry is studied to obtain a general formula for spatial delay gradients which express the influence of the indoor geometry on the localization performance. Next, the thesis analyses monostatic localization as a building block of Co-MINT. The derivation of the Cramér-Rao lower bound (CRLB) of monostatic position estimation and numerical results thereof are presented. The ranging information provided by particular monostatic multipath geometries is examined.

The final part of the thesis contains a derivation of the CRLB for Co-MINT and gives the corresponding equivalent Fisher information matrix (EFIM). Numerical results reveal characteristics of cooperation and show the behaviour of the position error bound (PEB) for several scenarios.

Kurzfassung

Es herrscht hoher Bedarf an Systemen zur präzisen Positionsbestimmung in Innenräumen, etwa in der Logistik, im industriellen Sektor und Handel sowie im Rüstungsbereich. Aufgrund von Mehrwegeausbreitung ist die Positionsbestimmung in Innenräumen allerdings ein schwieriges Unterfangen. Bestehende Lösungen von hinreichender Genauigkeit erfordern beträchtliche, starre Infrastruktur in Form von mehreren fixen Basisstationen.

Multipath-assisted Indoor Navigation and Tracking (MINT) ist ein Ansatz, der einen bekannten Grundriss des Innenraums voraussetzt. Dadurch wird mehrwegeunterstützte Positionsbestimmung ermöglicht, wobei jede Mehrwegekomponente einer virtuellen Quelle mit bekannter Position zugeordnet wird und so die Anzahl der erforderlichen Basisstationen reduziert wird. Cooperative MINT (Co-MINT) ist ein weiterführendes, noch flexibleres Konzept das ganz ohne Basisstationen auskommt. Dabei kooperieren mehrere mobile Geräte, jeweils mit einem Ultrabreitband-Transceiver ausgestattet, indem sie monostatische und bistatische Messungen durchführen und diese Messdaten austauschen um dann gemeinsam ihre Positionen zu schätzen. Ein Machbarkeitsnachweis wurde in einer kürzlich erschienenen Arbeit erbracht, eine quantitative Beurteilung der Lokalisierungsgenauigkeit wurde darin allerdings nicht angegeben.

Ziel dieser Masterarbeit ist es, eine enge Positionsfehlerschranke für Co-MINT herzuleiten. Als erster Schritt wird die Abhängigkeit der Mehrwegezeitverzögerungen von der Raumgeometrie untersucht und eine allgemeine Formel für räumliche Gradienten dieser Verzögerungen hergeleitet. Dies löst das Problem des Einflusses der Raumgeometrie auf die Lokalisierungsgenauigkeit. Ferner wird monostatische Lokalisierung als Baustein von Co-MINT beleuchtet und die Cramér-Rao-Ungleichung für diesen Fall bestimmt, sowie die Eigenschaften verschiedener Arten monostatischer Mehrwegekomponenten bezüglich ihrer Geometrie untersucht.

Der finale Teil der Arbeit widmet sich Co-MINT selbst. Die Cramér-Rao-Ungleichung sowie die äquivalente Fisher-Informationsmatrix werden für den kooperativen Fall bestimmt. Charakteristiken der Kooperation sowie das Verhalten der Positionsfehlerschranke in verschiedenen räumlichen Anordnungen werden anhand von numerischen Ergebnissen aufgezeigt.

Statutory Declaration

I declare that I have authored this thesis independently, that I have not used other than the declared sources/resources, and that I have explicitly marked all material which has been quoted either literally or by content from the used sources.

date

(signature)

Abbreviations

AoA	Angle of arrival
AoD	Angle of departure
AWGN	Additive white Gaussian noise
Co-MINT	Cooperative MINT
CRLB	Cramér-Rao lower bound
DMP	Diffuse multipath
EFIM	Equivalent Fisher information matrix
FI	Fisher information
FIM	Fisher information matrix
LHF	Likelihood function
LOS	Line of sight
MINT	Multipath-assisted indoor navigation and tracking
MPC	Multipath component
NLOS	Non line of sight
PEB	Position error bound
PSD	Power spectral density
RI	Ranging information
RX	Receiver
SINR	Signal-to-interference-plus-noise ratio
SNR	Signal-to-noise ratio
SPEB	Squared position error bound
TX	Transmitter
UWB	Ultra-wideband
VA	Virtual anchor

Frequent Symbols

Symbol	Set ¹	Meaning
Signal Model and Channel		
m	$\{1, \dots, M\}$	Indexes the m -th agent as RX.
j	$\{1, \dots, M\}$	Indexes the j -th agent as TX.
k	$\{1, \dots, K_{m,j}\}$	Indexes the k -th multipath component (MPC).
M	\mathbb{N}	Number of agents.
$K_{m,j}$	\mathbb{N}_0	Number of deterministic MPCs between m -th and j -th agent.
$r_{m,j}(t)$	\mathbb{C}	Signal between m -th and j -th agent, cf. (2.3).
$s(t)$	\mathbb{R}	Transmitted UWB waveform.
$\tau_{m,j}^{(k)}$	$\mathbb{R}_{>0}$	Propagation delay of an MPC (3.1).
$\alpha_{m,j}^{(k)}$	\mathbb{C}	Path amplitude of an MPC.
$\tau_{j,j}^{(k)}$	$\mathbb{R}_{>0}$	Monostatic indexing convention, shown for a delay.
c	$\mathbb{R}_{>0}$	Speed of light $c \approx 3 \cdot 10^8$ m/s.
N_0	$\mathbb{R}_{>0}$	PSD of AWGN $n(t)$ at the RX antenna.
$w_{m,j}^{(k)}$	$(0, 1)$	Weight (2.6) of an MPC due to diffuse multipath (DMP).
Geometry of the Indoor Environment		
\mathbf{p}_m	\mathbb{R}^2	Position of the m -th agent addressed as RX.
\mathbf{p}_j	\mathbb{R}^2	Position of the j -th agent addressed as TX.
$\mathbf{p}_{m,j}^{(k)}$	\mathbb{R}^2	Virtual anchor (VA) position (3.13) for a given MPC.
$\phi_{m,j}^{(k)}$	$(-\pi, +\pi]$	AoA (3.2). Points from VA $\mathbf{p}_{m,j}^{(k)}$ to RX \mathbf{p}_m .
$\gamma_{m,j}^{(k)}$	\mathbb{R}	Effective wall angle (3.26) of a MPC.
$Q_{m,j}^{(k)}$	\mathbb{N}_0	Order of a MPC and its VA, i.e. number of wall reflections. Zero value refers to the LOS component.
q	$\{1, \dots, Q_{m,j}^{(k)}\}$	Indexes the q -th step of a VA construction.
Continued on next page		

(continued from previous page)

Symbol	Set	Meaning
$\gamma_{m,j}^{(k,q)}$	$(-\frac{\pi}{2}, +\frac{\pi}{2}]$	q -th wall angle involved in the construction of a VA.
Single Transmission Estimation Problem		
$\mathbf{r}_{m,j}$	\mathbb{R}^{\dots}	Holds the Karhunen–Loève sampling (2.4) of $r_{m,j}(t)$.
$f(\mathbf{r}_{m,j} \dots)$	\mathbb{R}	Likelihood function (LHF) (2.5) of a single transmission.
$\Phi_{m,j}(\mathbf{x}, \mathbf{y})$	$\mathbb{R}^{(\dim \mathbf{x}) \times (\dim \mathbf{y})}$	Fisher information matrix (FIM) of some parameters \mathbf{x} and \mathbf{y} w.r.t. LHF of a single transmission m, j , cf. (4.5).
$\boldsymbol{\tau}_{m,j}$	$\mathbb{R}_{>0}^{K_{m,j}}$	Holds MPC delays $\tau_{m,j}^{(k)}$ of a transmission m, j , cf. (2.7) (4.1).
$\boldsymbol{\alpha}_{m,j}$	$\mathbb{C}^{K_{m,j}}$	Holds MPC amplitudes $\alpha_{m,j}^{(k)}$ of a transmission, cf. (2.8) (4.2).
$\boldsymbol{\theta}$	$\mathbb{R}^{2+2K_{j,j}}$	Monostatic estimation parameter vector (4.3), $\boldsymbol{\theta} = (\mathbf{p}_j^T, \Re \boldsymbol{\alpha}_{j,j}^T, \Im \boldsymbol{\alpha}_{j,j}^T)^T$.
$\boldsymbol{\psi}$	$\mathbb{R}^{3K_{j,j}}$	Monostatic support parameter vector (4.4), $\boldsymbol{\psi} = (\boldsymbol{\tau}_{j,j}^T, \Re \boldsymbol{\alpha}_{j,j}^T, \Im \boldsymbol{\alpha}_{j,j}^T)^T$.
$\mathbf{J}_{\boldsymbol{\theta}}$	$\mathbb{R}^{\dim \boldsymbol{\theta} \times \dim \boldsymbol{\theta}}$	Fisher information matrix (FIM) (4.7) (4.10) $\mathbf{J}_{\boldsymbol{\theta}} = \Phi_{j,j}(\boldsymbol{\theta}, \boldsymbol{\theta})$.
$\mathbf{J}_{\mathbf{p}_j}$	$\mathbb{R}^{2 \times 2}$	Monostatic equivalent Fisher information matrix (EFIM) (4.11).
Cooperative Estimation Problem		
\mathbf{r}	\mathbb{R}^{\dots}	Holds all sampled received signals $\mathbf{r}_{m,j}$, cf. (5.1).
$f(\mathbf{r} \boldsymbol{\theta})$	\mathbb{R}	Likelihood function (5.7).
$\Phi(\mathbf{x}, \mathbf{y})$	$\mathbb{R}^{(\dim \mathbf{x}) \times (\dim \mathbf{y})}$	FIM of some parameters \mathbf{x} and \mathbf{y} w.r.t. joint LHF, cf. (5.8).
\mathbf{p}	\mathbb{R}^{2M}	Holds all agent positions, cf. (5.2).
K	\mathbb{N}	Number of MPC parameters $K = \sum_{m=1}^M \sum_{j=1}^M K_{m,j}$.
$\boldsymbol{\tau}$	\mathbb{R}_+^K	Holds all delays of all transmissions, cf. (5.3).
$\boldsymbol{\alpha}$	\mathbb{C}^K	Holds all amplitudes of all transmissions, cf. (5.4).
$\boldsymbol{\theta}$	\mathbb{R}^{2M+2K}	Cooperative estimation parameter vector (5.5), $\boldsymbol{\theta} = (\mathbf{p}^T, \Re \boldsymbol{\alpha}^T, \Im \boldsymbol{\alpha}^T)^T$.
$\boldsymbol{\psi}$	\mathbb{R}^{3K}	Cooperative transformed parameter vector (5.6), $\boldsymbol{\psi} = (\boldsymbol{\tau}^T, \Re \boldsymbol{\alpha}^T, \Im \boldsymbol{\alpha}^T)^T$.
$\mathbf{J}_{\boldsymbol{\theta}}$	$\mathbb{R}^{\dim \boldsymbol{\theta} \times \dim \boldsymbol{\theta}}$	Fisher information matrix (FIM) (5.12) $\mathbf{J}_{\boldsymbol{\theta}} = \Phi(\boldsymbol{\theta}, \boldsymbol{\theta})$.
$\mathbf{J}_{\mathbf{p}}$	$\mathbb{R}^{2M \times 2M}$	Cooperative EFIM (5.13) (5.14) (5.26).

Mathematical Notation

All vectors are column vectors unless an explicit transpose is applied. They are denoted in bold lowercase letters, e.g. \mathbf{x} . Matrices are bold uppercase. $\text{tr}\{\mathbf{A}\}$ is the trace [1] of \mathbf{A} . \mathbf{I} and $\mathbf{0}$ are the unity and zero matrix. Matrix dimensions are given by the context or sometimes by explicit subscript denotation. We access element i, j of matrix \mathbf{A} via $[\mathbf{A}]_{i,j}$. We sometimes use matlab notation like $[\mathbf{A}]_{1:i,:}$ for submatrix, row, or column access. When \mathbf{A} has well-arranged block structure, we refer to the i, j -th $M \times N$ submatrix with $[\mathbf{A}]_{M \times N, i, j}$. $\mathbf{e}(\phi) := (\cos(\phi), \sin(\phi))^T$ is a unit vector in direction of angle ϕ . $\mathbf{Rot}(\gamma)$ is a standard 2×2 angle γ rotation matrix. For complex numbers $z \in \mathbb{C}$, we write $\Re z$ and $\Im z$ for real and imaginary parts.

The gradient of a scalar function $f(\mathbf{x})$ w.r.t. to a vector \mathbf{x} is

$$\frac{\partial f(\mathbf{x})}{\partial \mathbf{x}} = \left(\frac{\partial f}{\partial x_1}, \dots, \frac{\partial f}{\partial x_M} \right)^T.$$

When derivatives appear in text, we will usually use a slash, e.g. $\partial f(\mathbf{x})/\partial \mathbf{x}$. With regard to related literature like [2], we assume $\partial f(\mathbf{x})/\partial(\mathbf{x}^T) = (\partial f(\mathbf{x})/\partial \mathbf{x})^T$ for transposed differentials. Regarding second order partial derivatives, we explicitly note a transpose on the second differential $\partial \mathbf{y}^T$ as to clarify the dimensions of the resulting matrix

$$\frac{\partial f(\mathbf{x}, \mathbf{y})}{\partial \mathbf{x} \partial \mathbf{y}^T} = \begin{pmatrix} \frac{\partial f}{\partial x_1 \partial y_1} & \cdots & \frac{\partial f}{\partial x_1 \partial y_N} \\ \vdots & \ddots & \vdots \\ \frac{\partial f}{\partial x_M \partial y_1} & \cdots & \frac{\partial f}{\partial x_M \partial y_N} \end{pmatrix}.$$

The gradient of a vector-valued function $\mathbf{f}(\mathbf{x})$ w.r.t. \mathbf{x} is the Jacobian²

$$\frac{\partial \mathbf{f}(\mathbf{x})}{\partial \mathbf{x}} = \begin{pmatrix} \frac{\partial f_1}{\partial x_1} & \cdots & \frac{\partial f_N}{\partial x_1} \\ \vdots & \ddots & \vdots \\ \frac{\partial f_1}{\partial x_M} & \cdots & \frac{\partial f_N}{\partial x_M} \end{pmatrix}.$$

¹ In the case of a function symbol, the 'Set' column states the image set of that function. Dots used as an exponent indicate high dimensionality where an exact figure would be too involved and also unimportant for this overview.

² Notice that the assumed Jacobian dimensions $\text{dim} \mathbf{x} \times \text{dim} \mathbf{y}$ are consistent with communication theory literature but contradict most math texts, where the transposed dimensions $\text{dim} \mathbf{y} \times \text{dim} \mathbf{x}$ are used (cf. usage in multivariate Taylor series).

Contents

1	Introduction	1
1.1	Literature Survey	1
1.2	Idea of this Work	2
1.3	Goals	3
1.4	Outline	3
2	Problem Framework and Notation	5
2.1	Localization Problem	5
2.2	Channel and Signal Model	6
2.3	The Cramér-Rao Lower Bound	8
2.4	Nuisance Parameters and Path Overlap	9
2.5	Equivalent Fisher Information Matrix	11
3	Geometry of Multipath Components	13
3.1	Virtual Anchors	13
3.2	Spatial Delay Gradient: Preliminary Results	18
3.3	Linear Algebraic Virtual Anchor Construction	20
3.4	Mirror Matrix Properties	24
3.5	Spatial Delay Gradient: Final Result	28
4	Monostatic Localization	31
4.1	Monostatic Cramér-Rao Lower Bound	31
4.1.1	Monostatic CRLB Derivation	31
4.1.2	Monostatic CRLB Result	34
4.2	Analysis of monostatic Virtual Anchors	35
4.2.1	Significant Virtual Anchors	36
4.2.2	Useless Virtual Anchors	39
4.2.3	Miscellaneous Virtual Anchors	42
4.2.4	Inherent Path-Overlap Problem	44
4.3	Monostatic Numerical Results	45
4.3.1	Matlab Approach	45
4.3.2	Results neglecting Path Overlap	46
4.3.3	Results considering Path Overlap	52
5	Cooperative Localization	59
5.1	Cooperative CRLB Derivation	59
5.1.1	FIM, Parameter Transformation and EFIM	60
5.1.2	Simplifications for Dimensionality Reduction	62
5.1.3	Alternative Representation	64
5.2	Cooperative Cramér-Rao Lower Bound	66
5.2.1	Result	66
5.2.2	Discussion	67

Contents

5.3	Cooperative Numerical Results	69
5.3.1	M = 3 Cooperation over a simple Room	69
5.3.2	M = 2 Cooperation over a contorted Room	73
5.3.3	M = 3 Cooperation over an involved Trajectory	75
6	Conclusions	79
6.1	Summary	79
6.2	Outlook	80
A	Appendix	81
A.1	Fisher Information among Signal Model Parameters	81
A.2	Proof: Magnitude times Direction Form of Monostatic Gradient (3.32)	82

1

Introduction

1.1 Literature Survey

Many fields of application demand accurate position knowledge of vehicles, devices or personnel. The most prominent localization solutions are satellite-based systems like Galileo and GPS, where several satellites orbit the earth and serve as reliable anchors for mobile agents to triangulate their positions from the received signals, see for instance [3]. However, these systems fail in rough or tree-covered terrain, dense urban settings and especially in indoor environments because of poor material penetration and dominant multipath propagation [4]. Applications in logistics, disaster relief forces, military blue force tracking and within industrial buildings require location-awareness under such conditions though [3–5].

Wideband and ultra-wideband (UWB) pulses are promising candidates for localization in dense indoor environments as described by [2, 4, 6] amongst others. Large bandwidth yields short pulse durations and in further consequence high spatial resolution and resolvability of multipath components (MPCs) in measurements. In 2002, the US Federal Communications Commission issued regulations, "that allow the unlicensed operation of UWB radios in the microwave range" [7], which is sufficient transmission power for most indoor localization applications. The new regulations led to wide research efforts in the UWB field, for instance [5, 7–9]. Indoor propagation channels were studied in works like [9, 10]. Papers like [5, 6, 11] suggest that Diffuse multipath (DMP) is a dominant portion of indoor propagation channels.

Most available (conventional) systems for indoor positioning require several fixed anchors [2, 4, 12, 13] and are non-robust against NLOS situations. These anchors are immobile transmitters (TXs) or sometimes receivers (RXs) with precisely known position, resulting in high infrastructure expenditure and low flexibility. Multipath-assisted indoor navigation and tracking (MINT) [6, 9, 14] is one possibility to overcome those disadvantages and impairments. MINT assumes a known floor plan of the indoor environment and models MPCs as direct paths from so-called virtual anchors (VAs) [6, 13, 15, 16]. The VAs are mirror images of the TXs with respect to the walls and, because of the known floor plan, have equal position uncertainty as the TX, i.e. precisely known VA positions in the fixed anchor case. Knowledge about VA positions allows their utilization for position estimation, which reduces the amount of required fixed anchors and thereby lowers infrastructure efforts. Accurate performance results of MINT implementations with down to just a single fixed anchor are presented in [17–19].

In [6] the Cramér-Rao lower bound (CRLB) for the MINT set-up has been derived using a channel model which considers deterministic and diffuse multipath. This result is based on work of Shen and Win [4, 12], who showed that MPCs, which are just considered as interference, are usable for localization in the presence of prior knowledge about the channel parameters. Shen and Win use a prior distribution of the channel parameters, while MINT assumes prior knowledge in the comprehensible form of a known floor plan to enable multipath-assisted localization. An alternative way of formalizing room geometry (but with different intentions) is presented in [20]. While [4, 12] assume anchors merely providing one-dimensional ranging information (RI) in line of sight (LOS) direction, agents in a MINT set-up receive individual RI contributions from deterministic MPCs in direction of the respective angle of arrival (AoA).

Cooperative localization is a concept that allows for accurate localization despite low anchor deployment [2, 16, 21, 22]. Several mobile agents transmit pulses to one another and exchange observations for joint position estimation, which boosts localization performance [2]. Cooperative MINT (Co-MINT) [16] is a promising combination of cooperative and multipath-assisted localization. There, cooperating mobile agents perform monostatic and bistatic measurements, i.e. pulse transmission and MPC measurement via receive antenna either happen collocated on the same agent or at physically different agents. The a-priori known floor plan again gives rise to applicable VAs. This renders anchorless localization possible, so no fixed infrastructure is required at all. Fröhle [16] gave a successful proof of concept and developed an estimation algorithm for Co-MINT, but quantitative performance figures like the CRLB [23] on the variance of position estimation are currently unavailable.

Similar CRLB derivations are given for a single agent and multiple fixed anchors with or without prior knowledge in [4, 12], for MIMO radar systems with RI contributions in AoA direction of the individual components in [24], for MINT with one fixed anchor in [6], and for cooperating agents and multiple fixed anchors in [2]. All these derivations work on continuous-time received signals instead of extracted signal metrics to incorporate the entire observed information in the performance bound [4].

1.2 Idea of this Work

In this master thesis, we want to derive a performance bound of Cooperative MINT, which was introduced in [16]. This requires profound understanding of multipath geometry. Particularly, the influence of a mobile TX on the propagation delays of higher-order MPCs is, to the best of our knowledge, an open problem. Therefore, we have to investigate multipath and VA geometry in detail and tackle the aforementioned problem among other things.

Monostatic measurements are a fundamental building block of Co-MINT and, due to TX and RX being collocated, have very specific properties. Hence, we want to study monostatic localization of a single agent, obtain the CRLB thereof, investigate the peculiarities and compute numerical results.

Ultimately, we want to obtain a closed-form CRLB of Co-MINT. The CRLB is not only useful for computing numerical results of the position error bound (PEB), but a closed-form solution also allows studying the influence of technical and environmental parameters on the localization performance.³

³ Furthermore, a closed-form CRLB is a valuable prerequisite for computing covariance matrices during maximum-likelihood estimation [25].

1.3 Goals

- Extend the notation of [6] to a mathematical framework capable of all scheduled cooperative derivations within the chosen signal and geometry model.
- Study multipath geometry, formalize room geometry and VA construction with the goal of finding a general formula for spatial delay gradients of MPCs.
- Define the monostatic position estimation problem. Derive and analyse the monostatic CRLB. Investigate the peculiarities and usefulness of certain classes of monostatic MPCs.
- Define the cooperative position estimation problem. Derive and analyse the cooperative CRLB.

1.4 Outline

- Chapter 2 gives a detailed problem description and introduces, the propagation channel model, the signal model as well as the mathematical and notational framework that will be used throughout the thesis. It introduces estimation of vector parameters from observations, a transformation to an alternative parameter space, nuisance parameters and defines the CRLB.
- Chapter 3 analyses the fundamental quantity of room geometry influence: The spatial gradient of propagation delays over multipath components. A thorough linear algebraic derivation gives an exact result for virtual anchor positions. The spatial gradient thereof will yield a closed-form result for the desired quantity.
- Chapter 4 defines the monostatic position estimation problem and derives the CRLB. The chapter pursues with a theoretical examination of several monostatic multipath geometries and the evaluation of numerical results.
- Chapter 5 defines the cooperative anchorless multipath-assisted position estimation problem and conducts the involved CRLB derivation. On the basis of numerical results, we carry out an investigation of the CRLB result and subsequently the merits of cooperation and the approach by itself.
- Chapter 6 concludes the thesis and discusses possible future research.

2

Problem Framework and Notation

2.1 Localization Problem

We assume a total of M mobile agents at a priori unknown positions in a two-dimensional⁴ indoor environment with a priori known floor plan. The environment is enclosed by walls of a material that reflects radio waves to some extent. Walls are modeled as plane surfaces.

Each agent acts as both omnidirectional transmitter (TX) and receiver (RX) for ultra-wideband (UWB) [7,8] pulses $s(t)$. The agents alternately transmit (one agent at a time) a pulse while all other agents listen. Furthermore, all agents gather the channel impulse response to their own transmitted pulse. Thereby, all monostatic and bistatic measurements are obtained. Figure 2.1 shows an exemplary scenario. We define the meaning of those terms for our purpose:

- **Monostatic:** An agent emits a pulse which then bounces off of walls and returns to the agent over various reflection paths. The agent measures these so-called multipath components (MPCs). TX and RX are collocated on the same device.
- **Bistatic:** One agent emits a pulse while another agent receives the signal. The emitted pulse propagates over a line of sight (LOS) path (if unobstructed) and over several MPCs by bouncing off of walls one or more times before arriving at the RX. TX and RX are different agents.

MPCs are usually nothing but interference, but [4] showed that prior knowledge about the channel parameters enables the utilization of MPCs for localization. In our particular problem, a priori floor plan information allows us to use MPCs for anchorless cooperative localization [16].

The idea was introduced in [16] as follows:

“In the first phase, each mobile performs mono-static measurements. In this mono-static measurement setup, the mobile is both TX and RX. Localization with only this type of measurements alone would not be possible due to ambiguities in the

⁴ Throughout this thesis, we are dealing with two-dimensional geometries exclusively. Related literature [13] claims, “Extension to the three-dimensional localization is straightforward”. In our case though, the extension would require angle pairs instead of single angles for wall and agent alignments in Chapter 3 and would raise the dimensions of mirror matrices from 2×2 to 3×3 in Sections 3.3 and 3.4, which would render those derivations laborious to say the least.

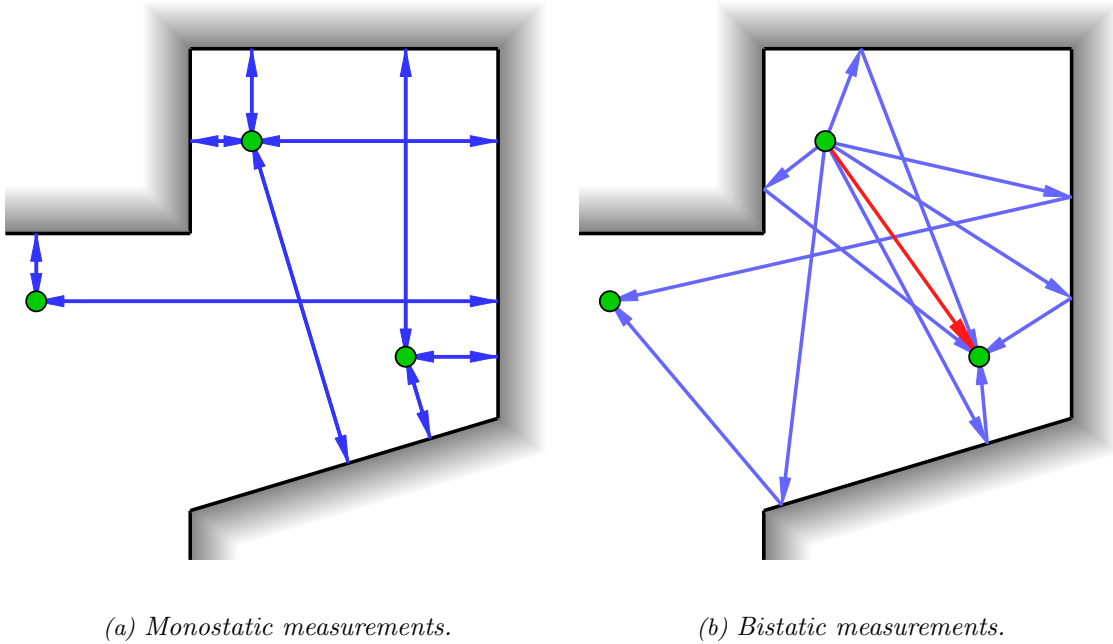


Figure 2.1: The two fundamental modes of transmission are shown. (a) Agents serve as both TX and RX. There is no LOS component, the receive antenna just picks up all signal components that bounced off walls. The shown transmissions do not happen concurrently for obvious reasons. (b) The upper agent is transmitting while the others are listening. The red arrow illustrates a LOS path. Even though the LOS path to the lower left agent is obstructed by a wall corner, the agent still receives two MPCs. In both figures, higher-order reflections were discarded for clarity.

likelihood-function caused by the room geometry. In the second phase, each mobile performs cooperative measurements with its neighbors [...]. In this bi-static measurement setup, the neighbor node acts as TX for the RX node. Cooperative measurements are useful only if the TX position is known. Hypotheses for this are taken from the mono-static measurement. It is therefore possible to determine the position of each cooperating mobile node without the help of a known reference anchor.”

Vectors $\mathbf{p}_m, \mathbf{p}_j \in \mathbb{R}^2$, $1 \leq m, j \leq M$ are unknown agent positions. Both indices m and j can be used to refer to any agent, but we use m when referring to the current RX and j when referring to the current TX. We assume a transmission protocol that avoids collisions and exchanges measurement data. The combined knowledge drawn from the measurements of all agents will be used to perform cooperative estimation of all agent positions.

2.2 Channel and Signal Model

A transmission from TX agent j to RX agent m that receives signal $r_{m,j}(t)$ is defined by

$$r_{m,j}(t) = \int_{-\infty}^{+\infty} s(\lambda) \cdot h_{m,j}(t - \lambda) d\lambda + n(t) \quad (2.1)$$

where $h_{m,j}(t)$ is the impulse response of the propagation channel, $s(t)$ is an UWB pulse, the integral represents a convolution and $n(t)$ is measurement noise at the receive antenna. We assume $n(t)$ to be additive white Gaussian noise (AWGN) [23] with power spectral density

(PSD) $N_0/2$.⁵ Our assumed channel model is

$$h(\tau) = \underbrace{\sum_{k=1}^{K_{m,j}} \alpha_{m,j}^{(k)} \cdot \delta(\tau - \tau_{m,j}^{(k)})}_{\text{Deterministic MPCs}} + \underbrace{\nu_{m,j}(\tau)}_{\text{Diffuse multipath}} . \quad (2.2)$$

The wave propagates over a total of $K_{m,j}$ deterministic MPCs represented by the delta comb in the impulse response. Diffuse multipath (DMP) on the other hand represents all reflections that are not covered by the MPC model. This does not only refer to high-order reflections or reflections w.r.t. objects that are not present in the floor plan, e.g. furniture, wireways, gadgets, people, or animals, but also to scattering and reflections off the agents themselves or any other object in close vicinity to the antennas. Therefore, DMP impairs a received signal $r_{m,j}(t)$ on an interval $t \in (\tau_{m,j}^{(k')}, \infty)$ when there is an unobstructed LOS component k' . DMP is the equivalent to reverberation in acoustics [26]. The suitability of the used model for diffuse indoor channels was confirmed in [6, 9]. The topic is also dealt with in [5, 25] and in much more detail in [11]. $\nu_{m,j}(t)$ is a realization of a non-stationary random process [6, 27]. We use the delay power spectrum [5, 28, 29] $S_{\nu_{m,j}}(\tau)$ to describe the evolution of power density of DMP in the delay domain.

By using (2.2) and performing the convolution in (2.1), we obtain a complex-valued baseband signal model

$$r_{m,j}(t) = \sum_{k=1}^{K_{m,j}} \alpha_{m,j}^{(k)} s(t - \tau_{m,j}^{(k)}) + \int_{-\infty}^{+\infty} s(\lambda) \nu_{m,j}(t - \lambda) d\lambda + n(t) . \quad (2.3)$$

The same channel and signal model are used in [6]. Each MPC has a distinct propagation delay $\tau_{m,j}^{(k)} \in \mathbb{R}_0^+$ (a fundamental quantity in position estimation) and a path amplitude $\alpha_{m,j}^{(k)} \in \mathbb{C}$ representing pathloss and phase shift. For bistatic transmissions, a possible LOS path is simply included in the list of MPCs. The frequent symbols table in the front matter gives an overview of indices.

The same signal model is used for monostatic transmissions. Whenever a single agent serves as both RX and TX ($m = j$) we will refer⁶ to it via index j . Thus we write $r_{j,j}(t)$ for a monostatically received signal. Signal model (2.3) applies to the monostatic case.

In (2.3), $\nu_{m,j}(t)$ convoluted with pulse $s(t)$ represents DMP. An alternative way of looking at DMP is as output of a fictional filter with impulse response $s(t)$ whose input signal is random process $\nu_{m,j}(t)$. The DMP process $\nu_{m,j}(t)$ convoluted with the transmit pulse is thus described as coloured noise process.

For our following estimation problem, we need a discrete set of observations instead of the continuous $r_{m,j}(t)$ to obtain a likelihood function (LHF). Detailed reasons therefor are explained in [6] and like them, we use Karhunen-Loève sampling [27]

$$\mathbf{r}_{m,j} := \text{KL} \{r_{m,j}(t)\} . \quad (2.4)$$

⁵ We use constant PSD $N_0/2$ for AWGN at all RX antennas. Extensions like an individual PSD per RX or even per transmission are unnecessary for our derivations.

⁶ The monostatic indexing convention j, j was chosen that way because MPC quantities are mostly influenced by TX positioning. This will be explained in detail in Chapter 3.

For a received signal within our signal model, Witrisal et al. [6] derived⁷ the LHF

$$f(\mathbf{r}_{m,j}|\boldsymbol{\tau}_{m,j},\boldsymbol{\alpha}_{m,j}) \propto \exp\left\{\frac{2}{N_0}\int_0^{T_0}\Re\left[r_{m,j}(t)\sum_{k=1}^{K_{m,j}}(w_{m,j}^{(k)})^2\cdot(\alpha_{m,j}^{(k)})^*s(t-\tau_{m,j}^{(k)})\right]dt\right. \\ \left.-\frac{1}{N_0}\int_0^{T_0}\sum_{k=1}^{K_{m,j}}w_{m,j}^{(k)}\cdot\alpha_{m,j}^{(k)}s(t-\tau_{m,j}^{(k)})\sum_{k'=1}^Kw_{m,j}^{(k')}\cdot(\alpha_{m,j}^{(k')})^*s(t-\tau_{m,j}^{(k')})dt\right\}. \quad (2.5)$$

Weights $w_{m,j}^{(k)}$ are given [6] as

$$w_{m,j}^{(k)} = \frac{N_0}{N_0 + T_s \cdot S_{\nu_{m,j}}(\tau_{m,j}^{(k)})} \quad (2.6)$$

where we evaluated the delay power spectrum at the delay of the k -th MPC. (2.6) describes the impairment of signal-to-interference-plus-noise ratio (SINR) of a MPC due to DMP.

LHF (2.5) is conditioned on stack vectors of all delays and amplitudes of a single transmission m, j . Later in the text, we will make extensive use of those stacks.

$$\boldsymbol{\tau}_{m,j} := \left(\tau_{m,j}^{(1)}, \dots, \tau_{m,j}^{(K_{m,j})}\right)^T \quad (2.7)$$

$$\boldsymbol{\alpha}_{m,j} := \left(\alpha_{m,j}^{(1)}, \dots, \alpha_{m,j}^{(K_{m,j})}\right)^T \quad (2.8)$$

We will never use (2.5) directly in this thesis but it is fruitful for understanding. Particularly in our Cramér-Rao lower bound (CRLB) end results, we will use certain quantities of Fisher information (FI) among signal model parameters (cf. Appendix A.1) that Witrisal et al. [6] derived from (2.5).

2.3 The Cramér-Rao Lower Bound

Let $\boldsymbol{\theta}$ be a vector parameter and \mathbf{r} noisy observations [23] with distribution⁸ $p(\mathbf{r}|\boldsymbol{\theta})$ where the conditioning implies that \mathbf{r} depends on $\boldsymbol{\theta}$ in some way. We want to find the value of $\boldsymbol{\theta}$ by observing \mathbf{r} . Intuitively, this works best when $\boldsymbol{\theta}$ has a strong influence on the distribution of \mathbf{r} . An estimator $\hat{\boldsymbol{\theta}}$ is a deterministic function that takes \mathbf{r} as input to compute an estimate of $\boldsymbol{\theta}$. Since \mathbf{r} is a random variable, the output value $\hat{\boldsymbol{\theta}}$ is a random variable as well.

A particular estimator that is often sought after is the minimum-variance unbiased estimator (MVUE) [23]:

- **Unbiased:** An unbiased estimator obtains the true value on average, i.e. $E_{\mathbf{r}|\boldsymbol{\theta}}\{\hat{\boldsymbol{\theta}}\} = \boldsymbol{\theta}$.
- **Minimum variance:** No unbiased estimator has variance $\text{var}\{\hat{\boldsymbol{\theta}}\}$ lower than the MVUE.

A popular means of obtaining a lower bound for the variance of an unbiased estimator is the Cramér-Rao lower bound (CRLB). For a vector-valued parameter $\boldsymbol{\theta}$, the CRLB is defined [23]

⁷ The authors used techniques like orthonormal basis functions in conjunction with Karhunen-Loève expansion to derive an inverse kernel for whitening of the DMP, which was required to obtain a standard LHF. The involved derivation is out of scope of this thesis. Although, one should keep in mind that, according to [6], the LHF (2.5) is valid only for signals with certain block spectra and non-overlapping pulses. This is usually violated in practice and thus (2.5) should be used cautiously.

⁸ Despite the bayesian notation, we assume a deterministic (i.e. not random) parameter $\boldsymbol{\theta}$. This is common practice in related literature.

as

$$\text{var}\{\hat{\theta}_i\} \geq [\mathbf{J}_{\boldsymbol{\theta}}^{-1}]_{i,i} \quad (2.9)$$

where $\mathbf{J}_{\boldsymbol{\theta}}$ is the Fisher information matrix (FIM)

$$\mathbf{J}_{\boldsymbol{\theta}} := -\mathbb{E}_{\mathbf{r}|\boldsymbol{\theta}} \left\{ \frac{\partial^2 \ln p(\mathbf{r}|\boldsymbol{\theta})}{\partial \boldsymbol{\theta} \partial \boldsymbol{\theta}^T} \right\}. \quad (2.10)$$

The i -th diagonal element of the FIM inverse is the Cramér-Rao lower bound for the i -th component of $\hat{\boldsymbol{\theta}}$. The CRLB theorem holds if all occurring derivatives exist and a weak condition on the distribution shape is fulfilled, for details see [23].

In our localization problem, the observed data \mathbf{r} consists of sampled received signals that were measured by the agents' receive antennas and are described by LHF (2.5). We will define $\boldsymbol{\theta}$ as the stack vector of agent position(s) and all real and imaginary parts of path amplitudes, e.g. the parameter vector of the monostatic estimation problem is

$$\boldsymbol{\theta} := (\mathbf{p}_j^T, \Re \boldsymbol{\alpha}_{j,j}^T, \Im \boldsymbol{\alpha}_{j,j}^T)^T.$$

We will then obtain the CRLB for position estimation by using (2.9) with those diagonal elements of $\mathbf{J}_{\boldsymbol{\theta}}^{-1}$ that correspond to x and y components of position \mathbf{p}_j , i.e. $[\mathbf{J}_{\boldsymbol{\theta}}^{-1}]_{1,1}$ and $[\mathbf{J}_{\boldsymbol{\theta}}^{-1}]_{2,2}$ for the given parameter vector example.⁹ This yields the position error bound (PEB), a figure of high technical relevance.

While $\boldsymbol{\theta}$ must contain positions \mathbf{p}_j for aforementioned reasons, switching to a higher-dimensional parametrization $\boldsymbol{\psi}$ can facilitate the CRLB derivation: We will define a $\boldsymbol{\psi}$ that contains all delays $\tau_{m,j}^{(k)}$ instead of positions \mathbf{p}_j , e.g. again for the monostatic estimation problem

$$\boldsymbol{\psi} := (\boldsymbol{\tau}_{j,j}^T, \Re \boldsymbol{\alpha}_{j,j}^T, \Im \boldsymbol{\alpha}_{j,j}^T)^T.$$

Then, the FIMs of our parametrizations $\boldsymbol{\theta}$ and $\boldsymbol{\psi}$ are related [6, 23] to one another by

$$\mathbf{J}_{\boldsymbol{\theta}} = \frac{\partial \boldsymbol{\psi}}{\partial \boldsymbol{\theta}} \cdot \mathbf{J}_{\boldsymbol{\psi}} \cdot \frac{\partial \boldsymbol{\psi}^T}{\partial \boldsymbol{\theta}} \quad (2.11)$$

where $\partial \boldsymbol{\psi} / \partial \boldsymbol{\theta}$ is the Jacobian matrix that represents the derivative of $\boldsymbol{\psi}$ w.r.t. $\boldsymbol{\theta}$. Computing $\mathbf{J}_{\boldsymbol{\psi}}$ is easier than direct computation of $\mathbf{J}_{\boldsymbol{\theta}}$ because (2.10) then dictates derivation w.r.t. delays rather than agent positions. The former is more convenient because the signal model (2.3) and subsequently LHF (2.5) explicitly use $\tau_{m,j}^{(k)}$ whereas they depend on \mathbf{p}_m and \mathbf{p}_j only implicitly via $\tau_{m,j}^{(k)}$ (which is a function of agent positions and room geometry).

Transformation (2.11) decomposes $\mathbf{J}_{\boldsymbol{\theta}}$ into the two major influences to the CRLB:

- $\mathbf{J}_{\boldsymbol{\psi}}$: Fisher information (FI) among signal model (2.3) quantities $\tau_{m,j}^{(k)}$ and $\alpha_{m,j}^{(k)}$. Accounts for the resolvability and detectability of these given a measurement $r_{m,j}(t)$.
- $\partial \boldsymbol{\psi} / \partial \boldsymbol{\theta}$: Effect of room geometry. Most importantly contains the sensitivity of delays $\tau_{m,j}^{(k)}$ towards RX and TX agent position, which the entire Chapter 3 is devoted to.

2.4 Nuisance Parameters and Path Overlap

Multipath-assisted cooperative localization and especially monostatic localization suffer from an effect called path overlap. The problem arises when pulses overlap which prevents accurate

⁹ The necessity of including amplitudes in the parameter vector will be explained in Section 2.4.

estimation of the MPC amplitudes $\alpha_{m,j}^{(k)}$, although the amplitude values may seem irrelevant to position estimation at first glance. Figure 2.2 shows how the adverse effect of path overlap can tremendously degrade estimation performance. Since path overlap is a major issue but somewhat unintuitive, we discuss the matter in this introductory section.

Why do we estimate the path amplitudes even though they are not in our interest? Let us emphasize the necessity of nuisance parameter estimation with the help of a classical example: Variance estimation on samples of an unknown normal distribution $x[n] \sim \mathcal{N}(\mu, \sigma^2)$. The MVUE $\hat{\sigma}^2$ involves a normalized sum over terms $(x[n] - \mu)^2$ [23]. Since this estimation endeavour is essentially the exploration of an unknown random variable, we have to assume that we do not have perfect knowledge of its mean value μ just as well. Hence we are forced to estimate $\hat{\mu}$ as a nuisance parameter, even though it is not of direct interest. Inaccurate $\hat{\mu}$ estimation will drastically impair the accuracy of $\hat{\sigma}^2$. The only way around would be perfect prior knowledge about the mean value from the problem context, e.g. $\mu = 0$.

Our situation is completely analogous: Our end result for the CRLB of agent position estimates will be a formula involving the amplitudes $\alpha_{m,j}^{(k)}$, thus knowledge thereof is crucial. In our case with an involved room geometry and channel model, there is certainly no way to obtain perfect knowledge of all MPC phase shifts and attenuations a-priori. Thus, not estimating the path amplitudes as nuisance parameters would be grossly negligent.

Countermeasures to path overlap include a higher transmission bandwidth and thus shorter pulses, changing the localization setup (agent positions and room geometry) as to avoid MPCs with similar delay, or dropping one of the overlapping MPCs from the estimation model. All of these measures are either limited by technical constraints or implementation issues [30], would require unrealistic foresight or suffer from miscellaneous peculiarities that cannot be discussed here.

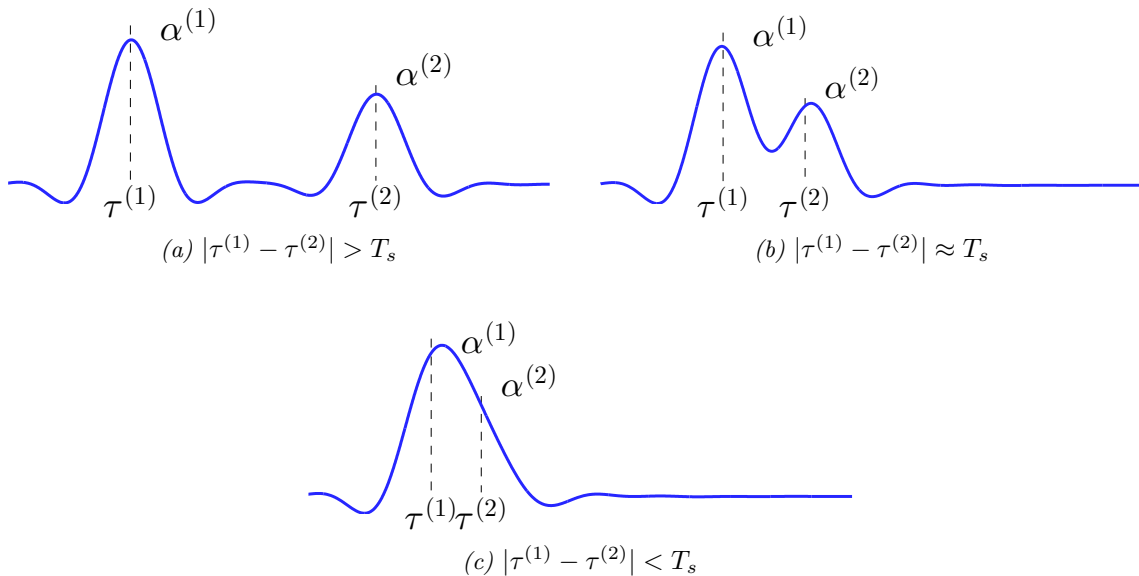


Figure 2.2: The plots show a signal $\alpha^{(1)} \cdot s(t - \tau^{(1)}) + \alpha^{(2)} \cdot s(t - \tau^{(2)})$ which is in accordance with signal model (2.3). $s(t)$ is a raised-cosine pulse with duration T_s . Amplitude estimates $\hat{\alpha}^{(1)}$, $\hat{\alpha}^{(2)}$ are heavily impaired by the effect of path overlap which arises when the difference of pulse delays is lower than the pulse duration. a) Pulses do not overlap, amplitude estimation is unproblematic. b) Pulses overlap slightly, there will be some impairment. c) Pulses overlap vastly and are indistinguishable. Merely some skewness tells that the later pulse has lower power.

Shen and Win [12] explain how ignoring path-overlap led to overly optimistic performance bounds in earlier literature. In [31] they explain the negative effect of path-overlap in great

detail and give a quantitative answer to the extent of impairment on localization performance. Later in this thesis, we will see in the CRLB results how path overlap reduces FI between delays of a received signal and in the course worsens position estimation. Equal MPC delays $\tau_{m,j}^{(k')} = \tau_{m,j}^{(k')}$ will cause a singular amplitude FIM and thus an infinite PEB.

2.5 Equivalent Fisher Information Matrix

When deriving the CRLB, formula (2.9) requires us to compute the inverse $\mathbf{J}_{\boldsymbol{\theta}}^{-1}$ of a high-dimensional FIM, even though most of its blocks are irrelevant (bounds on variances and covariances of nuisance parameters). This amounts to high computational effort and renders all aspirations towards a closed-form solution problematic.

Fortunately, there is a linear algebraic method called Schur complement [4,6,12] that we will use extensively to compute solely the interesting block of the FIM inverse. The following statement is a result of Schur complement customized to our needs:

Let $\mathbf{M} \in \mathbb{R}^{(a+b) \times (a+b)}$ be a symmetric square matrix with an upper left block $\mathbf{A} \in \mathbb{R}^{a \times a}$

$$\mathbf{M} = \begin{pmatrix} \mathbf{A} & \mathbf{B} \\ \mathbf{B}^T & \mathbf{C} \end{pmatrix} .$$

Then the upper left $a \times a$ submatrix of \mathbf{M}^{-1} is equal to the inverse of a matrix $\mathbf{M}_E \in \mathbb{R}^{a \times a}$

$$[\mathbf{M}^{-1}]_{a \times a} = \mathbf{M}_E^{-1} , \quad \mathbf{M}_E := \mathbf{A} - \mathbf{B}^T \mathbf{C}^{-1} \mathbf{B} . \quad (2.12)$$

Applied to our estimation problem, the upper left block of the FIM inverse $\mathbf{J}_{\boldsymbol{\theta}}^{-1}$ is then equal to an inverse $\mathbf{J}_{\mathbf{p}}^{-1}$ where matrix $\mathbf{J}_{\mathbf{p}}$ is known as equivalent Fisher information matrix (EFIM) [4,6,12]. Not only does this ease computation, but, more importantly, also allows for a closed-form EFIM solution for the position estimation and subsequently an analysis of CRLB dependency on technical parameters like room geometry, noise power or the shape of UWB pulse $s(t)$.

3

Geometry of Multipath Components

During Cramér-Rao lower bound (CRLB) derivations of monostatic or cooperative position estimation, we will inevitably stumble upon spatial gradients of propagation delays $\partial\tau_{m,j}^{(k)}/\partial\mathbf{p}_m$, $\partial\tau_{m,j}^{(k)}/\partial\mathbf{p}_j$ and $\partial\tau_{j,j}^{(k)}/\partial\mathbf{p}_j$. For a derivation of CRLBs, a detailed understanding is therefore necessary, however the topic is too involved for an auxiliary treatment in the respective sections. Thus, we dedicate this chapter to the study of multipath geometry to obtain a closed-form solution of the spatial delay gradients.

3.1 Virtual Anchors

In Chapter 2, we defined our scenario with M agents within a room that is limited by flat walls. When a pulse is transmitted, the walls reflect the electromagnetic wave which is considered as a multipath component (MPC), cf. signal model (2.3). A different way of looking at a MPC is to imagine it coming from a virtual anchor (VA) that is located behind the wall. Meissner et al. [15] explain the VA concept,

“Our approach exploits the multipath components (MPCs) of the UWB signal, which result from signal reflections at e.g. the room walls. Using given floor plan information, these MPCs can be mapped to virtual anchors (VAs), which are mirror images of the anchor with respect to the room walls, or other reflecting surfaces.”

Even though they assumed a fixed anchor with known position, this does not invalidate the idea for our purpose: We obtain VA positions $\mathbf{p}_{m,j}^{(k)}$ at the mirror images of the current transmitter (TX) agent position \mathbf{p}_j .¹⁰ Consequently, the k -th MPC is, from a receiver (RX) point of view, equal to a direct path from the k -th VA at $\mathbf{p}_{m,j}^{(k)}$ [13, 15].

The equivalence of MPC and VA model is twofold: Both angle of arrival (AoA) $\phi_{m,j}^{(k)}$ and propagation delay $\tau_{m,j}^{(k)}$ are maintained. The latter implies that the travel distance of the MPC

¹⁰ VAs being the mirror images of \mathbf{p}_j raises the question why we are using RX index m at all for VA position $\mathbf{p}_{m,j}^{(k)}$. The only reason is that transmissions $r_{m,j}(t)$ involving the same TX j but to different RXs m each require their own specific MPC indexing domain $1 \leq k \leq K_{m,j}$. This is due to certain intricacies, for instance monostatic cases cannot hold line of sight (LOS) paths in their MPC lists or in bistatic cases a certain MPC might be meaningless or obstructed for some RX. See Figure 3.2 and 3.3, where the addition of a LOS component changes k -indexing. Formally, k cannot occur in the absence of m because its upper limit $K_{m,j}$ is dependent on m . On these grounds, the excessive and somewhat unintuitive notation with m, j subscript is necessary.

and the RX-VA distance $\|\mathbf{p}_m - \mathbf{p}_{m,j}^{(k)}\|$ are equal. These properties hold for any VA order, which is the number of reflections of the associated MPC. We denote the VA order or likewise the MPC order with $Q_{m,j}^{(k)}$. The VA concept is known as virtual source in acoustics. Shen and Win [13] use the term virtual node.¹¹

Figure 3.1 shows the set of first-order VAs for an exemplary indoor environment with a TX agent at position \mathbf{p}_j . The VA positions are simply the mirror images of the TX w.r.t. the walls.

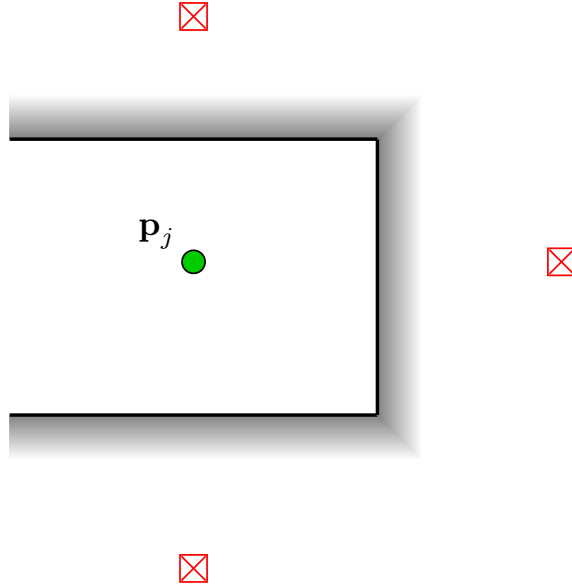


Figure 3.1: Three first-order VAs of a transmitting agent in an exemplary indoor scenario.

Figure 3.2 illustrates the VA-modeled part of a monostatic transmission of the same agent. Agent j functions as both RX and TX. First-order MPCs ($Q_{j,j}^{(k)} = 1$) and their rays are depicted. Three walls amount to $K_{m,j} = 3$ VAs, i.e. $1 \leq k \leq 3$. The rays bounce off perpendicularly and return to the agent on the same path they came from.

Figure 3.3 shows a bistatic transmission where the TX remains in the same position \mathbf{p}_j as in the previous scenarios, but an RX node at a separate position \mathbf{p}_m has entered the scene. All VA positions stay the same, they do not depend on RX position. There is a LOS path from \mathbf{p}_j to \mathbf{p}_m , which we consider as an additional MPC of 0-th order with index $k = 1$ ($Q_{m,j}^{(1)} = 0$). Thus, \mathbf{p}_j coincides with VA $\mathbf{p}_{m,j}^{(1)}$, the number of VAs $K_{m,j} = 4$ increased compared to the monostatic scenario, and the k -indexing of the remaining VAs changed. The figure elegantly shows the aforementioned properties of the VA model regarding preservation of travel distance and AoA. The first segment of each reflected ray, that is the path from the TX to the wall, is obtained by finding the intersection point between wall and VA-RX path.

We also want to give a construction example of a VA that represents a higher-order MPC, i.e. multiple wall reflections. We consider a threefold reflection that involves the three walls of the exemplary room in clockwise order (upper \rightarrow right \rightarrow lower wall). Figure 3.4 shows the construction process: a) Mirroring the TX on the first wall yields a first intermediate position $\mathbf{p}_i^{(1)}$ (which is also the VA of a first-order MPC that we do not consider for the moment). b) Mirroring $\mathbf{p}_i^{(1)}$ as well, but now on the second wall, yields a second intermediate position $\mathbf{p}_i^{(2)}$. c) Mirroring $\mathbf{p}_i^{(2)}$ on the last wall finally attains the virtual anchor $\mathbf{p}_i^{(3)} = \mathbf{p}_{m,j}^{(k)}$.

¹¹ The term “virtual node” might be more suitable than “virtual anchor” within this thesis because of the absence of actual fixed anchors. Nevertheless, we stick to “virtual anchor” to maintain consistency with other MINT and Co-MINT literature.

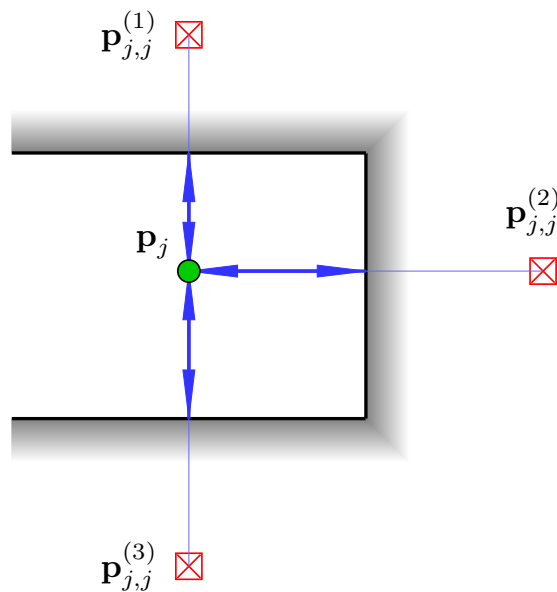


Figure 3.2: Monostatic transmission where three first-order MPCs are modeled by their respective VAs.

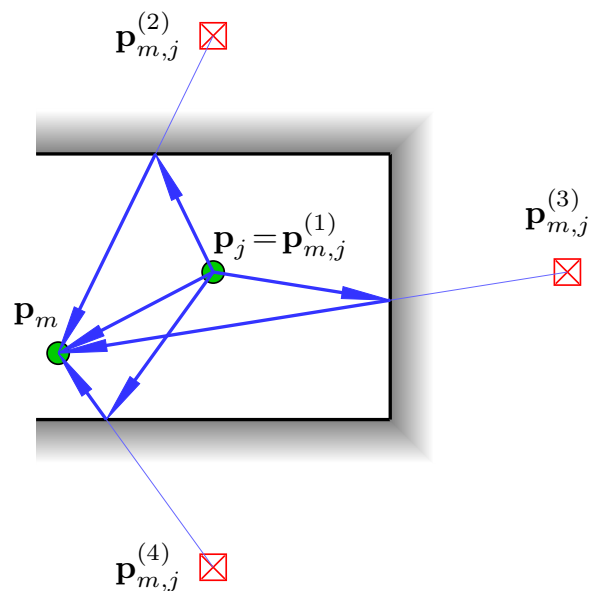


Figure 3.3: Bistatic transmission where three first-order MPCs and a LOS path are modeled using four VAs.

Figure 3.5 shows how the propagation path of a bistatic MPC ray modeled by the above third-order VA is obtained: The VA-RX path (i.e. the long line including the last ray segment) intersects with the last involved, lower wall. The intersection point serves as destination for the previous ray segment, whose virtual source is intermediate position $\mathbf{p}_i^{(2)}$. This path then intersects with the right wall and so on. The backtracking in the depicted fashion ultimately reaches the TX, which concludes the procedure.

Figure 3.6 shows the outcome of the same procedure for a monostatic MPC of the same third-order VA. Again, whether or not RX and TX are collocated does not affect the VA position.

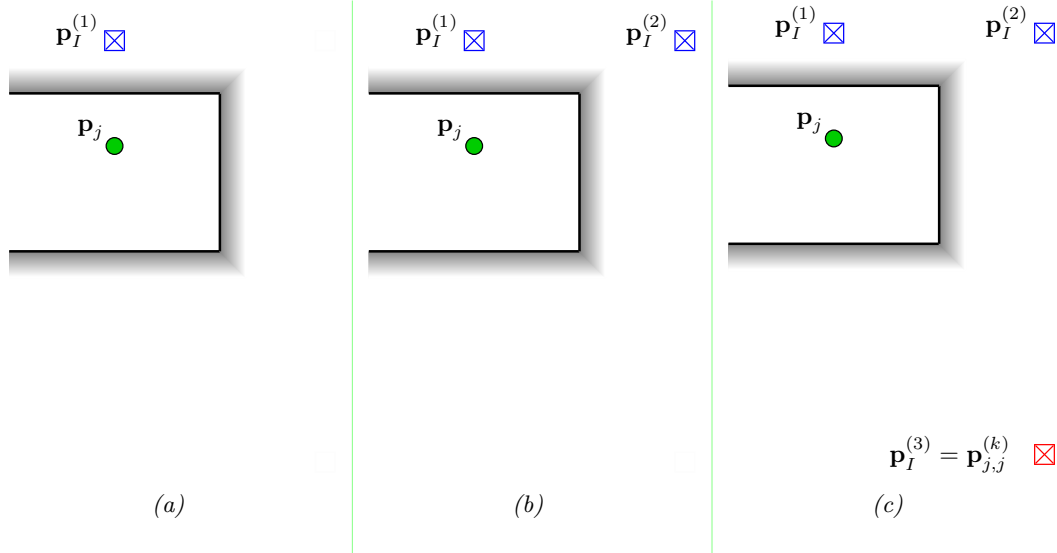


Figure 3.4: Construction of a third-order VA.

Beware that the VA construction procedure may yield unrealistic reflection paths. This includes the following aspects:

- **Feasibility:** Does the VA account for a feasible reflection path?
- **Obstacles:** Is the ray unobstructed? Are the only points of contact the designated wall reflections in the intended order?
- **Orientation:** Does the ray hit all designated walls on their surface areas rather than the material side?

The executing program must pay attention to the reasonableness of the construction. The mathematical model introduced later in this chapter does not account for these peculiarities either, but our Matlab scripts for numerical results, cf. Section 4.3 and 5.3, do so. Examples for infeasible VA constructions are second-order VAs between parallel walls of equal orientation or between two walls of an obtuse-angled corner (i.e. $> 90^\circ$). In such scenarios, the VA may sit inside the room instead of behind a wall and/or results in a reflection path that immediately contradicts elementary optics and common sense. Often these cases lead to the ray visiting walls in an unintended order or from the material side, so they can be intercepted by the unobstructed-criterion or orientation-criterion, but for computational reasons it is wise to discard void VAs beforehand instead of checking said criteria for each agent arrangement.

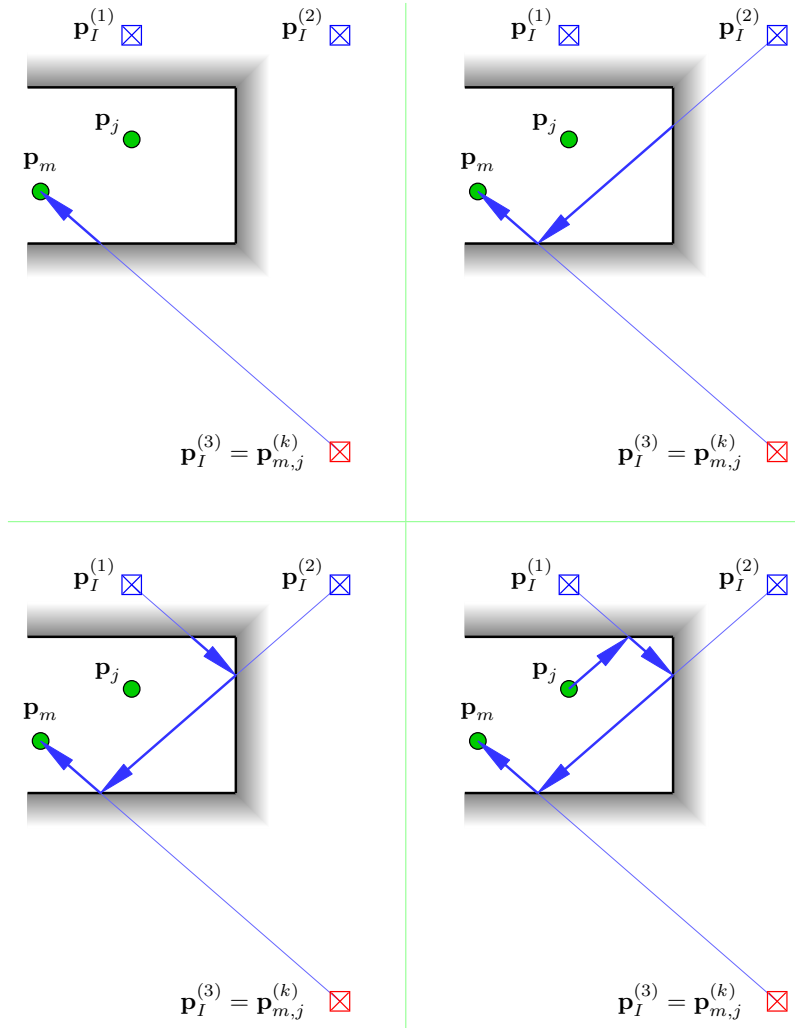


Figure 3.5: Bistatic ray tracing of a given third-order VA and its intermediate construction positions.

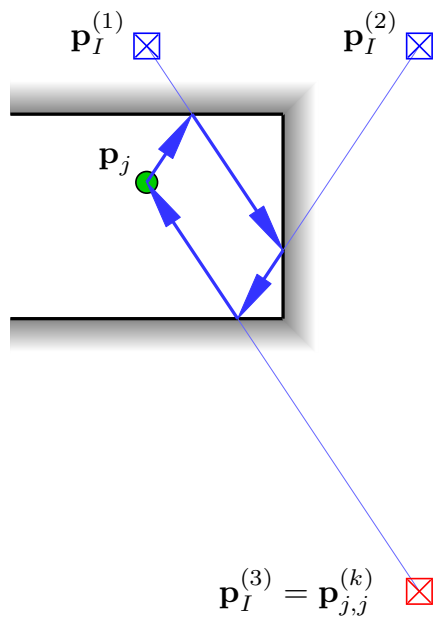


Figure 3.6: Monostatic ray tracing of a third-order VA. Intermediate steps are analogous to Figure 3.5 and not shown.

3.2 Spatial Delay Gradient: Preliminary Results

Earlier in the chapter, we outlined the importance of the spatial gradient of the propagation delay $\tau_{m,j}^{(k)}$ of an MPC. And rightfully so: The path delay is the central quantity of position estimation and therefore its sensitivity towards positioning is crucial. For example, think about the role of delays in the popular time of arrival (ToA) or time difference of arrival (TDoA) [3] localization implementations. Low sensitivity means one can draw little position information from delays and will subsequently experience poor localization performance and vice versa.

Monostatic measurements raise interest in the gradient $\partial\tau_{j,j}^{(k)}/\partial\mathbf{p}_j$. Concerning bistatic measurements, both the delay gradients w.r.t. RX position $\partial\tau_{m,j}^{(k)}/\partial\mathbf{p}_m$ and TX position $\partial\tau_{m,j}^{(k)}/\partial\mathbf{p}_j$ are relevant. We will perform derivations in a universal fashion and look at $\partial\tau_{m,j}^{(k)}/\partial\mathbf{p}_\eta$ where η is arbitrary and either $m \neq j$ or $m = j$ may be the case.

Section 3.1 explained that distance and angle between VA and RX are equal to travelling distance and AoA of the MPC ray. This constitutes the fundamental properties of our geometric figures: The propagation delay $\tau_{m,j}^{(k)}$ fulfills [4, 6, 12, 24]

$$c \cdot \tau_{m,j}^{(k)} = \|\mathbf{p}_m - \mathbf{p}_{m,j}^{(k)}\| = \sqrt{(x_m - x_{m,j}^{(k)})^2 + (y_m - y_{m,j}^{(k)})^2} \quad (3.1)$$

where $c \approx 3 \cdot 10^8$ m/s is the speed of light. On the other hand, AoA $\phi_{m,j}^{(k)}$ is the angle between $\mathbf{p}_{m,j}^{(k)}$ and \mathbf{p}_m (cf. [4, 6, 12]) and thus per definition [32] of trigonometric functions

$$\sin(\phi_{m,j}^{(k)}) = \frac{y_m - y_{m,j}^{(k)}}{\|\mathbf{p}_m - \mathbf{p}_{m,j}^{(k)}\|}, \quad \cos(\phi_{m,j}^{(k)}) = \frac{x_m - x_{m,j}^{(k)}}{\|\mathbf{p}_m - \mathbf{p}_{m,j}^{(k)}\|}. \quad (3.2)$$

Ultimately, we want to obtain the spatial gradient of $\tau_{m,j}^{(k)}$. But instead of differentiating $\tau_{m,j}^{(k)}$ from (3.1) directly w.r.t. \mathbf{p}_η , i.e. x_η and y_η componentwise, let us use a two-dimensional function $\mathbf{f} : \mathbb{R}^2 \rightarrow \mathbb{R}^2$, $(x, y) \mapsto \mathbf{f}(x, y)$ to keep the notation unscattered and simple:

$$\begin{aligned} \frac{\partial}{\partial x} \|\mathbf{f}(x, y)\| &= \frac{\partial}{\partial x} \left\| \begin{pmatrix} f_x(x, y) \\ f_y(x, y) \end{pmatrix} \right\| = \frac{\partial}{\partial x} \sqrt{f_x(x, y)^2 + f_y(x, y)^2} \\ &= \frac{2 \cdot f_x(x, y) \cdot \frac{\partial}{\partial x} f_x(x, y) + 2 \cdot f_y(x, y) \cdot \frac{\partial}{\partial x} f_y(x, y)}{2 \cdot \sqrt{f_x(x, y)^2 + f_y(x, y)^2}} \\ &= \frac{f_x(x, y)}{\|\mathbf{f}(x, y)\|} \cdot \frac{\partial f_x(x, y)}{\partial x} + \frac{f_y(x, y)}{\|\mathbf{f}(x, y)\|} \cdot \frac{\partial f_y(x, y)}{\partial x} \end{aligned}$$

We apply the above formalism on $\|\mathbf{p}_m - \mathbf{p}_{m,j}^{(k)}\|$ from (3.1)

$$\begin{aligned} c \cdot \frac{\partial \tau_{m,j}^{(k)}}{\partial x_\eta} &= \frac{x_m - x_{m,j}^{(k)}}{\|\mathbf{p}_m - \mathbf{p}_{m,j}^{(k)}\|} \cdot \frac{\partial(x_m - x_{m,j}^{(k)})}{\partial x_\eta} + \frac{y_m - y_{m,j}^{(k)}}{\|\mathbf{p}_m - \mathbf{p}_{m,j}^{(k)}\|} \cdot \frac{\partial(y_m - y_{m,j}^{(k)})}{\partial x_\eta} \\ c \cdot \frac{\partial \tau_{m,j}^{(k)}}{\partial y_\eta} &= \frac{x_m - x_{m,j}^{(k)}}{\|\mathbf{p}_m - \mathbf{p}_{m,j}^{(k)}\|} \cdot \frac{\partial(x_m - x_{m,j}^{(k)})}{\partial y_\eta} + \frac{y_m - y_{m,j}^{(k)}}{\|\mathbf{p}_m - \mathbf{p}_{m,j}^{(k)}\|} \cdot \frac{\partial(y_m - y_{m,j}^{(k)})}{\partial y_\eta} \end{aligned}$$

and identify the leading brackets as trigonometric functions (3.2)

$$\begin{aligned} c \cdot \frac{\partial \tau_{m,j}^{(k)}}{\partial x_\eta} &= \cos(\phi_{m,j}^{(k)}) \cdot \frac{\partial(x_m - x_{m,j}^{(k)})}{\partial x_\eta} + \sin(\phi_{m,j}^{(k)}) \cdot \frac{\partial(y_m - y_{m,j}^{(k)})}{\partial x_\eta} \\ c \cdot \frac{\partial \tau_{m,j}^{(k)}}{\partial y_\eta} &= \cos(\phi_{m,j}^{(k)}) \cdot \frac{\partial(x_m - x_{m,j}^{(k)})}{\partial y_\eta} + \sin(\phi_{m,j}^{(k)}) \cdot \frac{\partial(y_m - y_{m,j}^{(k)})}{\partial y_\eta} . \end{aligned}$$

The derivatives from the chain rule demand further analysis though. By using linear algebraic notation and splitting up the subtractions, we decompose the gradient into the Jacobians of the position parameters and a unit vector in direction $\phi_{m,j}^{(k)}$.

$$\begin{aligned} c \cdot \frac{\partial \tau_{m,j}^{(k)}}{\partial \mathbf{p}_\eta} &= \begin{pmatrix} \frac{\partial(x_m - x_{m,j}^{(k)})}{\partial x_\eta} & \frac{\partial(y_m - y_{m,j}^{(k)})}{\partial x_\eta} \\ \frac{\partial(x_m - x_{m,j}^{(k)})}{\partial y_\eta} & \frac{\partial(y_m - y_{m,j}^{(k)})}{\partial y_\eta} \end{pmatrix} \begin{pmatrix} \cos(\phi_{m,j}^{(k)}) \\ \sin(\phi_{m,j}^{(k)}) \end{pmatrix} \\ &= \left(\begin{pmatrix} \frac{\partial x_m}{\partial x_\eta} & \frac{\partial y_m}{\partial x_\eta} \\ \frac{\partial x_m}{\partial y_\eta} & \frac{\partial y_m}{\partial y_\eta} \end{pmatrix} - \begin{pmatrix} \frac{\partial x_{m,j}^{(k)}}{\partial x_\eta} & \frac{\partial y_{m,j}^{(k)}}{\partial x_\eta} \\ \frac{\partial x_{m,j}^{(k)}}{\partial y_\eta} & \frac{\partial y_{m,j}^{(k)}}{\partial y_\eta} \end{pmatrix} \right) \begin{pmatrix} \cos(\phi_{m,j}^{(k)}) \\ \sin(\phi_{m,j}^{(k)}) \end{pmatrix} = \left(\frac{\partial \mathbf{p}_m}{\partial \mathbf{p}_\eta} - \frac{\partial \mathbf{p}_{m,j}^{(k)}}{\partial \mathbf{p}_\eta} \right) \mathbf{e}(\phi_{m,j}^{(k)}) \end{aligned}$$

We take note that Jacobian $\partial \mathbf{p}_m / \partial \mathbf{p}_\eta$ becomes either $\mathbf{0}$ when $m \neq \eta$ or unity \mathbf{I} when $m = \eta$. We use a Kronecker delta $\delta_{m,\eta}$ to combine both cases nicely where

$$\delta_{m,j} := \begin{cases} 1 & \text{if } m = j \\ 0 & \text{if } m \neq j \end{cases} . \quad (3.3)$$

According to Section 3.1, a VA position $\mathbf{p}_{m,j}^{(k)}$ is determined by TX position \mathbf{p}_j and room geometry and hence is not dependent on RX position \mathbf{p}_m . Thus, $\partial \mathbf{p}_{m,j}^{(k)} / \partial \mathbf{p}_\eta$ vanishes for all cases but $\eta = j$, so we write

$$\frac{\partial \mathbf{p}_{m,j}^{(k)}}{\partial \mathbf{p}_\eta} = \delta_{\eta,j} \cdot \frac{\partial \mathbf{p}_{m,j}^{(k)}}{\partial \mathbf{p}_j}$$

in the upcoming result (3.4) to increase intuition and for consistency with the gradient end result in Section 3.5.

Preliminary Result for the Spatial Gradient of the Propagation Delay

$$\frac{\partial \tau_{m,j}^{(k)}}{\partial \mathbf{p}_\eta} = \frac{1}{c} \left(\delta_{m,\eta} \cdot \mathbf{I} - \delta_{\eta,j} \cdot \frac{\partial \mathbf{p}_{m,j}^{(k)}}{\partial \mathbf{p}_j} \right) \mathbf{e}(\phi_{m,j}^{(k)}) \quad (3.4)$$

Formula (3.4) is nicely decomposed into the influence of RX position minus the influence of VA position as a result of TX position. An informal explanation for the subtraction is: When both RX and VA move in the same direction, the delay will remain constant. When they move in opposed directions, there will be maximum change to the delay.

In gradients of bistatic cases, either $\delta_{m,\eta}$ or $\delta_{\eta,j}$ will be active, i.e. either RX or TX positioning influence will be present. In monostatic cases, both influences will be present simultaneously.

Differentiating the delay of a bistatic transmission w.r.t. to the RX position is easy and the result is well-known in all of radar and fixed-anchor localization literature, e.g. [4, 6, 12, 24]

$$\frac{\partial \tau_{m,j}^{(k)}}{\partial \mathbf{p}_m} = \frac{1}{c} (1 \cdot \mathbf{I} - 0 \cdot \mathbf{0}) \mathbf{e}(\phi_{m,j}^{(k)}) = \frac{1}{c} \mathbf{e}(\phi_{m,j}^{(k)}) . \quad (3.5)$$

The Jacobian $\partial \mathbf{p}_{m,j}^{(k)} / \partial \mathbf{p}_j$, the derivative of a VA position w.r.t. to TX agent position, is the most important term of (3.4) for describing the movement of a TX agent, i.e. of the corresponding VAs. Its solution requires rigorous mathematical formalization of room geometry and the VA construction procedure in Section 3.1, which will be the agenda for the remainder of this chapter.

3.3 Linear Algebraic Virtual Anchor Construction

In this section, we will formalize the geometric construction procedure of VAs that was introduced in Section 3.1. Our goal is to find an exact expression for VA position $\mathbf{p}_{m,j}^{(k)}$ and subsequently the Jacobian $\partial \mathbf{p}_{m,j}^{(k)} / \partial \mathbf{p}_j$. Since we can perform all of the following derivations on a fixed MPC of a fixed TX without loss of generality, we will temporarily drop all m, j, k indices for the sake of notation. Table 3.1 defines the notation change.

Temporary Notation	\mathbf{p}_{TX}	\mathbf{p}_{VA}	Q	$\gamma^{(q)}$
Complete Notation	\mathbf{p}_j	$\mathbf{p}_{m,j}^{(k)}$	$Q_{m,j}^{(k)}$	$\gamma_{m,j}^{(k,q)}$

Table 3.1: Translation table between the complete notation and the temporary notation that will be used by the derivation in Section 3.3 and 3.4. Some symbols do not have an equivalent in the complete notation because their usage is limited to the derivations in Section 3.3 and 3.4.

The main quantity of interest is $\partial \mathbf{p}_{\text{VA}} / \partial \mathbf{p}_{\text{TX}}$. We are observing an MPC of arbitrary order Q , i.e. the wave bounces off of walls Q times before it is received. For the VA construction this means we have to do Q consecutive mirroring operations on the involved walls starting with position \mathbf{p}_{TX} . We will use index q , $1 \leq q \leq Q$ for iterating this procedure. Mirroring \mathbf{p}_{TX} on the first wall yields the first intermediate position denoted by $\mathbf{p}_1^{(1)}$. We introduce an iterative rule: Mirroring $\mathbf{p}_1^{(q-1)}$ on the q -th wall yields $\mathbf{p}_1^{(q)}$. The definitions

$$\begin{aligned} \mathbf{p}_1^{(0)} &:= \mathbf{p}_{\text{TX}} \\ \mathbf{p}_1^{(Q)} &:= \mathbf{p}_{\text{VA}} \end{aligned}$$

ensure that we can describe the VA construction procedure from Section 3.1 by simply iterating from $\mathbf{p}_1^{(0)}$ to $\mathbf{p}_1^{(Q)}$. Next we have to formalize room geometry and VA construction.

Walls are considered as line equation model. The model is complete with knowledge of the wall angle¹² $\gamma^{(q)} \in (-\frac{\pi}{2}, +\frac{\pi}{2}]$ and an offset vector¹³ $\mathbf{d}^{(q)} = (d_x^{(q)}, d_y^{(q)})^T$ that sits on the wall:

$$y - d_y^{(q)} = \tan(\gamma^{(q)}) \cdot (x - d_x^{(q)}) \quad (3.6)$$

¹² The wall angle domain could be extended to $\gamma^{(q)} \in (-\pi, +\pi]$ to account for wall orientation, i.e. to answer the question where the surface and material sides are. This was omitted in favour of the simplest model.

Wall Mirroring Formula (simplest form) for the q -th Iteration of VA Construction

$$\mathbf{p}_I^{(q)} = \begin{pmatrix} \cos(2\gamma^{(q)}) & \sin(2\gamma^{(q)}) \\ \sin(2\gamma^{(q)}) & -\cos(2\gamma^{(q)}) \end{pmatrix} \cdot (\mathbf{p}_I^{(q-1)} - \mathbf{d}^{(q)}) + \mathbf{d}^{(q)} \quad (3.7)$$

Proof of (3.7): Figure 3.7 guides the proof by showing a wall-mirroring scenario with all important quantities. For mathematical description we use short symbols \mathbf{e} , \mathbf{d} instead of $\mathbf{e}(\gamma^{(q)})$, $\mathbf{d}^{(q)}$ though. Position \mathbf{p}_\perp is the orthogonal projection of the initial position $\mathbf{p}_I^{(q-1)}$ on the wall, and our sketch shows that

$$\begin{aligned} \mathbf{p}_\perp - \mathbf{d} &= \mathbf{e} \cdot \langle \mathbf{e}, \mathbf{p}_I^{(q-1)} - \mathbf{d} \rangle = \mathbf{e}\mathbf{e}^T(\mathbf{p}_I^{(q-1)} - \mathbf{d}) \\ \mathbf{p}_\perp &= \mathbf{e}\mathbf{e}^T(\mathbf{p}_I^{(q-1)} - \mathbf{d}) + \mathbf{d} . \end{aligned} \quad (3.8)$$

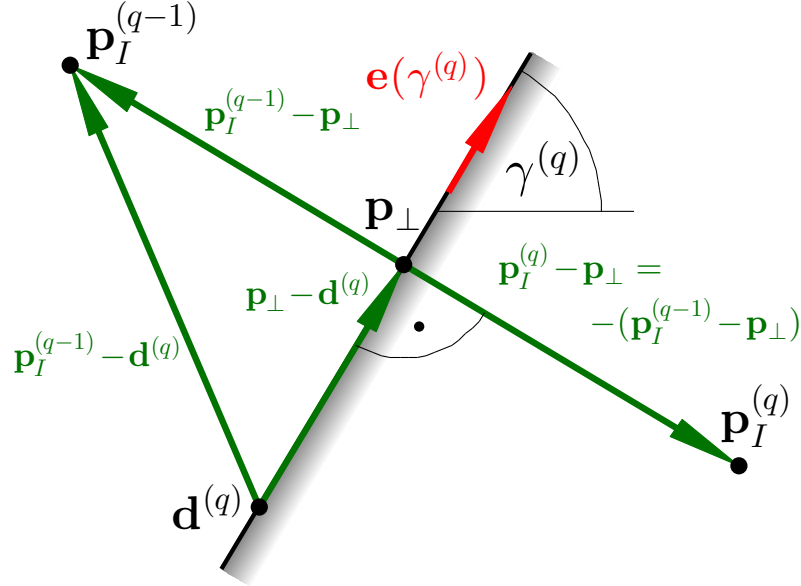


Figure 3.7: This wall-mirroring sketch of the q -th iteration of a VA construction supports the proof of (3.7). $\mathbf{p}_I^{(q-1)}$ is the given position and $\mathbf{p}_I^{(q)}$ the result, i.e. the mirrored point. Wall angle $\gamma^{(q)}$ and wall offset $\mathbf{d}^{(q)}$ are required within our wall model (3.6).

Figure 3.7 shows that the mirrored point $\mathbf{p}_I^{(q)}$ is constructed by flipping the vector that points from \mathbf{p}_\perp to $\mathbf{p}_I^{(q-1)}$

$$\mathbf{p}_I^{(q)} = \mathbf{p}_\perp + (\mathbf{p}_I^{(q)} - \mathbf{p}_\perp) = \mathbf{p}_\perp - (\mathbf{p}_I^{(q-1)} - \mathbf{p}_\perp) = 2\mathbf{p}_\perp - \mathbf{p}_I^{(q-1)}$$

and by further substituting \mathbf{p}_\perp by expression (3.8), we can work towards the end result structure

$$\begin{aligned} \mathbf{p}_I^{(q)} &= 2\mathbf{e}\mathbf{e}^T(\mathbf{p}_I^{(q-1)} - \mathbf{d}) + 2\mathbf{d} - \mathbf{p}_I^{(q-1)} = 2\mathbf{e}\mathbf{e}^T(\mathbf{p}_I^{(q-1)} - \mathbf{d}) - \mathbf{I}(\mathbf{p}_I^{(q-1)} - \mathbf{d}) + \mathbf{d} \\ &= (2\mathbf{e}\mathbf{e}^T - \mathbf{I})(\mathbf{p}_I^{(q-1)} - \mathbf{d}) + \mathbf{d} . \end{aligned}$$

¹³ Note that a two-dimensional offset $\mathbf{d}^{(q)}$ is required to properly handle both borderline cases: A vertical wall has $\gamma^{(q)} = \frac{\pi}{2}$, the line equation becomes $y - d_y^{(q)} = \infty \cdot (x - d_x^{(q)}) \iff \frac{y - d_y^{(q)}}{\infty} = x - d_x^{(q)} \iff x = d_x^{(q)}$. On the other hand, a horizontal wall has $\gamma^{(q)} = 0$, which causes $y - d_y^{(q)} = 0 \cdot (x - d_x^{(q)}) \iff y = d_y^{(q)}$. The extra dimension makes the choice of $\mathbf{d}^{(q)}$ ambiguous: Any point on the wall is just as good as the other.

Matrix $2\mathbf{e}\mathbf{e}^T - \mathbf{I}$ is simplified by recognizing double-angle formulae [32] in the matrix elements

$$2\mathbf{e}\mathbf{e}^T - \mathbf{I} = \begin{pmatrix} 2\cos^2(\gamma^{(q)}) - 1 & 2\cos(\gamma^{(q)})\sin(\gamma^{(q)}) \\ 2\sin(\gamma^{(q)})\cos(\gamma^{(q)}) & 2\sin^2(\gamma^{(q)}) - 1 \end{pmatrix} = \begin{pmatrix} \cos(2\gamma^{(q)}) & \sin(2\gamma^{(q)}) \\ \sin(2\gamma^{(q)}) & -\cos(2\gamma^{(q)}) \end{pmatrix}$$

which concludes the proof. \square

Alternative View on Mirroring

A more comprehensible view on (3.7) is given by an easy matrix decomposition

$$\mathbf{p}_I^{(q)} = \underbrace{\begin{pmatrix} \cos(2\gamma^{(q)}) & -\sin(2\gamma^{(q)}) \\ \sin(2\gamma^{(q)}) & \cos(2\gamma^{(q)}) \end{pmatrix}}_{III.} \cdot \underbrace{\begin{pmatrix} 1 & 0 \\ 0 & -1 \end{pmatrix}}_{II.} \cdot \underbrace{(\mathbf{p}_I^{(q-1)} - \mathbf{d}^{(q)})}_{I.} + \underbrace{\mathbf{d}^{(q)}}_{IV.} \quad (3.9)$$

The steps labeled below (3.9) are shown in Figure 3.8 and process input vector $\mathbf{p}_I^{(q-1)}$ in the following way:

- I.: Remove wall offset, i.e. move the arrangement so that the wall goes through the coordinate system origin.
- II.: Invert y-coordinate, i.e. mirror the shifted point $\mathbf{p}_I^{(q-1)}$ about the x-axis.
- III.: Angle $2\gamma^{(q)}$ rotation about the origin. The linear map is a rotation matrix (3.17).
- IV.: Add again the offset that was removed in step I.

The mirroring result is invariant against the choice of $\mathbf{d}^{(q)}$ as long as it sits on the wall. This might appear counterintuitive in the light of this procedure but will be shown later in (3.22).

Constructing VAs of arbitrary Order

To obtain the Jacobian $\partial\mathbf{p}_{VA}/\partial\mathbf{p}_{TX}$, the most suitable form of (3.7) has the $\mathbf{p}_I^{(q-1)}$ -summand isolated from all other influences.

$$\mathbf{p}_I^{(q)} = \mathbf{M}(\gamma^{(q)})\mathbf{p}_I^{(q-1)} + (\mathbf{I} - \mathbf{M}(\gamma^{(q)}))\mathbf{d}^{(q)} \quad (3.10)$$

The above expression uses a matrix function $\mathbf{M} : \mathbb{R} \mapsto [-1, 1]^{2 \times 2}$ that we will henceforth call mirror matrix.

Mirror Matrix

$$\mathbf{M}(\gamma^{(q)}) := \begin{pmatrix} \cos(2\gamma^{(q)}) & \sin(2\gamma^{(q)}) \\ \sin(2\gamma^{(q)}) & -\cos(2\gamma^{(q)}) \end{pmatrix} \quad (3.11)$$

We use (3.10) and (3.11) to encapsulate our iteration between intermediate positions $\mathbf{p}_I^{(q-1)}$ and $\mathbf{p}_I^{(q)}$ in a mirroring function

$$\mathbf{p}_I^{(q)} = \mathbf{Mir}(\mathbf{p}_I^{(q-1)}, \gamma^{(q)}, \mathbf{d}^{(q)}) := \mathbf{M}(\gamma^{(q)})\mathbf{p}_I^{(q-1)} + (\mathbf{I} - \mathbf{M}(\gamma^{(q)}))\mathbf{d}^{(q)} \quad (3.12)$$

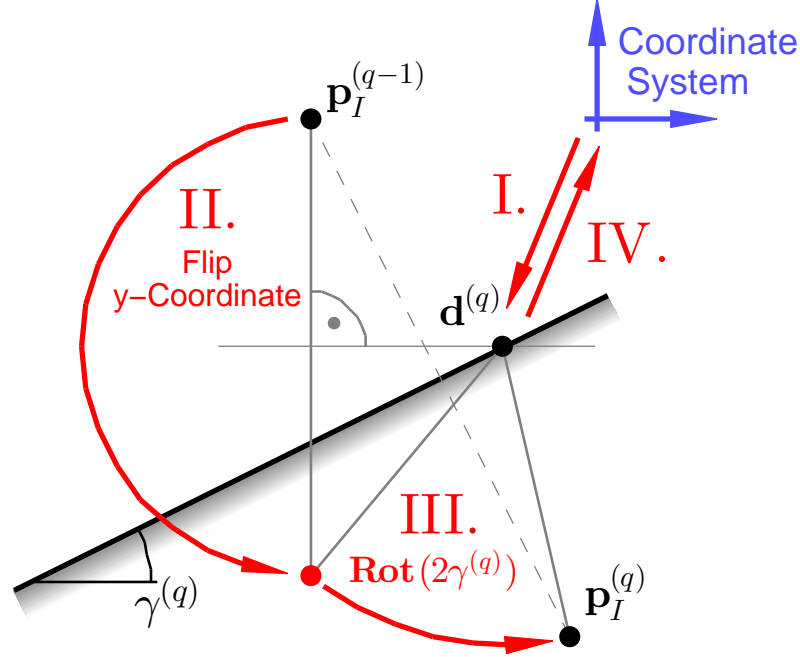


Figure 3.8: A more comprehensible way of mirroring: A y -coordinate flip and successive $2\gamma^{(q)}$ rotation of $\mathbf{p}_I^{(q-1)}$ produce its mirror image $\mathbf{p}_I^{(q)}$ about the wall when the coordinate origin was moved on the wall. The four steps are labeled in (3.9). This arrangement is a suitable starting point for a geometric proof of correctness of mirroring formula (3.7), which was omitted in favour of the given constructive proof though.

A recursive analysis gives a complicated formula for \mathbf{p}_{VA} as a function of \mathbf{p}_{TX} and the parameters of all involved walls

$$\begin{aligned} \mathbf{p}_{VA} = \mathbf{p}_I^{(Q)} &= \text{Mir} \left(\mathbf{p}_I^{(Q-1)}, \gamma^{(Q)}, \mathbf{d}^{(Q)} \right) \\ &= \text{Mir} \left(\text{Mir} \left(\mathbf{p}_I^{(Q-2)}, \gamma^{(Q-1)}, \mathbf{d}^{(Q-1)} \right), \gamma^{(Q)}, \mathbf{d}^{(Q)} \right) \\ &= \text{Mir} \left(\text{Mir} \left(\dots \text{Mir} \left(\text{Mir} \left(\mathbf{p}_{TX}, \gamma^{(1)}, \mathbf{d}^{(1)} \right), \gamma^{(2)}, \mathbf{d}^{(2)} \right), \dots, \gamma^{(Q-1)}, \mathbf{d}^{(Q-1)} \right), \gamma^{(Q)}, \mathbf{d}^{(Q)} \right) \end{aligned}$$

Using (3.12), this reads

$$\begin{aligned} \mathbf{p}_{VA} &= \mathbf{M}(\gamma^{(Q)}) \mathbf{p}_I^{(Q-1)} + (\mathbf{I} - \mathbf{M}(\gamma^{(Q)})) \mathbf{d}^{(Q)} \\ &= \mathbf{M}(\gamma^{(Q)}) \mathbf{M}(\gamma^{(Q-1)}) \mathbf{p}_I^{(Q-2)} + \mathbf{M}(\gamma^{(Q)}) (\mathbf{I} - \mathbf{M}(\gamma^{(Q-1)})) \mathbf{d}^{(Q-1)} + (\mathbf{I} - \mathbf{M}(\gamma^{(Q)})) \mathbf{d}^{(Q)} \\ &= \dots \end{aligned}$$

and when carefully breaking this down until $\mathbf{p}_I^{(0)} = \mathbf{p}_{TX}$, we ultimately obtain a formula^{14,15} for the VA position

$$\mathbf{p}_{VA} = \underbrace{\left(\prod_{q=0}^{Q-1} \mathbf{M}(\gamma^{(Q-q)}) \right)}_{= \partial \mathbf{p}_{VA} / \partial \mathbf{p}_{TX}} \mathbf{p}_{TX} + \sum_{q=1}^Q \left(\prod_{\tilde{q}=1}^{Q-q} \mathbf{M}(\gamma^{(Q+1-\tilde{q})}) \right) (\mathbf{I} - \mathbf{M}(\gamma^{(q)})) \mathbf{d}^{(q)}. \quad (3.13)$$

The above formula is inconvenient but fortunately we have little interest in the exact position \mathbf{p}_{VA} as such, but rather in its derivative w.r.t. \mathbf{p}_{TX} , which is simply the tagged factor of \mathbf{p}_{TX} in (3.13). The residual summand does not depend on \mathbf{p}_{TX} and thus vanishes during differentiation.

Preliminary result for the Jacobian of VA position w.r.t. TX position

$$\frac{\partial \mathbf{p}_{\text{VA}}}{\partial \mathbf{p}_{\text{TX}}} = \prod_{q=0}^{Q-1} \mathbf{M}(\gamma^{(Q-q)}) \quad (3.14)$$

This long product of mirror matrices motivates the next section, where we will study properties thereof to find further simplifications.

3.4 Mirror Matrix Properties

The goal of this section is finding a mirror matrix property that enables simplification of the mirror matrix product (3.14). The similarities to rotation matrices allow for a homomorphism-style property that turns such a product into a single mirror matrix whose argument is a combination of the individual previous arguments. In the course, we analyse some mirroring specifics relevant to VA understanding.

Basic Properties and Relations to Rotation Matrices

Let us write the mirror matrix definition (3.11) again

$$\mathbf{M}(\gamma) = \begin{pmatrix} \cos(2\gamma) & \sin(2\gamma) \\ \sin(2\gamma) & -\cos(2\gamma) \end{pmatrix}.$$

It is obviously a symmetric matrix

$$\mathbf{M}(\gamma) = \mathbf{M}(\gamma)^T. \quad (3.15)$$

Some distinctive values are given by

$$\forall m \in \mathbb{Z}, b \in \{0, 1\} : \quad \mathbf{M}\left(m\pi + b \cdot \frac{\pi}{2}\right) = (-1)^b \begin{pmatrix} 1 & 0 \\ 0 & -1 \end{pmatrix}$$

Earlier in the text near (3.9), we outlined that the linear map represented by the mirror matrix is equivalent to first flipping the y-coordinate of a vector and then doing a 2γ rotation.¹⁶

¹⁴ An empty product equals the identity element of multiplication: $\prod_{\tilde{q}=1}^0 f(\tilde{q}) = 1$.

¹⁵ The cumbersome inverse indexing of the $\gamma^{(\dots)}$ parameters in the products is required for assuring the proper matrix multiplication order from left to right since we are dealing with non-commutative matrices.

¹⁶ Because of the close relation, mirroring is also referred to as improper rotation or rotoinversion in geometry. Linear maps of proper and improper rotation are isometric (i.e., distance preserving) and therefore important elements of the well-studied Euclidean group [33]. Results from that mathematical field could be beneficial for further research on the influence of room geometry on localization performance, especially for the extension to three-dimensional multipath-assisted anchorless localization.

A mirror matrix is a composition of a 2γ -rotation and a sign flip in the second dimension

$$\mathbf{M}(\gamma) = \mathbf{Rot}(2\gamma) \begin{pmatrix} 1 & 0 \\ 0 & -1 \end{pmatrix} \quad (3.16)$$

$\mathbf{Rot}(2\gamma)$ is our notation for a standard angle 2γ rotation matrix [1]

$$\mathbf{Rot}(\gamma) := \begin{pmatrix} \cos(\gamma) & -\sin(\gamma) \\ \sin(\gamma) & \cos(\gamma) \end{pmatrix}$$

which is a homomorphism and an orthogonal matrix [1]

$$\begin{aligned} \mathbf{Rot}(\gamma)\mathbf{Rot}(\beta) &= \mathbf{Rot}(\gamma + \beta) \\ \mathbf{Rot}(\gamma)^T &= \mathbf{Rot}(\gamma)^{-1} = \mathbf{Rot}(-\gamma) . \end{aligned} \quad (3.17)$$

The numerical matrix on the right-hand side of (3.16) represents a sign-flip in the y-coordinate. Mirror matrices are orthogonal and self-inverse

$$\mathbf{M}(\gamma)^T \mathbf{M}(\gamma) = \mathbf{I} \quad \iff \quad \mathbf{M}(\gamma)^T = \mathbf{M}(\gamma)^{-1} \quad \iff \quad \mathbf{M}(\gamma) = \mathbf{M}(\gamma)^{-1} \quad (3.18)$$

which is intuitively clear because mirroring twice does not achieve anything, i.e. the composition of two equal mirror maps equals the identity map.

The numeric sign-flip matrix on the right-hand matrix of (3.16) will often occur in derivations. It is a mirror matrix as well

$$\begin{pmatrix} 1 & 0 \\ 0 & -1 \end{pmatrix} = \mathbf{M}(0)$$

and thus has all mirror matrix properties: It is symmetric, orthogonal, and self-inverse as well.

Proof of (3.18):

$$\begin{aligned} \mathbf{M}(\gamma)\mathbf{M}(\gamma)^T &= \mathbf{Rot}(2\gamma) \begin{pmatrix} 1 & 0 \\ 0 & -1 \end{pmatrix} \begin{pmatrix} 1 & 0 \\ 0 & -1 \end{pmatrix}^T \mathbf{Rot}(2\gamma)^T \\ &= \mathbf{Rot}(2\gamma) \cdot \mathbf{I} \cdot \mathbf{Rot}(-2\gamma) = \mathbf{Rot}(2\gamma - 2\gamma) = \mathbf{Rot}(0) = \mathbf{I} \end{aligned}$$

and $\mathbf{M}(\gamma)^2 = \mathbf{M}(\gamma)\mathbf{M}(\gamma)^T = \mathbf{I}$ follows from (3.15). □

Diagonalization and Eigenvalues

The mirror matrix can be diagonalized [1] via

$$\begin{aligned} \mathbf{M}(\gamma) &= \mathbf{Rot}(\gamma + \gamma) \begin{pmatrix} 1 & 0 \\ 0 & -1 \end{pmatrix} = \mathbf{Rot}(\gamma)\mathbf{Rot}(\gamma) \begin{pmatrix} 1 & 0 \\ 0 & -1 \end{pmatrix} \\ &= \begin{pmatrix} \cos(\gamma) & -\sin(\gamma) \\ \sin(\gamma) & \cos(\gamma) \end{pmatrix} \begin{pmatrix} \cos(\gamma) & \sin(\gamma) \\ \sin(\gamma) & -\cos(\gamma) \end{pmatrix} \end{aligned}$$

Mirror Matrix Diagonalization

$$\mathbf{M}(\gamma) = \begin{pmatrix} \cos(\gamma) & \sin(\gamma) \\ \sin(\gamma) & -\cos(\gamma) \end{pmatrix}^T \begin{pmatrix} 1 & 0 \\ 0 & -1 \end{pmatrix} \begin{pmatrix} \cos(\gamma) & \sin(\gamma) \\ \sin(\gamma) & -\cos(\gamma) \end{pmatrix} \quad (3.19)$$

Diagonalization (3.19) reveals eigenvalues λ_i (in the diagonal of the center matrix) and eigenvectors \mathbf{v}_i (in the columns of both bordering matrices) of the mirror matrix. We interpret the two eigenvectors in the following way:

- Eigenvector $\mathbf{v}_1 = (\cos(\gamma), \sin(\gamma))^T = \mathbf{e}(\gamma)$ points alongside the wall and is invariant under mirroring, thus $\lambda_1 = +1$.
- Eigenvector $\mathbf{v}_2 = (\sin(\gamma), -\cos(\gamma))^T = \mathbf{e}(\gamma - \pi/2)$ represents components orthogonal to the wall. Those will be projected onto the other side of the wall, i.e. its negative vector value, thus $\lambda_2 = -1$.

With the gained insights, we can show some characteristic properties of the mirroring function (3.12) in an elegant fashion:

- Moving a distance $l \in \mathbb{R}$ parallel to the wall will move the mirror image in the same direction:

$$\mathbf{Mir}(\mathbf{p} + l \cdot \mathbf{e}(\gamma), \gamma, \mathbf{d}) = \mathbf{Mir}(\mathbf{p}, \gamma, \mathbf{d}) + l \cdot \mathbf{e}(\gamma) \quad (3.20)$$

- Moving a distance $l \in \mathbb{R}$ orthogonal to the wall will move the mirror image in the opposite direction:

$$\mathbf{Mir}(\mathbf{p} + l \cdot \mathbf{e}(\gamma - \pi/2), \gamma, \mathbf{d}) = \mathbf{Mir}(\mathbf{p}, \gamma, \mathbf{d}) + l \cdot \mathbf{e}(\gamma + \pi/2) \quad (3.21)$$

- The choice of wall offset \mathbf{d} is ambiguous and any \mathbf{d} on the wall is equally suitable:

$$\mathbf{Mir}(\mathbf{p}, \gamma, \mathbf{d} + l \cdot \mathbf{e}(\gamma)) = \mathbf{Mir}(\mathbf{p}, \gamma, \mathbf{d}) \quad (3.22)$$

Proof of (3.20), (3.21), (3.22): All three statements rely on $\mathbf{e}(\gamma)$ and $\mathbf{e}(\gamma - \pi/2)$ being eigenvectors of $\mathbf{M}(\gamma)$ and thus $\mathbf{M}(\gamma) \cdot \mathbf{e}(\gamma) = \mathbf{e}(\gamma)$ and $\mathbf{M}(\gamma) \cdot \mathbf{e}(\gamma - \pi/2) = -\mathbf{e}(\gamma - \pi/2) = \mathbf{e}(\gamma + \pi/2)$. We will give a full proof for (3.20) because the two remaining proofs are alike. We use the simplest mirroring function definition (3.7):

$$\begin{aligned} \mathbf{Mir}(\mathbf{p} + l \cdot \mathbf{e}(\gamma), \gamma, \mathbf{d}) &= \mathbf{M}(\gamma) \cdot (\mathbf{p} + l \cdot \mathbf{e}(\gamma) - \mathbf{d}) + \mathbf{d} = \mathbf{M}(\gamma) \cdot (\mathbf{p} - \mathbf{d}) + \mathbf{d} + l \cdot \mathbf{M}(\gamma) \cdot \mathbf{e}(\gamma) \\ &= \mathbf{M}(\gamma) \cdot (\mathbf{p} - \mathbf{d}) + \mathbf{d} + l \cdot \mathbf{e}(\gamma) = \mathbf{Mir}(\mathbf{p}, \gamma, \mathbf{d}) + l \cdot \mathbf{e}(\gamma) \end{aligned}$$

□

Pseudo-Homomorphism Property

Feeding the mirror matrix with a negative argument flips the signs of the off-diagonal sine functions, which manifests as

$$\mathbf{M}(-\gamma) = \begin{pmatrix} 1 & 0 \\ 0 & -1 \end{pmatrix} \mathbf{M}(\gamma) \begin{pmatrix} 1 & 0 \\ 0 & -1 \end{pmatrix}. \quad (3.23)$$

Pseudo-homomorphism¹⁷ property of mirror matrices

$$\mathbf{M}(\gamma)\mathbf{M}(\beta) = \mathbf{M}(\gamma - \beta) \begin{pmatrix} 1 & 0 \\ 0 & -1 \end{pmatrix} = \begin{pmatrix} 1 & 0 \\ 0 & -1 \end{pmatrix} \mathbf{M}(\beta - \gamma) = \mathbf{Rot}(2(\gamma - \beta)) \quad (3.24)$$

Proof of (3.24): We start with the left-hand expression and transpose $\mathbf{M}(\beta)$ while maintaining equality because of (3.18) and furthermore use (3.16) and (3.17) to obtain

$$\begin{aligned} \mathbf{M}(\gamma)\mathbf{M}(\beta) &= \mathbf{M}(\gamma)\mathbf{M}(\beta)^T = \mathbf{Rot}(2\gamma) \begin{pmatrix} 1 & 0 \\ 0 & -1 \end{pmatrix} \begin{pmatrix} 1 & 0 \\ 0 & -1 \end{pmatrix}^T \mathbf{Rot}(2\beta)^T \\ &= \mathbf{Rot}(2\gamma) \cdot \mathbf{I} \cdot \mathbf{Rot}(-2\beta) = \mathbf{Rot}(2(\gamma - \beta)) \end{aligned}$$

The remaining conjectures follow from (3.16) and (3.23). \square

Application to Products occurring in the Jacobian

Result (3.24) is the key property that, when applied repeatedly, allows us to resolve arbitrary products of mirror matrices like the Jacobian (3.14) in particular. We deduce

$$\begin{aligned} \frac{\partial \mathbf{p}_{\text{VA}}}{\partial \mathbf{p}_{\text{TX}}} &= \prod_{q=0}^{Q-1} \mathbf{M}(\gamma^{(Q-q)}) = \mathbf{M}(\gamma^{(Q)})\mathbf{M}(\gamma^{(Q-1)}) \dots \mathbf{M}(\gamma^{(2)})\mathbf{M}(\gamma^{(1)}) \\ &= \mathbf{M}(\gamma^{(Q)})\mathbf{M}(\gamma^{(Q-1)}) \dots \mathbf{M}(\gamma^{(2)} - \gamma^{(1)}) \cdot \begin{pmatrix} 1 & 0 \\ 0 & -1 \end{pmatrix} \\ &= \mathbf{M} \left(\gamma^{(Q)} - \gamma^{(Q-1)} + \dots + (-1)^{Q-2} \gamma^{(2)} + (-1)^{Q-1} \gamma^{(1)} \right) \cdot \begin{pmatrix} 1 & 0 \\ 0 & -1 \end{pmatrix}^{Q-1} \end{aligned}$$

or in short

$$\begin{aligned} \frac{\partial \mathbf{p}_{\text{VA}}}{\partial \mathbf{p}_{\text{TX}}} &= \mathbf{M} \left(\sum_{q=1}^Q (-1)^{Q-q} \gamma^{(q)} \right) \cdot \begin{pmatrix} 1 & 0 \\ 0 & -1 \end{pmatrix}^{Q-1} \\ &= \mathbf{M}(\gamma_{\text{eff}}) \cdot \begin{pmatrix} 1 & 0 \\ 0 & -1 \end{pmatrix}^{Q-1} = \mathbf{Rot}(2\gamma_{\text{eff}}) \cdot \begin{pmatrix} 1 & 0 \\ 0 & -1 \end{pmatrix}^Q \end{aligned}$$

where we implicitly defined a symbol γ_{eff} for the sign-flipped sum of angles $\gamma^{(q)}$. From now on, we will call γ_{eff} the effective wall angle of the MPC. We recall the self-inverse property of the sign-flip matrix and obtain

$$\frac{\partial \mathbf{p}_{\text{VA}}}{\partial \mathbf{p}_{\text{TX}}} = \mathbf{Rot}(2\gamma_{\text{eff}}) \cdot \begin{pmatrix} 1 & 0 \\ 0 & (-1)^Q \end{pmatrix}. \quad (3.25)$$

The next section will restate result (3.25) and the effective angle in the complete notation and use them in the preliminary gradient delay result (3.4) to work towards a final result and an analysis thereof. For brevity and required space for other indices, we will drop the subscript of γ_{eff} .

¹⁷ 'Pseudo-homomorphism' is not an established term. We introduce the term because a functional equation of the type $f(x) \cdot f(y) = f(x - y) \cdot A$ holds for \mathbf{M} , which is similar yet still fundamentally different from the functional equation $f(x) \cdot f(y) = f(x + y)$ of a classical group homomorphism like \mathbf{Rot} .

3.5 Spatial Delay Gradient: Final Result

We switch back to the complete notation and restate result (3.25).

$\gamma_{m,j}^{(k)}$ is the effective wall angle of an MPC of order $Q_{m,j}^{(k)}$. It is the sum of alternating walls angles of involved walls

$$\gamma_{m,j}^{(k)} = \sum_{q=1}^{Q_{m,j}^{(k)}} (-1)^{Q_{m,j}^{(k)}-q} \cdot \gamma_{m,j}^{(k,q)}. \quad (3.26)$$

The Jacobian of a VA position $\mathbf{p}_{m,j}^{(k)}$ w.r.t. to the position of its TX \mathbf{p}_j is a rotation by the effective wall angle and a possible preceding sign flip in the second dimension depending on the parity of MPC order $Q_{m,j}^{(k)}$

$$\frac{\partial \mathbf{p}_{m,j}^{(k)}}{\partial \mathbf{p}_j} = \mathbf{Rot}(2\gamma_{m,j}^{(k)}) \cdot \begin{pmatrix} 1 & 0 \\ 0 & (-1)^{Q_{m,j}^{(k)}} \end{pmatrix}. \quad (3.27)$$

After our long excursus to room geometry and consecutive mirroring, we can finally return to the spatial delay gradient and use (3.27) to refine our preliminary result (3.4) as

$$\begin{aligned} \frac{\partial \tau_{m,j}^{(k)}}{\partial \mathbf{p}_\eta} &= \frac{1}{c} \left(\delta_{m,\eta} \cdot \mathbf{I} - \delta_{\eta,j} \cdot \frac{\partial \mathbf{p}_{m,j}^{(k)}}{\partial \mathbf{p}_j} \right) \mathbf{e}(\phi_{m,j}^{(k)}) \\ &= \frac{1}{c} \left(\delta_{m,\eta} \cdot \mathbf{I} - \delta_{\eta,j} \cdot \mathbf{Rot}(2\gamma_{m,j}^{(k)}) \begin{pmatrix} 1 & 0 \\ 0 & (-1)^{Q_{m,j}^{(k)}} \end{pmatrix} \right) \mathbf{e}(\phi_{m,j}^{(k)}) \\ &= \frac{1}{c} \left(\delta_{m,\eta} \cdot \mathbf{e}(\phi_{m,j}^{(k)}) - \delta_{\eta,j} \cdot \mathbf{Rot}(2\gamma_{m,j}^{(k)}) \cdot \mathbf{e}((-1)^{Q_{m,j}^{(k)}} \cdot \phi_{m,j}^{(k)}) \right). \end{aligned}$$

Spatial Gradient of Propagation Delay

$$\frac{\partial \tau_{m,j}^{(k)}}{\partial \mathbf{p}_\eta} = \frac{1}{c} \left(\delta_{m,\eta} \cdot \mathbf{e}(\phi_{m,j}^{(k)}) - \delta_{\eta,j} \cdot \mathbf{e}((-1)^{Q_{m,j}^{(k)}} \cdot \phi_{m,j}^{(k)} + 2\gamma_{m,j}^{(k)}) \right) \quad (3.28)$$

We analyze and interpret all four cases indicated by the Kronecker deltas. Expression (3.28) consists of a $\delta_{m,\eta}$ -masked unit vector that is a consequence of the propagation delay depending on RX positioning and a $\delta_{\eta,j}$ -masked unit vector reflecting dependence on VA locations and TX positioning subsequently (MPCs) or TX positioning directly (LOS path). In a thorough case-by-case analysis thereof we give the specific outcomes of (3.28):

- $\eta \neq m, \eta \neq j$: Unrelated agent case, gradient is zero.
- $\eta \neq m, \eta = j$: Bistatic case w.r.t. TX

$$\frac{\partial \tau_{m,j}^{(k)}}{\partial \mathbf{p}_j} = -\frac{1}{c} \mathbf{e}((-1)^{Q_{m,j}^{(k)}} \cdot \phi_{m,j}^{(k)} + 2\gamma_{m,j}^{(k)}) \quad (3.29)$$

- $\eta = m, \eta \neq j$: Bistatic case w.r.t. RX

$$\frac{\partial \tau_{m,j}^{(k)}}{\partial \mathbf{p}_m} = \frac{1}{c} \mathbf{e}(\phi_{m,j}^{(k)}) \quad (3.30)$$

- $\eta = m, \eta = j$: Monostatic case

$$\frac{\partial \tau_{j,j}^{(k)}}{\partial \mathbf{p}_j} = \frac{1}{c} \left(\mathbf{e}(\phi_{j,j}^{(k)}) - \mathbf{e}((-1)^{Q_{j,j}^{(k)}} \cdot \phi_{j,j}^{(k)} + 2\gamma_{j,j}^{(k)}) \right) \quad (3.31)$$

$$= \begin{cases} \frac{2}{c} \cdot \sin(\gamma_{j,j}^{(k)}) \cdot \mathbf{e}(\gamma_{j,j}^{(k)} + \phi_{j,j}^{(k)} - \frac{\pi}{2}) & \text{if } Q_{j,j}^{(k)} \text{ is even} \\ \frac{2}{c} \cdot \sin(\gamma_{j,j}^{(k)} - \phi_{j,j}^{(k)}) \cdot \mathbf{e}(\gamma_{j,j}^{(k)} - \frac{\pi}{2}) & \text{if } Q_{j,j}^{(k)} \text{ is odd} \end{cases} \quad (3.32)$$

Expression (3.32) is a sometimes useful magnitude-times-direction result rather than the vector-minus-vector result (3.31). The proof of (3.32) can be found in Appendix A.2.

Interpretation of bistatic LOS Transmissions

In Section 3.1, we defined that the LOS path of a bistatic transmission is considered as a 0-th order MPC. The formal consequences are

$$Q_{m,j}^{(k)} = 0 \quad \implies \quad \mathbf{p}_{m,j}^{(k)} = \mathbf{p}_j \quad \wedge \quad \gamma_{m,j}^{(k)} = 0 \quad (3.33)$$

where the vanishing effective wall angle is due to (3.26) becoming an empty sum. Hence, the delay gradient w.r.t. TX (3.29) becomes

$$\frac{\partial \tau_{m,j}^{(k)}}{\partial \mathbf{p}_j} = -\frac{1}{c} \mathbf{e}((-1)^0 \cdot \phi_{m,j}^{(k)} + 2 \cdot 0) = -\frac{1}{c} \mathbf{e}(\phi_{m,j}^{(k)}) .$$

In consideration of the similar result (3.30) for bistatic delay gradients w.r.t. RX position (which was anticipated in (3.5)), we notice that for any unobstructed bistatic LOS transmission, the equality

$$\frac{\partial \tau_{m,j}^{(k)}}{\partial \mathbf{p}_m} = -\frac{\partial \tau_{m,j}^{(k)}}{\partial \mathbf{p}_j} = \frac{1}{c} \mathbf{e}(\phi_{m,j}^{(k)}) \quad (3.34)$$

holds. The equality is trivial if you imagine a one-dimensional setup with RX x_m and TX x_j on the real number line where $x_m > x_j$ so that the distance between them is $c \cdot \tau_{m,j} = x_m - x_j$. Cooperative localization techniques without multipath-assistance [2] focus on the LOS path, so in CRLB derivations thereof (3.34) solves the geometry influence.

4

Monostatic Localization

4.1 Monostatic Cramér–Rao Lower Bound

Without loss of generality, we observe a fixed agent j with an a-priori unknown position \mathbf{p}_j . The agent is both transmitter (TX) and receiver (RX) and performs a monostatic measurement $r_{j,j}(t)$ that includes $K_{j,j}$ multipath components (MPCs). Our goal is to find the Cramér-Rao lower bound (CRLB) for the variance of an unbiased position estimator $\hat{\mathbf{p}}_j$ that uses the sampled observation $\mathbf{r}_{j,j}$.¹⁸ There is no line of sight (LOS) component, i.e. $\forall k \in \{1, \dots, K_{j,j}\} : Q_{j,j}^{(k)} \geq 1$.

4.1.1 Monostatic CRLB Derivation

With the knowledge earned in preceding chapters, the CRLB derivation for multipath-assisted monostatic indoor localization is straightforward and analogous to the derivations by Witrissal et.al [6]. The main difference is the Jacobian used in the parameter transformation, but the contained spatial delay gradients of MPCs already received a thorough examination in Chapter 3 and can be adopted without further effort.

We recall stack vectors (2.7) and (2.8) of all MPC delays and amplitudes within a transmission and write their monostatic versions

$$\boldsymbol{\tau}_{j,j} := \left(\tau_{j,j}^{(1)}, \dots, \tau_{j,j}^{(K_{j,j})} \right)^T \quad (4.1)$$

$$\boldsymbol{\alpha}_{j,j} := \left(\alpha_{j,j}^{(1)}, \dots, \alpha_{j,j}^{(K_{j,j})} \right)^T. \quad (4.2)$$

For monostatic position estimation, we define a parameter vector $\boldsymbol{\theta}$ as in [6]: A stack of the desired agent position plus all MPC amplitudes as nuisance parameters. We use real and imaginary parts of the latter to avoid complex derivatives.

$$\boldsymbol{\theta} := \left(\mathbf{p}_j^T, \Re \boldsymbol{\alpha}_{j,j}^T, \Im \boldsymbol{\alpha}_{j,j}^T \right)^T \in \mathbb{R}^{2+2K_{j,j}} \quad (4.3)$$

¹⁸ The omnipresent \square_j and $\square_{j,j}$ indexing may be confusing, but no actions towards a simpler notation were taken to maintain consistency with the cooperative notation of Chapter 2, 3, and 5 and because the derivation in this section is rather short.

As outlined in Section 2.3, we do a transformation to a higher-dimensional parameter $\boldsymbol{\psi}$. The corresponding Fisher information matrix (FIM) $\mathbf{J}_\boldsymbol{\psi}$ was solved in [6] and is simpler than $\mathbf{J}_\boldsymbol{\theta}$ because $\boldsymbol{\psi}$ consists of parameters directly used by the signal model (2.3) and the likelihood function (LHF) (2.5).

$$\boldsymbol{\psi} := (\boldsymbol{\tau}_{j,j}^T, \Re\boldsymbol{\alpha}_{j,j}^T, \Im\boldsymbol{\alpha}_{j,j}^T)^T \in \mathbb{R}^{3K_{j,j}} \quad (4.4)$$

We use the channel model described in Section 2.2, which assumes additive white Gaussian noise (AWGN) and diffuse multipath (DMP). Thus, $\mathbf{r}_{j,j}$ is described by $f(\mathbf{r}_{j,j}|\boldsymbol{\tau}_{j,j}, \boldsymbol{\alpha}_{j,j})$ given by the LHF (2.5) with $m = j$.¹⁹

Furthermore, we adopt a notation from [2] for FIMs (or blocks thereof) of some parameters \mathbf{x} , \mathbf{y} evaluated over the monostatic LHF (2.5) $f(\mathbf{r}_{j,j}|\boldsymbol{\tau}_{j,j}, \boldsymbol{\alpha}_{j,j})$.

$$\Phi_{j,j}(\mathbf{x}, \mathbf{y}) := \mathbb{E}_{\mathbf{r}_{j,j}|\boldsymbol{\tau}_{j,j}, \boldsymbol{\alpha}_{j,j}} \left\{ -\frac{\partial^2 \ln f(\mathbf{r}_{j,j}|\boldsymbol{\tau}_{j,j}, \boldsymbol{\alpha}_{j,j})}{\partial \mathbf{x} \partial \mathbf{y}^T} \right\} \quad (4.5)$$

The FIM for the support parameter vector $\boldsymbol{\psi}$ FIM is then

$$\mathbf{J}_\boldsymbol{\psi} = \Phi_{j,j}(\boldsymbol{\psi}, \boldsymbol{\psi}) = \begin{pmatrix} \Phi_{j,j}(\boldsymbol{\tau}_{j,j}, \boldsymbol{\tau}_{j,j}) & \Phi_{j,j}(\boldsymbol{\tau}_{j,j}, \Re\boldsymbol{\alpha}_{j,j}) & \Phi_{j,j}(\boldsymbol{\tau}_{j,j}, \Im\boldsymbol{\alpha}_{j,j}) \\ \Phi_{j,j}(\boldsymbol{\tau}_{j,j}, \Re\boldsymbol{\alpha}_{j,j})^T & \Phi_{j,j}(\Re\boldsymbol{\alpha}_{j,j}, \Re\boldsymbol{\alpha}_{j,j}) & 0 \\ \Phi_{j,j}(\boldsymbol{\tau}_{j,j}, \Im\boldsymbol{\alpha}_{j,j})^T & 0 & \Phi_{j,j}(\Im\boldsymbol{\alpha}_{j,j}, \Im\boldsymbol{\alpha}_{j,j}) \end{pmatrix} \quad (4.6)$$

FIM $\mathbf{J}_\boldsymbol{\psi}$ has a $K_{j,j} \times K_{j,j}$ block structure of matrices holding Fisher information (FI) within or among MPC parameters $\tau_{j,j}^{(k)}$ and $\alpha_{j,j}^{(k)}$. They were derived for our signal model in [6] and formulas are given in Appendix A.1.

According to [6], FI among real and imaginary parts of two different path amplitudes and even of one and the same path amplitude is always zero. Hence, the two concerned blocks in (4.6) (also in (4.7) below) vanished. Furthermore, equality $\Phi_{j,j}(\Re\boldsymbol{\alpha}_{j,j}, \Re\boldsymbol{\alpha}_{j,j}) = \Phi_{j,j}(\Im\boldsymbol{\alpha}_{j,j}, \Im\boldsymbol{\alpha}_{j,j})$ holds as shown by (A.2) or in [6].

The parameter vector of interest $\boldsymbol{\theta}$ gives rise to a FIM

$$\mathbf{J}_\boldsymbol{\theta} = \Phi_{j,j}(\boldsymbol{\theta}, \boldsymbol{\theta}) = \begin{pmatrix} \Phi_{j,j}(\mathbf{p}_j, \mathbf{p}_j) & \Phi_{j,j}(\mathbf{p}_j, \Re\boldsymbol{\alpha}_{j,j}) & \Phi_{j,j}(\mathbf{p}_j, \Im\boldsymbol{\alpha}_{j,j}) \\ \Phi_{j,j}(\mathbf{p}_j, \Re\boldsymbol{\alpha}_{j,j})^T & \Phi_{j,j}(\Re\boldsymbol{\alpha}_{j,j}, \Re\boldsymbol{\alpha}_{j,j}) & 0 \\ \Phi_{j,j}(\mathbf{p}_j, \Im\boldsymbol{\alpha}_{j,j})^T & 0 & \Phi_{j,j}(\Im\boldsymbol{\alpha}_{j,j}, \Im\boldsymbol{\alpha}_{j,j}) \end{pmatrix} \quad (4.7)$$

which is coupled with $\mathbf{J}_\boldsymbol{\psi}$ (4.6) through parameter transformation (2.11)

$$\mathbf{J}_\boldsymbol{\theta} = \frac{\partial \boldsymbol{\psi}}{\partial \boldsymbol{\theta}} \cdot \mathbf{J}_\boldsymbol{\psi} \cdot \frac{\partial \boldsymbol{\psi}^T}{\partial \boldsymbol{\theta}} \quad (4.8)$$

where the following Jacobian (same structure as in [6]) arises

$$\frac{\partial \boldsymbol{\psi}}{\partial \boldsymbol{\theta}} = \begin{pmatrix} \partial \boldsymbol{\tau}_{j,j} / \partial \mathbf{p}_j & \mathbf{0}_{2 \times 2K_{j,j}} \\ \mathbf{0}_{2K_{j,j} \times K_{j,j}} & \mathbf{I}_{2K_{j,j} \times 2K_{j,j}} \end{pmatrix}. \quad (4.9)$$

¹⁹ Actually, estimating parameter $\boldsymbol{\theta}$ dictates to use $f(\mathbf{r}_{j,j}|\boldsymbol{\theta}) = f(\mathbf{r}_{j,j}|\mathbf{p}_j, \boldsymbol{\alpha}_{j,j})$ for a CRLB derivation of this estimation problem. But since the assumed LHF (2.5) incorporates position \mathbf{p}_j only implicitly via delays $\tau_{j,j}^{(k)}$, which are functions of \mathbf{p}_j and the known room geometry, usage of $f(\mathbf{r}_{j,j}|\boldsymbol{\tau}_{j,j}, \boldsymbol{\alpha}_{j,j})$ for CRLB derivation is legitimate. Furthermore, in a well-posed localization problem, a bijection between the set of true delay values and agent position(s) exists.

The majority of blocks turns zero or unity due to basic rules of differential calculus. The only non-trivial block of $\partial\psi/\partial\theta$ is the Jacobian $\partial\tau_{j,j}/\partial\mathbf{p}_j$, which holds the spatial gradients of monostatic MPC delays. These complicated gradients account for room geometry and were solved in Chapter 3. Furthermore, FIM \mathbf{J}_ψ in (4.8) was already broken down in [6], so the rest of the derivation is straight forward.

A more specific expression for the FIM of θ is obtained through usage of (4.8), (4.9), (4.6) and matrix multiplication

$$\mathbf{J}_\theta = \begin{pmatrix} \frac{\partial\tau_{j,j}}{\partial\mathbf{p}_j} \cdot \Phi_{j,j}(\tau_{j,j}, \tau_{j,j}) \cdot \frac{\partial\tau_{j,j}}{\partial\mathbf{p}_j}^T & \frac{\partial\tau_{j,j}}{\partial\mathbf{p}_j} \cdot \Phi_{j,j}(\tau_{j,j}, \mathfrak{R}\alpha_{j,j}) & \frac{\partial\tau_{j,j}}{\partial\mathbf{p}_j} \cdot \Phi_{j,j}(\tau_{j,j}, \mathfrak{S}\alpha_{j,j}) \\ \Phi_{j,j}(\tau_{j,j}, \mathfrak{R}\alpha_{j,j})^T \cdot \frac{\partial\tau_{j,j}}{\partial\mathbf{p}_j}^T & \Phi_{j,j}(\mathfrak{R}\alpha_{j,j}, \mathfrak{R}\alpha_{j,j}) & \mathbf{0} \\ \Phi_{j,j}(\tau_{j,j}, \mathfrak{S}\alpha_{j,j})^T \cdot \frac{\partial\tau_{j,j}}{\partial\mathbf{p}_j}^T & \mathbf{0} & \Phi_{j,j}(\mathfrak{S}\alpha_{j,j}, \mathfrak{S}\alpha_{j,j}) \end{pmatrix} \quad (4.10)$$

To conclude the derivation, we compute the equivalent Fisher information matrix (EFIM) $\mathbf{J}_{\mathbf{p}_j} \in \mathbb{R}^{2 \times 2}$ of the position vector \mathbf{p}_j . The EFIM fulfills

$$[\mathbf{J}_\theta^{-1}]_{2 \times 2} = \mathbf{J}_{\mathbf{p}_j}^{-1}.$$

We obtain the EFIM by computing the Schur complement (2.12), which reads

$$\begin{aligned} \mathbf{J}_{\mathbf{p}_j} &= \frac{\partial\tau_{j,j}}{\partial\mathbf{p}_j} \cdot \Phi_{j,j}(\tau_{j,j}, \tau_{j,j}) \cdot \frac{\partial\tau_{j,j}}{\partial\mathbf{p}_j}^T - \begin{pmatrix} \frac{\partial\tau_{j,j}}{\partial\mathbf{p}_j} \cdot \Phi_{j,j}(\tau_{j,j}, \mathfrak{R}\alpha_{j,j}) & \frac{\partial\tau_{j,j}}{\partial\mathbf{p}_j} \cdot \Phi_{j,j}(\tau_{j,j}, \mathfrak{S}\alpha_{j,j}) \end{pmatrix} \\ &\quad \cdot \begin{pmatrix} \Phi_{j,j}(\mathfrak{R}\alpha_{j,j}, \mathfrak{R}\alpha_{j,j}) & \mathbf{0} \\ \mathbf{0} & \Phi_{j,j}(\mathfrak{S}\alpha_{j,j}, \mathfrak{S}\alpha_{j,j}) \end{pmatrix}^{-1} \cdot \begin{pmatrix} \left(\frac{\partial\tau_{j,j}}{\partial\mathbf{p}_j} \cdot \Phi_{j,j}(\tau_{j,j}, \mathfrak{R}\alpha_{j,j}) \right)^T \\ \left(\frac{\partial\tau_{j,j}}{\partial\mathbf{p}_j} \cdot \Phi_{j,j}(\tau_{j,j}, \mathfrak{S}\alpha_{j,j}) \right)^T \end{pmatrix} \\ &= \frac{\partial\tau_{j,j}}{\partial\mathbf{p}_j} \cdot \Phi_{j,j}(\tau_{j,j}, \tau_{j,j}) \cdot \frac{\partial\tau_{j,j}}{\partial\mathbf{p}_j}^T - \begin{pmatrix} \frac{\partial\tau_{j,j}}{\partial\mathbf{p}_j} \cdot \Phi_{j,j}(\tau_{j,j}, \mathfrak{R}\alpha_{j,j}) & \frac{\partial\tau_{j,j}}{\partial\mathbf{p}_j} \cdot \Phi_{j,j}(\tau_{j,j}, \mathfrak{S}\alpha_{j,j}) \end{pmatrix} \\ &\quad \cdot \begin{pmatrix} \Phi_{j,j}(\mathfrak{R}\alpha_{j,j}, \mathfrak{R}\alpha_{j,j})^{-1} & \mathbf{0} \\ \mathbf{0} & \Phi_{j,j}(\mathfrak{S}\alpha_{j,j}, \mathfrak{S}\alpha_{j,j})^{-1} \end{pmatrix} \cdot \begin{pmatrix} \Phi_{j,j}(\tau_{j,j}, \mathfrak{R}\alpha_{j,j})^T \cdot \frac{\partial\tau_{j,j}}{\partial\mathbf{p}_j}^T \\ \Phi_{j,j}(\tau_{j,j}, \mathfrak{S}\alpha_{j,j})^T \cdot \frac{\partial\tau_{j,j}}{\partial\mathbf{p}_j}^T \end{pmatrix} \\ &= \frac{\partial\tau_{j,j}}{\partial\mathbf{p}_j} \cdot \Phi_{j,j}(\tau_{j,j}, \tau_{j,j}) \cdot \frac{\partial\tau_{j,j}}{\partial\mathbf{p}_j}^T \\ &\quad - \frac{\partial\tau_{j,j}}{\partial\mathbf{p}_j} \cdot \Phi_{j,j}(\tau_{j,j}, \mathfrak{R}\alpha_{j,j}) \cdot \Phi_{j,j}(\mathfrak{R}\alpha_{j,j}, \mathfrak{R}\alpha_{j,j})^{-1} \cdot \Phi_{j,j}(\tau_{j,j}, \mathfrak{R}\alpha_{j,j})^T \cdot \frac{\partial\tau_{j,j}}{\partial\mathbf{p}_j}^T \\ &\quad - \frac{\partial\tau_{j,j}}{\partial\mathbf{p}_j} \cdot \Phi_{j,j}(\tau_{j,j}, \mathfrak{S}\alpha_{j,j}) \cdot \Phi_{j,j}(\mathfrak{S}\alpha_{j,j}, \mathfrak{S}\alpha_{j,j})^{-1} \cdot \Phi_{j,j}(\tau_{j,j}, \mathfrak{S}\alpha_{j,j})^T \cdot \frac{\partial\tau_{j,j}}{\partial\mathbf{p}_j}^T \\ &= \frac{\partial\tau_{j,j}}{\partial\mathbf{p}_j} \cdot \left(\Phi_{j,j}(\tau_{j,j}, \tau_{j,j}) \cdot \frac{\partial\tau_{j,j}}{\partial\mathbf{p}_j}^T \right. \\ &\quad \left. - \Phi_{j,j}(\tau_{j,j}, \mathfrak{R}\alpha_{j,j}) \cdot \Phi_{j,j}(\mathfrak{R}\alpha_{j,j}, \mathfrak{R}\alpha_{j,j})^{-1} \cdot \Phi_{j,j}(\tau_{j,j}, \mathfrak{R}\alpha_{j,j})^T \right. \\ &\quad \left. - \Phi_{j,j}(\tau_{j,j}, \mathfrak{S}\alpha_{j,j}) \cdot \Phi_{j,j}(\mathfrak{S}\alpha_{j,j}, \mathfrak{S}\alpha_{j,j})^{-1} \cdot \Phi_{j,j}(\tau_{j,j}, \mathfrak{S}\alpha_{j,j})^T \right) \cdot \frac{\partial\tau_{j,j}}{\partial\mathbf{p}_j}^T \end{aligned}$$

We used that the inverse of a block-diagonal matrix is a block-diagonal matrix as well and holds just the inverses of the original blocks [1]. We obtain the CRLB on the variance of x- and y-components of an unbiased position estimate $\hat{\mathbf{p}}_j$ from the on-diagonal matrix elements $[\mathbf{J}_{\mathbf{p}_j}^{-1}]_{1,1}$ and $[\mathbf{J}_{\mathbf{p}_j}^{-1}]_{2,2}$ respectively. The position error bound (PEB) is simply a Pythagorean combination thereof, which is invariant under rotations of the coordinate system [2].

4.1.2 Monostatic CRLB Result

EFIM of Monostatic Indoor Localization

$$\mathbf{J}_{\mathbf{p}_j} = \frac{\partial \boldsymbol{\tau}_{j,j}}{\partial \mathbf{p}_j} \cdot \boldsymbol{\Lambda}_{j,j} \cdot \frac{\partial \boldsymbol{\tau}_{j,j}^T}{\partial \mathbf{p}_j} \quad (4.11)$$

Fisher information (FI) among multipath delays, impaired by path overlap

$$\boldsymbol{\Lambda}_{j,j} = \Phi_{j,j}(\boldsymbol{\tau}_{j,j}, \boldsymbol{\tau}_{j,j}) - \Psi_{j,j}^{(\Re)} - \Psi_{j,j}^{(\Im)} \quad (4.12)$$

Spatial delay gradient of monostatic MPCs, cf. (3.31) (3.32)

$$\left[\frac{\partial \boldsymbol{\tau}_{j,j}}{\partial \mathbf{p}_j} \right]_{:,k} = \frac{\partial \tau_{j,j}^{(k)}}{\partial \mathbf{p}_j} = \frac{1}{c} \left(\mathbf{e}(\phi_{j,j}^{(k)}) - \mathbf{e}((-1)^{Q_{j,j}^{(k)}} \cdot \phi_{j,j}^{(k)} + 2\gamma_{j,j}^{(k)}) \right) \quad (4.13)$$

$$= \begin{cases} \frac{2}{c} \cdot \sin(\gamma_{j,j}^{(k)}) \cdot \mathbf{e}(\gamma_{j,j}^{(k)} + \phi_{j,j}^{(k)} - \frac{\pi}{2}) & \text{if } Q_{j,j}^{(k)} \text{ is even} \\ \frac{2}{c} \cdot \sin(\gamma_{j,j}^{(k)} - \phi_{j,j}^{(k)}) \cdot \mathbf{e}(\gamma_{j,j}^{(k)} - \frac{\pi}{2}) & \text{if } Q_{j,j}^{(k)} \text{ is odd} \end{cases} \quad (4.14)$$

Effective wall angle, cf. (3.26)

$$\gamma_{j,j}^{(k)} = \sum_{q=1}^{Q_{j,j}^{(k)}} (-1)^{Q_{j,j}^{(k)}-q} \cdot \gamma_{j,j}^{(k,q)}$$

The Squared position error bound (SPEB) and position error bound (PEB) of monostatic localization are described by

$$\text{SPEB}(\mathbf{p}_j) = \text{tr}\{\mathbf{J}_{\mathbf{p}_j}^{-1}\}, \quad \text{PEB}(\mathbf{p}_j) = \sqrt{\text{SPEB}(\mathbf{p}_j)}.$$

The influence of path overlap is given by

$$\begin{aligned} \Psi_{j,j}^{(\Re)} &:= \Phi_{j,j}(\boldsymbol{\tau}_{j,j}, \Re \boldsymbol{\alpha}_{j,j}) \cdot \Phi_{j,j}(\Re \boldsymbol{\alpha}_{j,j}, \Re \boldsymbol{\alpha}_{j,j})^{-1} \cdot \Phi_{j,j}(\boldsymbol{\tau}_{j,j}, \Re \boldsymbol{\alpha}_{j,j})^T. \\ \Psi_{j,j}^{(\Im)} &:= \Phi_{j,j}(\boldsymbol{\tau}_{j,j}, \Im \boldsymbol{\alpha}_{j,j}) \cdot \Phi_{j,j}(\Im \boldsymbol{\alpha}_{j,j}, \Im \boldsymbol{\alpha}_{j,j})^{-1} \cdot \Phi_{j,j}(\boldsymbol{\tau}_{j,j}, \Im \boldsymbol{\alpha}_{j,j})^T. \end{aligned}$$

Matrices $\Phi_{j,j}(\dots)$ are given in Appendix A.1. FI notation Φ is defined in (4.5). For MPC-related equations, $Q_{j,j}^{(k)}$ is the MPC order, $\phi_{j,j}^{(k)}$ the angle of arrival (AoA), and $\gamma_{j,j}^{(k,q)}$ are the wall angles involved in order $1 \leq q \leq Q_{j,j}^{(k)}$.

When pulses do not overlap or when we neglect the effect of path overlap (cf. Section 2.4), i.e. $\Psi_{j,j}^{(\Re)} = \mathbf{0}$ and $\Psi_{j,j}^{(\Im)} = \mathbf{0}$, then $\boldsymbol{\Lambda}_{j,j} = \Phi_{j,j}(\boldsymbol{\tau}_{j,j}, \boldsymbol{\tau}_{j,j})$ and the EFIM is simply $\mathbf{J}_{\mathbf{p}_j} = \frac{\partial \boldsymbol{\tau}_{j,j}}{\partial \mathbf{p}_j} \cdot \Phi_{j,j}(\boldsymbol{\tau}_{j,j}, \boldsymbol{\tau}_{j,j}) \cdot \frac{\partial \boldsymbol{\tau}_{j,j}^T}{\partial \mathbf{p}_j}$. This quantity consists of the two key figures of monostatic position

estimation: $\Phi_{j,j}(\boldsymbol{\tau}_{j,j}, \boldsymbol{\tau}_{j,j})$ holds FI among MPC delays $\tau_{j,j}^{(k)}$ while $\partial\boldsymbol{\tau}_{j,j}/\partial\mathbf{p}_j$ represents room geometry dependence on the delays.

The subtractive terms $-\Psi_{j,j}^{(\Re)}$ and $-\Psi_{j,j}^{(\Im)}$ in (4.12) describe the influence of estimated amplitude alpha $\hat{\alpha}_{j,j}^{(k)} \in \mathbb{C}$ on the EFIM. This could lead to an increase in the CRLB, i.e. a degradation of localization performance caused by poor estimation of the nuisance parameters.

4.2 Analysis of monostatic Virtual Anchors

In this section we investigate the contributions of individual monostatic virtual anchors (VAs) to localization. We adopt the concept of ranging information (RI) from [2, 4, 6, 12] which states that each VA provides one-dimensional RI along the eigenvector in direction of the AoA to the VA. In the mentioned literature, contributions always happen in direction of the AoA for reasons (3.5) (3.34). Our situation is different because of the vastly more intricate spatial delay gradient (4.13) (4.14) (or earlier (3.31) (3.32)).

Similar to [2, 4, 6, 12], we get a formula for the monostatic EFIM (4.11) as a sum of individual contributions from MPCs

$$\mathbf{J}_{\mathbf{p}_j} = 8\pi^2\beta^2 \sum_{k=1}^{K_{j,j}} \text{SINR}_{j,j}^{(k)} \cdot \frac{\partial\tau_{j,j}^{(k)}}{\partial\mathbf{p}_j} \cdot \frac{\partial\tau_{j,j}^{(k)T}}{\partial\mathbf{p}_j} \quad (4.15)$$

where β is the effective bandwidth [6, 23, 24] of pulse $s(t)$ and $\text{SINR}_{j,j}^{(k)}$ is the signal-to-interference-plus-noise ratio (SINR) [6] of the MPC in the received signal $r_{j,j}(t)$. The representation is valid when pulses do not overlap.

We temporarily encapsulate gradient (4.14) in a simpler magnitude-times-direction form

$$\frac{\partial\tau_{j,j}^{(k)}}{\partial\mathbf{p}_j} = \frac{1}{c} \cdot A_{j,j}^{(k)} \cdot \mathbf{e}(\mu_{j,j}^{(k)})$$

that just covers the even/odd distinction of (4.14) within symbols

$$A_{j,j}^{(k)} := \begin{cases} 2 \cdot \sin(\gamma_{j,j}^{(k)}) & \text{if } Q_{j,j}^{(k)} \text{ is even} \\ 2 \cdot \sin(\gamma_{j,j}^{(k)} - \phi_{j,j}^{(k)}) & \text{if } Q_{j,j}^{(k)} \text{ is odd} \end{cases}$$

$$\mu_{j,j}^{(k)} := \begin{cases} \gamma_{j,j}^{(k)} + \phi_{j,j}^{(k)} - \frac{\pi}{2} & \text{if } Q_{j,j}^{(k)} \text{ is even} \\ \gamma_{j,j}^{(k)} - \frac{\pi}{2} & \text{if } Q_{j,j}^{(k)} \text{ is odd} \end{cases}.$$

Hence, we obtain

$$\begin{aligned} \mathbf{J}_{\mathbf{p}_j} &= \frac{8\pi^2\beta^2}{c^2} \sum_{k=1}^{K_{j,j}} \text{SINR}_{j,j}^{(k)} \cdot (A_{j,j}^{(k)})^2 \cdot \mathbf{e}(\mu_{j,j}^{(k)}) \cdot \mathbf{e}(\mu_{j,j}^{(k)})^T \\ &= \frac{8\pi^2\beta^2}{c^2} \sum_{k=1}^{K_{j,j}} \text{SINR}_{j,j}^{(k)} \cdot (A_{j,j}^{(k)})^2 \cdot \mathbf{J}_r(\mu_{j,j}^{(k)}). \end{aligned} \quad (4.16)$$

Here, $\mathbf{J}_r(\mu)$ is the ranging direction matrix [2, 4] which has one non-zero eigenvalue with eigen-

vector $\mathbf{e}(\mu)$.

$$\mathbf{J}_r(\mu) := \begin{pmatrix} \cos^2(\mu) & \cos(\mu) \sin(\mu) \\ \cos(\mu) \sin(\mu) & \sin^2(\mu) \end{pmatrix}$$

Thus, any MPC contributes RI in direction $\mu_{j,j}^{(k)}$ of its delay gradient $\partial\tau_{j,j}^{(k)}/\partial\mathbf{p}_j$.

A uniqueness of monostatic localization is that its gradient is a sum of two vector components (4.13). These components can either cancel out ($A_{j,j}^{(k)} = 0$) or add up ($A_{j,j}^{(k)} = 2$) as shown by the factor 2 in (4.14). This is due to RX and TX being collocated, which couples agent positioning and VA positioning. Contributions from monostatic MPCs are ...

- ... in general not aligned with the AoA direction. Their direction depends on the multipath geometry defined by the effective wall angle (3.26).
- ... scaled by a factor $0 \leq (A_{j,j}^{(k)})^2 \leq 2^2$, which may amplify or nullify the contribution.

The bottom line of these RI considerations is that we can assess contributions from certain classes of MPCs to localization by looking at magnitude and direction of their delay gradient $\partial\tau_{j,j}^{(k)}/\partial\mathbf{p}_j$. The geometric setup will determine whether (4.13) or (4.14) is the better choice for investigation. For instance, (4.14) is convenient when the gradient vanishes for even order $Q_{j,j}^{(k)}$ because the magnitude term $\sin(\gamma_{j,j}^{(k)})$ immediately shows that this happens iff $\gamma_{j,j}^{(k)} = l\pi$, $l \in \mathbb{Z}$.

4.2.1 Significant Virtual Anchors

First Order VA

In this simple case, the effective wall angle (3.26) is just the only occurring wall angle, i.e. $\gamma_{j,j}^{(k)} = \gamma_{j,j}^{(k,1)}$. We use (4.13) with MPC order $Q_{j,j}^{(k)} = 1$

$$\frac{\partial\tau_{j,j}^{(k)}}{\partial\mathbf{p}_j} = \frac{1}{c} \left(\mathbf{e}(\phi_{j,j}^{(k)}) - \mathbf{e}(-\phi_{j,j}^{(k)} + 2\gamma_{j,j}^{(k,1)}) \right) \quad (4.17)$$

By the definition of wall mirroring, angles $\phi_{j,j}^{(k)}$ and $\gamma_{j,j}^{(k,1)}$ are orthogonal $\gamma_{j,j}^{(k,1)} = \phi_{j,j}^{(k)} \pm \frac{\pi}{2}$ and the gradient becomes

$$\frac{\partial\tau_{j,j}^{(k)}}{\partial\mathbf{p}_j} = \frac{1}{c} \left(\mathbf{e}(\phi_{j,j}^{(k)}) - \mathbf{e}(-\phi_{j,j}^{(k)} + 2\phi_{j,j}^{(k)} \pm \pi) \right) = \frac{1}{c} \left(\mathbf{e}(\phi_{j,j}^{(k)}) - \mathbf{e}(\phi_{j,j}^{(k)} \pm \pi) \right)$$

and thus

$$\frac{\partial\tau_{j,j}^{(k)}}{\partial\mathbf{p}_j} = \frac{2}{c} \mathbf{e}(\phi_{j,j}^{(k)}) \quad (4.18)$$

The resulting magnitude $2/c$ is twice the magnitude of gradients in fixed anchor localization [4, 6, 12]. The doubled sensitivity is due to the fact that the virtual anchor is moving in the opposite direction when the agent moves orthogonal to the wall. The direction reveals that first-order VAs provide position information exclusively orthogonal to the wall. The setup and all deduced properties are illustrated in Figure 4.1.

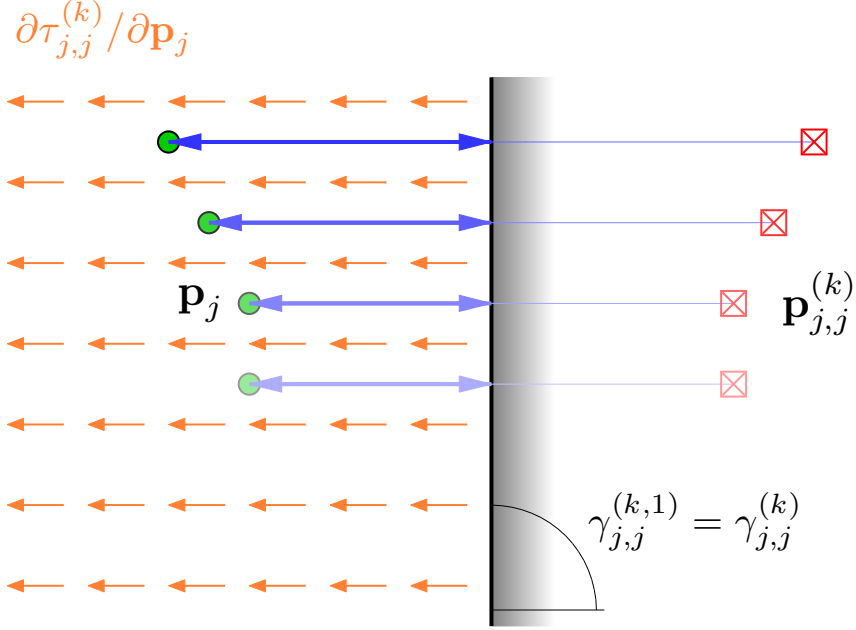


Figure 4.1: The sketch shows a monostatic first-order MPC of an agent at varying position \mathbf{p}_j . The fading effect indicates agent movement. The VA position $\mathbf{p}_{j,j}^{(k)}$ is the mirror image of \mathbf{p}_j w.r.t. to the wall with angle $\gamma_{j,j}^{(k,1)}$. The thick blue arrows show the reflection path while the thin line extends from VA to agent (direct path). The spatial delay gradient field, whose direction is equal to the RI contribution, is shown in orange and is perpendicular to the wall.

Further insights are provided by the directional derivative of $\tau_{j,j}^{(k)}$ in direction of an arbitrary angle ξ .

$$\begin{aligned} D_{\mathbf{e}(\xi)}\tau_{j,j}^{(k)} &= \left\langle \frac{\partial \tau_{j,j}^{(k)}}{\partial \mathbf{p}_j}, \mathbf{e}(\xi) \right\rangle = \frac{2}{c} \cdot \left\langle \begin{pmatrix} \cos(\phi_{j,j}^{(k)}) \\ \sin(\phi_{j,j}^{(k)}) \end{pmatrix}, \begin{pmatrix} \cos(\xi) \\ \sin(\xi) \end{pmatrix} \right\rangle \\ &= \frac{2}{c} \cdot (\cos(\phi_{j,j}^{(k)}) \cos(\xi) + \sin(\phi_{j,j}^{(k)}) \sin(\xi)) \\ &= \frac{2}{c} \cdot (\cos(-\phi_{j,j}^{(k)}) \cos(\xi) - \sin(-\phi_{j,j}^{(k)}) \sin(\xi)) = \frac{2}{c} \cos(\xi - \phi_{j,j}^{(k)}) . \end{aligned}$$

The directional derivative result allows to formally show that agent movements in parallel with the wall do not affect the propagation delay

$$\xi \in \left\{ \gamma_{j,j}^{(k,1)}, \gamma_{j,j}^{(k,1)} + \pi \right\} \implies D_{\mathbf{e}(\xi)}\tau_{j,j}^{(k)} = 0 .$$

Movements orthogonal to the wall affect the delay most

$$\begin{aligned} \xi = \phi_{j,j}^{(k)} &\implies D_{\mathbf{e}(\xi)}\tau_{j,j}^{(k)} = +\frac{2}{c} \\ \xi = \phi_{j,j}^{(k)} + \pi &\implies D_{\mathbf{e}(\xi)}\tau_{j,j}^{(k)} = -\frac{2}{c} . \end{aligned}$$

These properties explain the constant gradient field in Figure 4.1 and were already addressed with a different, less graphic approach in (3.20) and (3.21).

Second-Order Corner VA

Monostatic second-order VAs constituted by a perpendicular wall corner are special for several reasons:

- Two walls give rise to two second-order MPCs (reflection path $\mathbf{p}_j \rightarrow \text{wall 1} \rightarrow \text{wall 2} \rightarrow \mathbf{p}_j$ and vice versa). The resulting VAs will be in the same position and can be merged, i.e. considered as a single VA. To emphasize this property, the initial anchors of both construction sequences were kept in Figure 4.2.
- Physically, only a single reflection takes place and the ray from wall to wall has length zero (cf. Figure 4.2).
- The effective wall angle $\gamma_{j,j}^{(k)} = \pm \frac{\pi}{2}$ maximizes the gradient magnitude (4.13), previously also denoted as $A_{j,j}^{(k)}$, for even $Q_{j,j}^{(k)}$.
- For any corner angle $\frac{\pi}{2} + \epsilon$ with $\epsilon > 0$, the reflection path would be infeasible.

Because of the perpendicularity $\gamma_{j,j}^{(k,2)} = \gamma_{j,j}^{(k,1)} \pm \frac{\pi}{2}$ and $\gamma_{j,j}^{(k)} = \gamma_{j,j}^{(k,2)} - \gamma_{j,j}^{(k,1)} = \pm \frac{\pi}{2}$. We use (4.13) and get

$$\frac{\partial \tau_{j,j}^{(k)}}{\partial \mathbf{p}_j} = \frac{1}{c} \left(\mathbf{e}(\phi_{j,j}^{(k)}) - \mathbf{e}(\phi_{j,j}^{(k)} \pm \pi) \right) = \frac{2}{c} \mathbf{e}(\phi_{j,j}^{(k)})$$

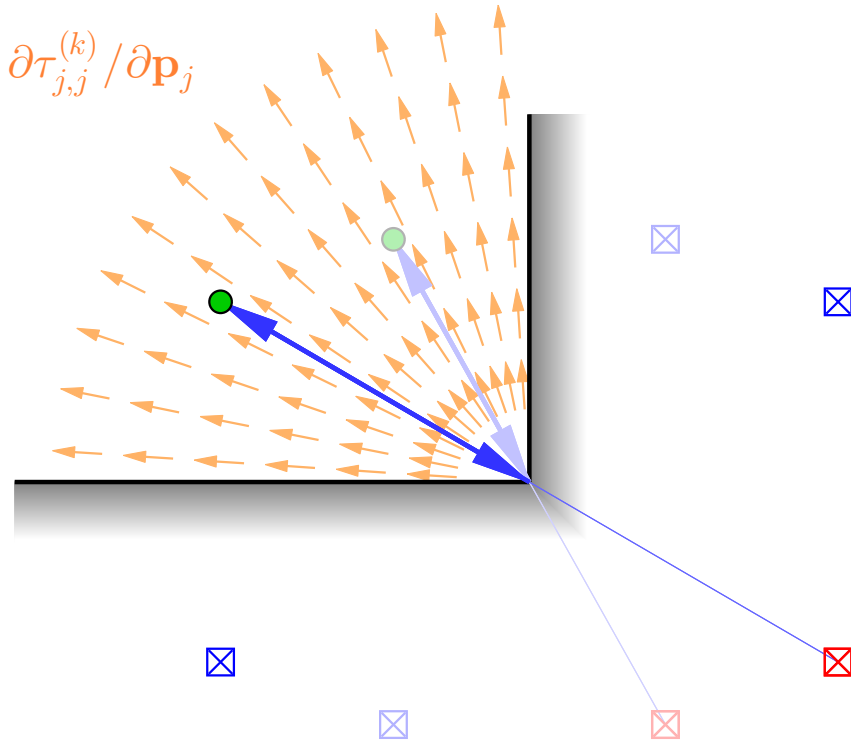


Figure 4.2: A monostatic second-order reflection on a wall corner is shown for two agent positions \mathbf{p}_j . Red squares are the respective VAs, blue squares are the intermediate (ambiguous) construction anchors. The orange, radial gradient field shows the direction of provided RI.

Figure 4.2 shows that direction $\mathbf{e}(\phi_{j,j}^{(k)})$ from the VA to the agent is equal to a direction vector pointing from the corner to the agent. Second-order corner VAs provide position information exclusively in said direction. The radial gradient fields in Figure 4.2 illustrates this property.

Third-Order VA between Two Walls

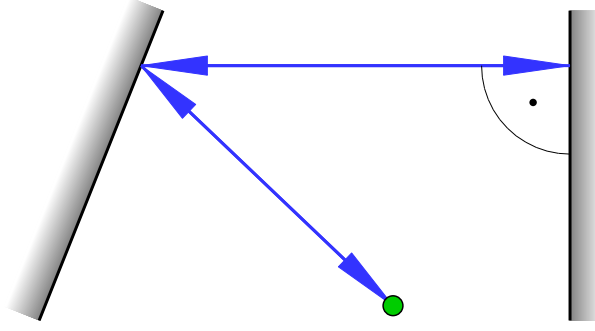


Figure 4.3: Shows a monostatic third-order reflection between two walls. The ray necessarily bounces off the second wall perpendicularly which causes arrival and departure angles to be equal at the agent.

Figure 4.3 shows the scenario. The ray departs and arrives from the same direction and is always perpendicular to the $q = 2$ wall. Section 4.2.4 explains why this is the only class of third-order VAs spared from severe problems during parameter estimation.

In the case of parallel walls, $\gamma_{j,j}^{(k)} = \gamma_{j,j}^{(k,1)} = \phi_{j,j}^{(k)} \pm \frac{\pi}{2}$ holds and the delay gradient is equal to gradient (4.18) of a first-order reflection off the wall that is involved twice (via $q = 1$ and $q = 3$).

4.2.2 Useless Virtual Anchors

Second Order VA of parallel Walls

The scenario is shown in Figure 4.4. Owing to the parallelism, wall angles $\gamma_{j,j}^{(k,2)} = \gamma_{j,j}^{(k,1)}$ are equal and the effective wall angle $\gamma_{j,j}^{(k)} = \gamma_{j,j}^{(k,2)} - \gamma_{j,j}^{(k,1)} = 0$ vanishes. Using (4.14)

$$\frac{\partial \tau_{j,j}^{(k)}}{\partial \mathbf{p}_j} = \frac{2}{c} \underbrace{\sin(0)}_{=0} \cdot \mathbf{e} \left(\pi + \phi_{j,j}^{(k)} - \frac{\pi}{2} \right) = \mathbf{0}$$

shows that the spatial delay gradient is zero over the entire room. Delays are fundamental quantities in localization though and we cannot utilize measurements with zero sensitivity towards them. Thus, second order VAs between parallel walls do not provide any position information and are entirely worthless for localization.²⁰

²⁰ They could be fruitful in a different application though: When an agent explores an unknown indoor environment, he could move around the room and then extract from the measured signals the MPCs whose propagation delays were constant while moving. Those delays could then serve in the estimation of the room size.

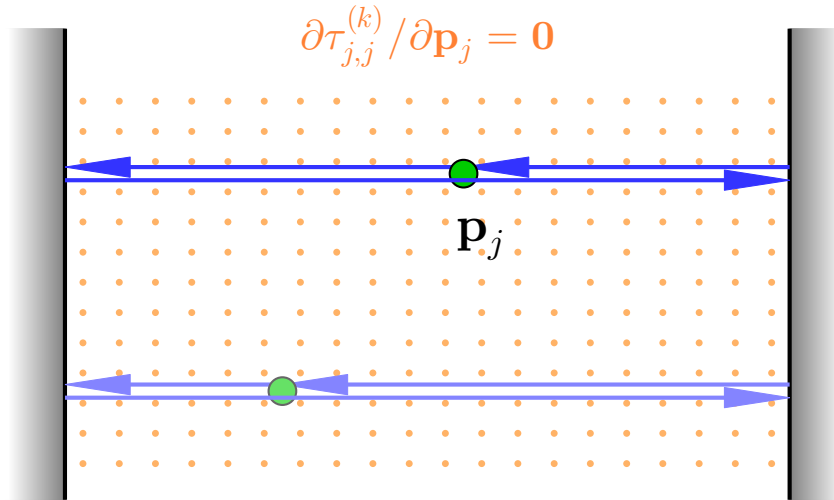


Figure 4.4: A monostatic second-order reflection between parallel walls. No matter where the agent is located, the ray always travels twice the distance between the walls, hence the propagation delay $\tau_{j,j}^{(k)}$ is constant. The orange dots indicate a nullified gradient field, corresponding to zero RI contribution of this type of VAs.

Other even-order VAs with vanishing Gradient

The statements about second-order VAs can be generalized to all even-order VAs: The spatial delay gradient associated with an even-order MPC ...

- ... vanishes iff $\gamma_{j,j}^{(k)} = l\pi$, $l \in \mathbb{Z}$.
- ... has maximum magnitude iff $\gamma_{j,j}^{(k)} = \frac{\pi}{2} + l\pi$, $l \in \mathbb{Z}$.
- ... is very hard to evaluate for all in-between cases because of the RI direction depending on both AoA and effective angle.

A fourth-order cyclic reflection in a rectangular room is shown in Figure 4.5. The effective angle of said MPC is

$$\gamma_{j,j}^{(k)} = \gamma_{j,j}^{(k,4)} - \gamma_{j,j}^{(k,3)} + \gamma_{j,j}^{(k,2)} - \gamma_{j,j}^{(k,1)} = 0 - \frac{\pi}{2} + 0 - \frac{\pi}{2} = \pi$$

and therefore the delay gradient is zero, i.e. the delay is constant. For either agent position, the propagation distance is

$$c \cdot \tau_{j,j}^{(k)} = 2 \cdot \sqrt{\text{room width}^2 + \text{room height}^2} = 2 \cdot \text{room diagonal}$$

which can be observed in Figure 4.5 with some geometric thought.

A more general statement is: For all quadrilateral room shapes where the symmetry $\gamma_{j,j}^{(k,q)} = -\gamma_{j,j}^{(k,q+2)}$ holds for all eligible q , all $4n$ -th order cyclic reflections have constant propagation delay. In Figure 4.6, we changed the rectangular room from Figure 4.5 in a sense that the wall angles deviate 5° horizontally and 10° vertically. Although the introduced skewness annihilates all geometric intuition, the formulas still prevail and in the same easy fashion show that the MPC delay is constant over the room. The only relevant criterion is a vanishing effective angle because of given symmetry.

The discussed fourth-order MPCs are nice examples but are practically irrelevant because after quadruple reflection the transmitted pulse will be attenuated to an extent where it will hardly be distinguishable from noise [9].

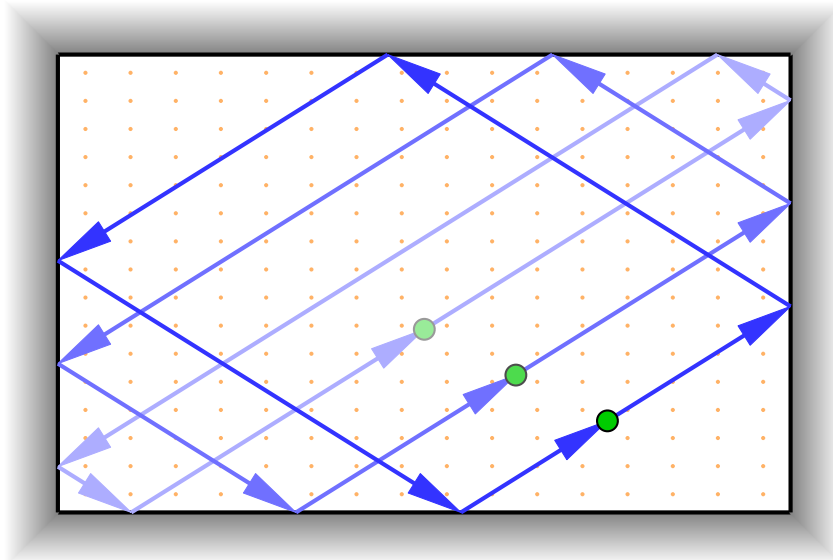


Figure 4.5: Monostatic cyclic fourth-order reflection in a rectangular room. No matter where the agent is positioned, the propagation distance is inherently equal to twice the room diagonal.

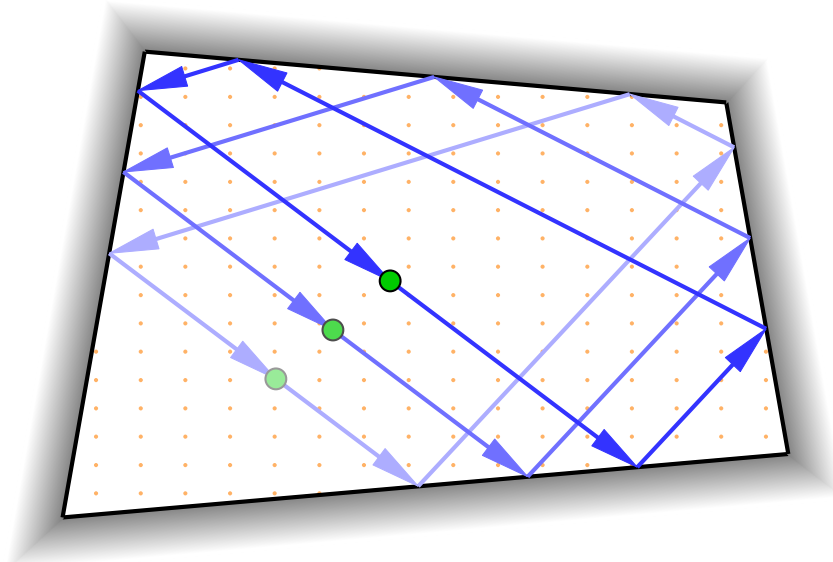


Figure 4.6: Monostatic cyclic fourth-order reflection in a quadrilateral room with antiparallel walls. Again, the propagation delay is invariant against agent positioning, which can easily be shown with the developed formulae despite the deviant geometry.

Figure 4.7 shows another fancy but purely theoretical example of a honeycomb-shaped room where the propagation delay of a sixth-order MPC is invariant against agent movements. Again, the effective angle $\gamma_{j,j}^{(k)} = 0$ because of the symmetry $\gamma_{j,j}^{(k,q)} = -\gamma_{j,j}^{(k,q+2)}$ and here even $\gamma_{j,j}^{(k,q)} = \gamma_{j,j}^{(k,q+3)}$.

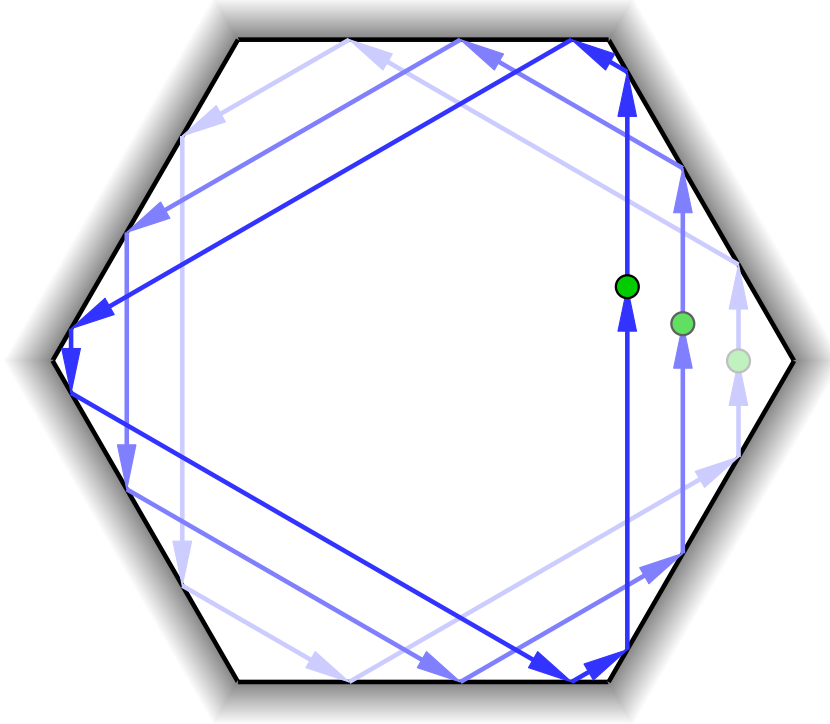


Figure 4.7: Monostatic cyclic sixth-order reflection in a honeycomb-shaped room. The room geometry has even two symmetry properties that qualify for a vanishing effective wall angle and in turn a constant propagation delay.

4.2.3 Miscellaneous Virtual Anchors

Third Order Side-End-Side VA

We assume parallel side walls with angle $\gamma_s := \gamma_{j,j}^{(k,1)} = \gamma_{j,j}^{(k,3)}$ and a perpendicular end wall, i.e. $\gamma_e := \gamma_{j,j}^{(k,2)} = \gamma_s \mp \frac{\pi}{2}$.

$$\gamma_{j,j}^{(k)} = \gamma_{j,j}^{(k,3)} - \gamma_{j,j}^{(k,2)} + \gamma_{j,j}^{(k,1)} = 2\gamma_s - \gamma_e = \gamma_s \pm \frac{\pi}{2}$$

$$\begin{aligned} \frac{\partial \tau_{j,j}^{(k)}}{\partial \mathbf{p}_j} &= \frac{2}{c} \sin(\gamma_{j,j}^{(k)} - \phi_{j,j}^{(k)}) \mathbf{e}(\gamma_{j,j}^{(k)} - \frac{\pi}{2}) = \frac{2}{c} \sin(\gamma_s - \phi_{j,j}^{(k)} \pm \frac{\pi}{2}) \mathbf{e}(\gamma_s \pm \frac{\pi}{2} - \frac{\pi}{2}) \\ &= \frac{2}{c} (\pm 1) \cos(\gamma_s - \phi_{j,j}^{(k)}) (\pm 1) \mathbf{e}(\gamma_s) = \frac{2}{c} \cos(\gamma_s - \phi_{j,j}^{(k)}) \mathbf{e}(\gamma_s) \end{aligned} \quad (4.19)$$

Hence, a third order side-end-side VA provides position information along the main direction $\mathbf{e}(\gamma_s)$.

Figure 4.8 shows such a VA by means of a long corridor. For very long corridors, ray and side wall are approximately parallel and thus $\phi_{j,j}^{(k)} \approx \gamma_s \pm \frac{\pi}{2}$ depending on the orientation of the end wall. The magnitude in (4.19) is then maximum because $\cos(\gamma_s - \phi_{j,j}^{(k)}) \approx \cos(0 \pm \frac{\pi}{2}) = \pm 1$ and

$$\frac{\partial \tau_{j,j}^{(k)}}{\partial \mathbf{p}_j} \approx \pm \frac{2}{c} \mathbf{e}(\gamma_s) .$$

The delay gradient is approximately equal to the case of a first-order reflection off the far end

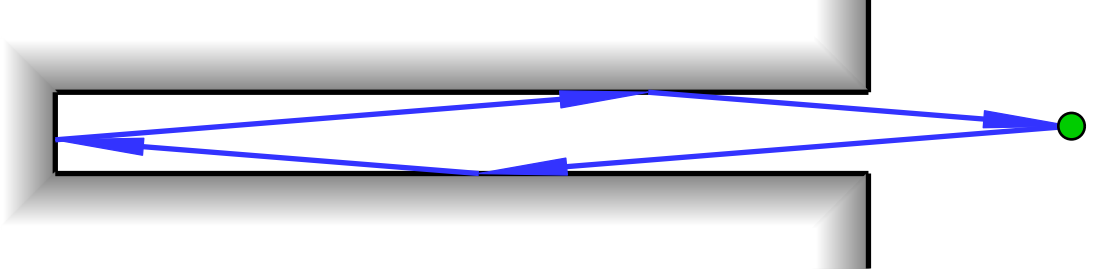


Figure 4.8: Monostatic third-order side-end-side reflection. This MPC provides RI along the main direction of the corridor. The gradient (and therefore RI) magnitude is maximum for a very long corridor where the AoA approaches $\phi_{j,j}^{(k)} \rightarrow \gamma_s$, i.e. becomes parallel to the main direction.

wall, cf. (4.18).

Third Order End-Side-Side VA of a crooked Corridor

Figure (4.9) shows the setup. The $q = 2$ and $q = 3$ walls are parallel, i.e. $\gamma_{j,j}^{(k,3)} = \gamma_{j,j}^{(k,2)}$, so these angles cancel out in the effective angle formula (3.26) and we get $\gamma_{j,j}^{(k)} = \gamma_{j,j}^{(k,1)}$. The spatial delay gradient is then

$$\frac{\partial \tau_{j,j}^{(k)}}{\partial \mathbf{p}_j} = \frac{2}{c} \sin(\gamma_{j,j}^{(k,1)} - \phi_{j,j}^{(k)}) \mathbf{e}(\gamma_{j,j}^{(k,1)} - \frac{\pi}{2}).$$

Thus, the RI is directed perpendicular to the $q = 1$ wall. In the shown scenario, this amounts to purely horizontal position information. The contribution is attenuated by a factor $0 < \sin(\gamma_{j,j}^{(k,1)} - \phi_{j,j}^{(k)}) < 1$. A more particular expression thereof, e.g. by expressing $\phi_{j,j}^{(k)}$ as a function of \mathbf{p}_j and wall angles $\gamma_{j,j}^{(k,q)}$ would, be extremely involved though.

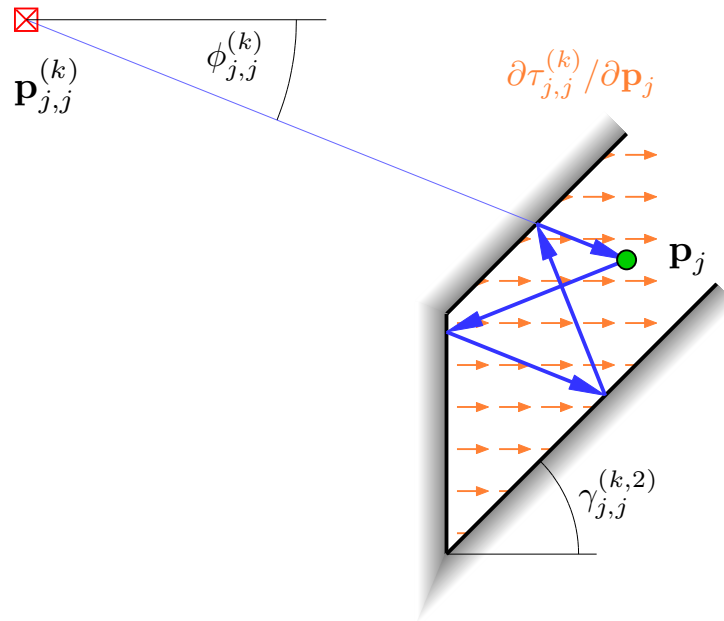


Figure 4.9: A monostatic third-order reflection where the second and third involved walls are parallel. The VA provides RI directed orthogonal to the first wall.

Third Order Reflection around an Obstacle

Figure 4.10 shows an example where a monostatic high-order reflection is essential for obtaining RI in a certain direction. All other eligible reflection paths are obstructed.

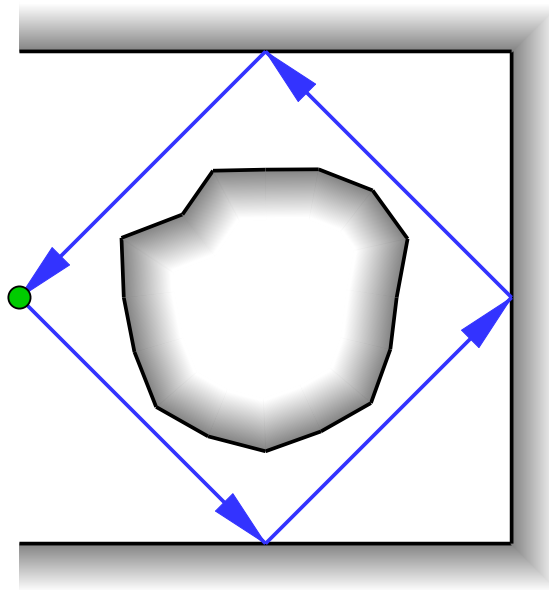


Figure 4.10: An obstacle is present in the room but unregistered in the floorplan. The third-order reflection around the obstacle is the only reasonable means of obtaining horizontal position information for the agent. The first-order reflection path on the right-side wall and the corner reflections are obstructed.

4.2.4 Inherent Path-Overlap Problem

Figure 4.11 illustrates a problem that, without special handling, renders most higher-order MPCs useless or at least problematic for monostatic localization: A given MPC has a particular AoA. Now you can always launch a ray in direction of the aforementioned AoA and the ray will travel exactly the reverse path. The two paths thus will have exactly the same propagation delay and will inherently and always result in exact path overlap.

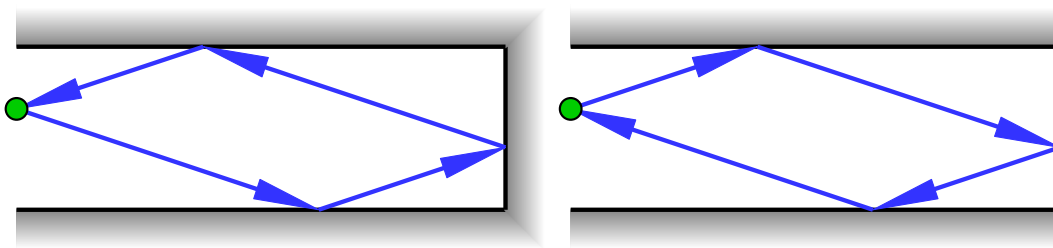


Figure 4.11: Opposite directions of otherwise equal reflection paths. The propagation delay is equal, which inherently causes maximum path overlap.

Equality of delays $\tau_{j,j}^{(k)} = \tau_{j,j}^{(k')}$ of opposite paths causes an illposed estimation problem. The CRLB (4.11) will not be evaluable because of a singular matrix $\Phi_{j,j}(\alpha_{j,j}, \alpha_{j,j})$, which informally means infinite impairment through path overlap.

An MPC is spared from this problem if and only if AoA and angle of departure are equal. This includes first-order reflections, second-order corner reflections and third-order reflections

between two walls.

A means to avoid this problem is discarding all problematic pairs of MPCs from the estimation model. One could argue that this is the best solution, because most problematic MPCs are either inherently worthless for localization (e.g., second-order parallel wall reflection) or have poor signal-to-noise ratio (SNR) due to a high number of reflections on their path. On the other hand, there are very well problematic MPCs with a non-negligible contribution, Figure 4.10 shows an extreme case.

A more sensitive approach would be discarding one VA of each problematic pair from the model, but the practicability thereof is left as an open question. Yet another not fully developed approach is shown in Figure 4.12, where the same pair of third-order side-end-side corridor MPCs as before fully overlaps. We learned in (4.19) that such VAs provide localization information perpendicular to the end wall (here: horizontal). We substitute the pair of third-order VAs with a single first-order VA with equal distance and position information and that way obtained an equivalent description.

All mentioned approaches pose a hard challenge to implementations when we expect them to robustly detect and handle pairs of opposite multipaths.

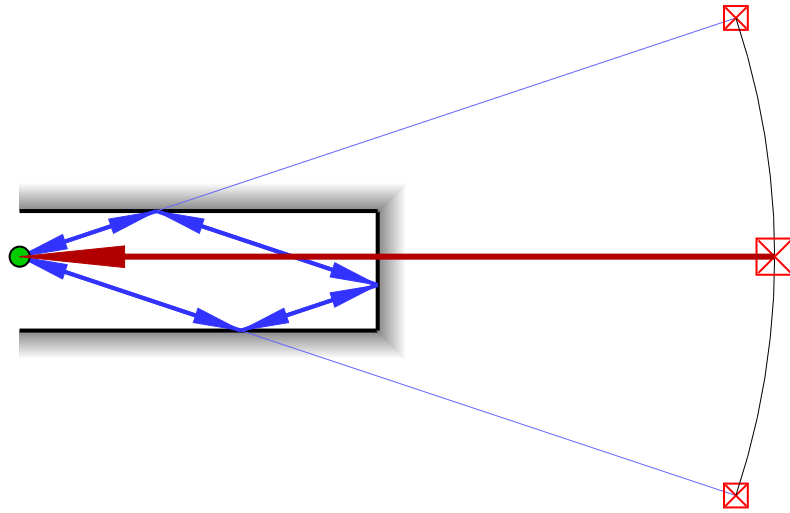


Figure 4.12: A pair of VAs of opposite and thus inherently overlapping multipaths is getting substituted by a first-order VA. This alternative description has equivalent distance and localization contribution.

4.3 Monostatic Numerical Results

4.3.1 Matlab Approach

Using Matlab, we compute the PEB given by EFIM (4.11) over an exemplary room in the fashion of [6, 16]. The setup with a single mobile agent at \mathbf{p}_j in an indoor environment is shown in Figure 4.13.

For each position, we compute the set of monostatic VAs and their visibilities, which forms a basis for the computation of all MPC parameters: Delays $\tau_{j,j}^{(k)}$ are a result of the distance between agent and VAs, see (3.1). The amplitudes $\alpha_{j,j}^{(k)}$ are computed using a free-space pathloss model [29], assuming a carrier frequency of $f_c = 7$ GHz and adding 3 dB of attenuation for each reflection at a wall. We neglect second-order VAs between parallel walls and other useless or

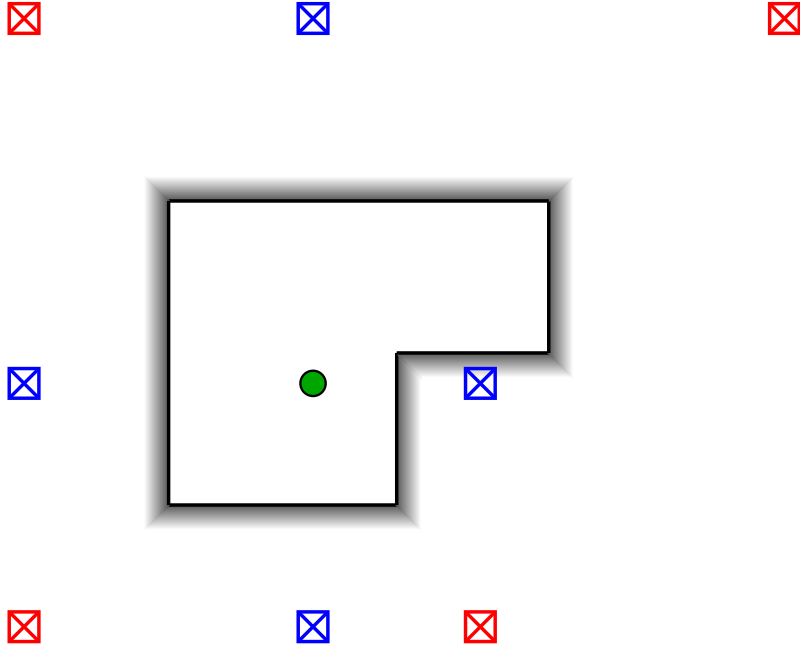


Figure 4.13: Mobile agent at \mathbf{p}_j in a simple indoor environment. For the current position, all first-order VAs are shown in blue and second-order corner VAs are shown in red. Invisible, infeasible, or useless VAs were discarded.

problematic VAs for reasons explained in Section 4.2.2 and 4.2.4.

We use an ultra-wideband (UWB) raised cosine pulse [29] $s(t)$ with pulse duration $T_s = 1$ ns and roll-off factor $\beta = 0.6$. We assume the same propagation channel model as the Matlab code of Witrisal et al. that generated the numerical results of [6]. Thus, we use the delay power spectrum [6, 28] of DMP, given by [5] as

$$S_\nu(\tau) = \Omega_1 \frac{\gamma_1 + \gamma_{\text{rise}}}{\gamma_1(\gamma_1 + \gamma_{\text{rise}}(1 - \chi))} \left(1 - \chi \cdot e^{-\tau/\gamma_{\text{rise}}}\right) e^{-\tau/\gamma_1} . \quad (4.20)$$

We choose shape parameters $\gamma_{\text{rise}} = 5$ ns, $\gamma_1 = 20$ ns, $\chi = 0.98$ and normalized power $\Omega_1 = \frac{1}{10} \cdot \left(\frac{c}{4\pi f_c}\right)^2$. The power spectral density (PSD) of AWGN is set to $N_0 = 10^{-8} \frac{1}{\text{Hz}}$. Figure 4.14 shows the received signal composed of MPCs and DMP for the setup in Figure 4.13.

VA positions are obtained by (consecutive) wall mirroring, cf. Chapter 3. Answering the visibility question requires execution of the ray tracing operation outlined in Section 3.1. In the course, we check for any obstruction by uninvolved walls and verify the feasibility of the ray, which is computationally expensive.

There already exist an optical ray-tracking tool (MATLAB) for bistatic situated RX and TX, which was adapted to the monostatic setup. The PEB of the monostatic setup was evaluated for 640000 position \mathbf{p}_j over a grid with 1 cm spacing.

4.3.2 Results neglecting Path Overlap

Figure 4.15, 4.16, and 4.17 show the monostatic PEB for VAs up to the first, second, and third order respectively. The results neglect the adverse effect of path overlap. Positioning works well when balanced horizontal and vertical RI is available, i.e. when the agent is close to a corner. Otherwise free-space pathloss over reflection paths decreases the SNR of MPC and impairs performance. Adding second-order VAs yields a significant performance boost, but furthermore going up to the third order barely changes anything. This is also evident in the cumulative distribution function of the PEB in Figure 4.25, where distributions of orders 2 and

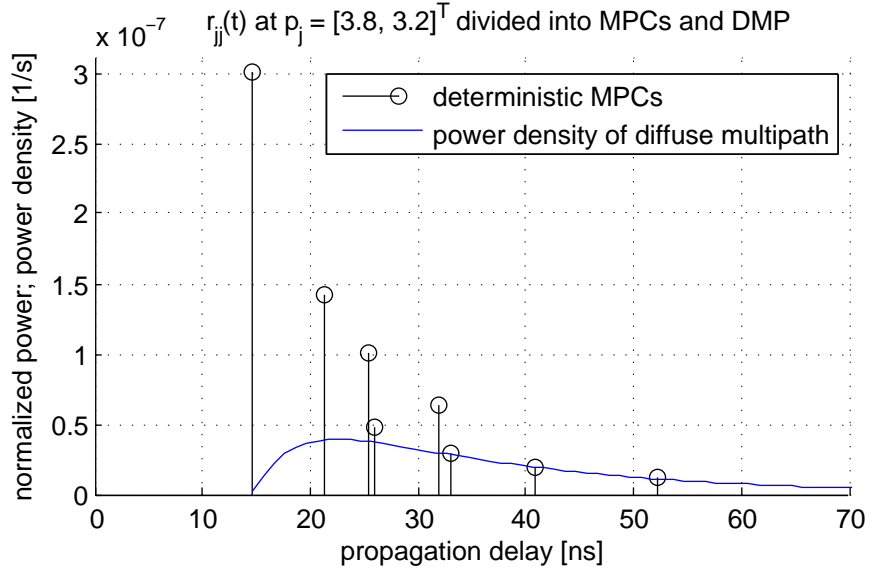


Figure 4.14: Power of MPCs and DMP in a received signal $r_{j,j}(t)$ for the monostatic setup given in Figure 4.13. DMP attunes after the earliest MPC.

3 are almost identical. A result of Shen and Win [31] explains this PEB convergence: Any MPC $\alpha_{j,j}^{(k)} \cdot s(t - \tau_{j,j}^{(k)})$ beyond the fifth ($k > 5$) is completely irrelevant to localization performance as long as MPCs $1 \leq k \leq 5$ have decent SINR and some directional diversity. In fact components $k > 3$ barely contribute anything. Furthermore, third-order VAs are especially irrelevant within our chosen parameters because of their low SNR due to -9 dB reflection damping. The bottom line is that in the absence of path overlap, adding higher-order VAs strictly improves performance but the gain beyond second order is neglectable.

Figure 4.18 and 4.19 show the relative performance gain when adding higher-order VAs. The biggest gains occurs in areas distant from the corner diagonals. In said diagonals, the performance is excellent for order 1 already, so there is not much room for improvement.

Figure 4.20 and 4.21 show error ellipses at many positions for VA orders up to first and third respectively. The half-axis diameters correspond to the minimum and maximum directional position error bound (DPEB) which is explained in detail in [2]. We define the monostatic DPEB in direction of a unit vector \mathbf{e} as

$$\text{DPEB}(\mathbf{p}_j; \mathbf{e}) = \sqrt{\mathbf{e}^T \cdot [\mathbf{J}_{\boldsymbol{\theta}}^{-1}]_{2 \times 2} \cdot \mathbf{e}} = \sqrt{\mathbf{e}^T \cdot \mathbf{J}_{\mathbf{p}_j}^{-1} \cdot \mathbf{e}}.$$

All ellipses are aligned with the main coordinate axes, which is due to first-order VAs of vertical and horizontal walls providing horizontal and vertical RI respectively. When going from order 1 to 3, ellipses visibly shrink. This amounts to the performance gain described earlier.

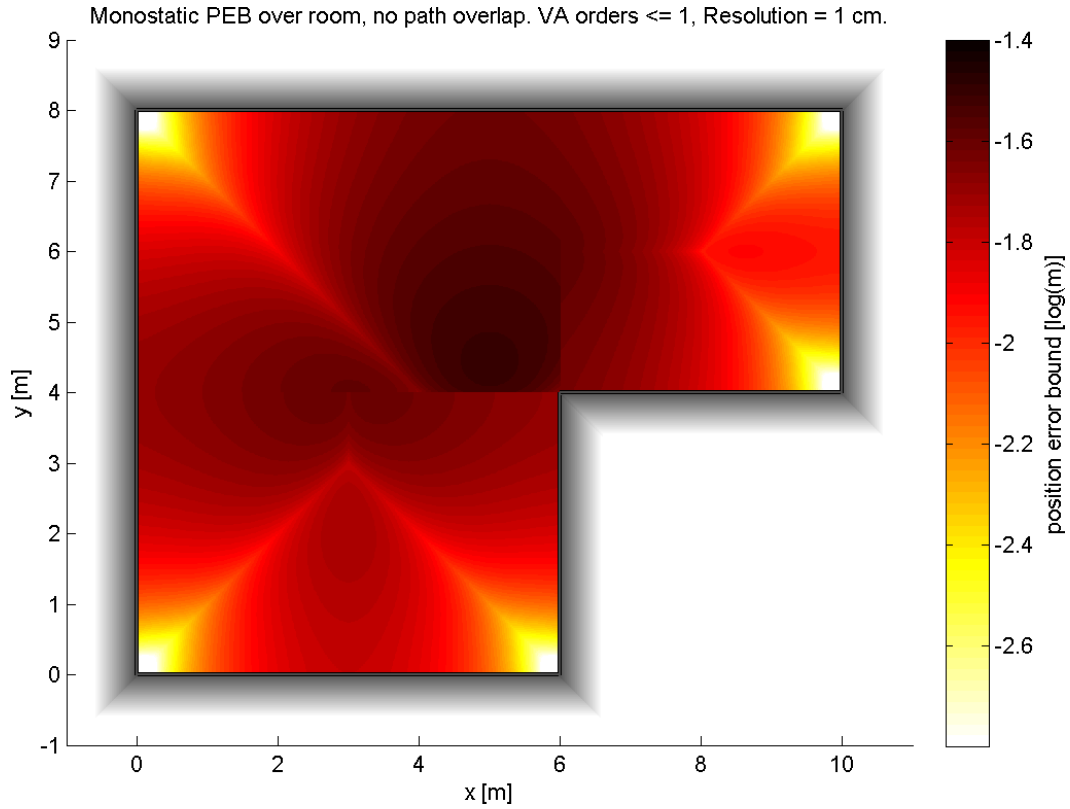


Figure 4.15: PEB of monostatic indoor localization neglecting path overlap over a simple room. VAs of order up to 1 enable multipath-assisted localization.

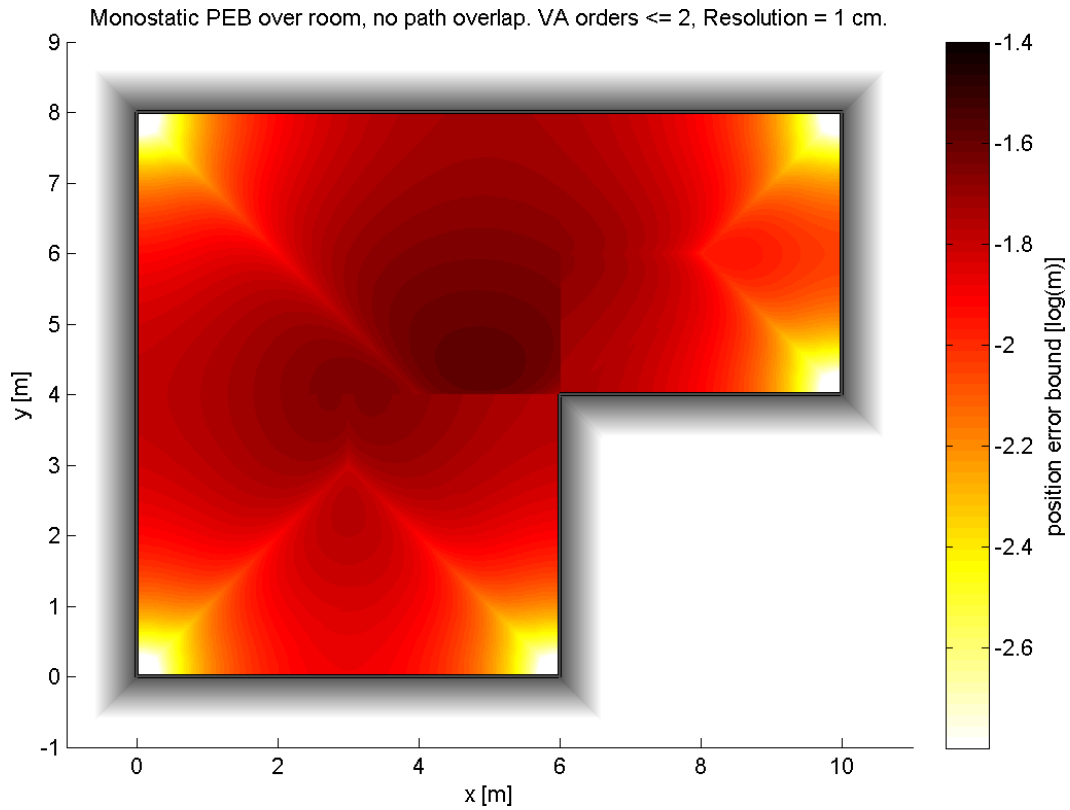


Figure 4.16: PEB of monostatic indoor localization neglecting path overlap over a simple room. VAs of order up to 2 enable multipath-assisted localization.

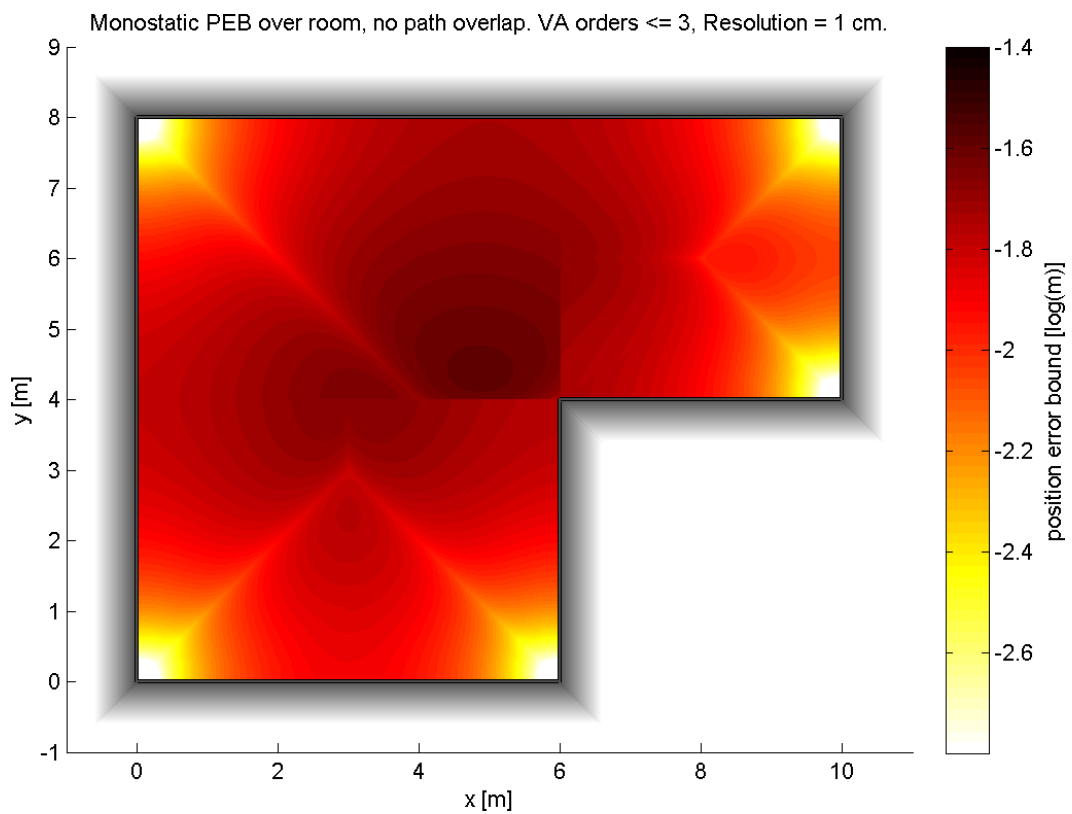


Figure 4.17: PEB of monostatic indoor localization neglecting path overlap over a simple room. VAs of order up to 3 enable multipath-assisted localization.

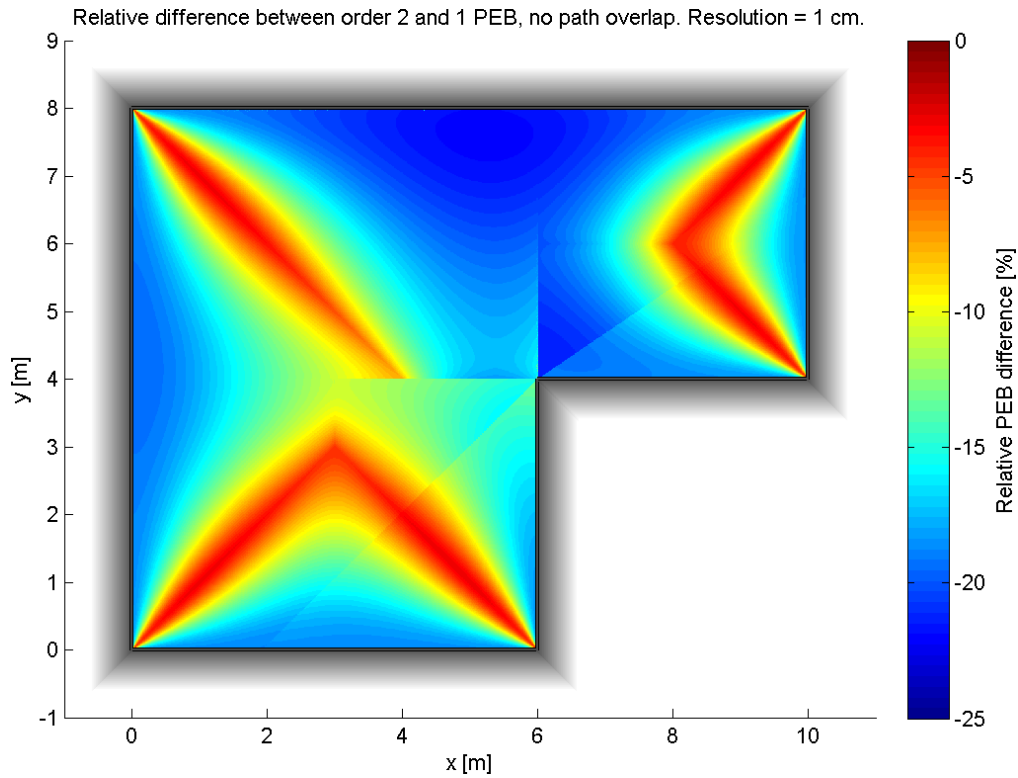


Figure 4.18: Relative PEB decline when adding second-order VAs to a monostatic indoor localization model. Path overlap is neglected.

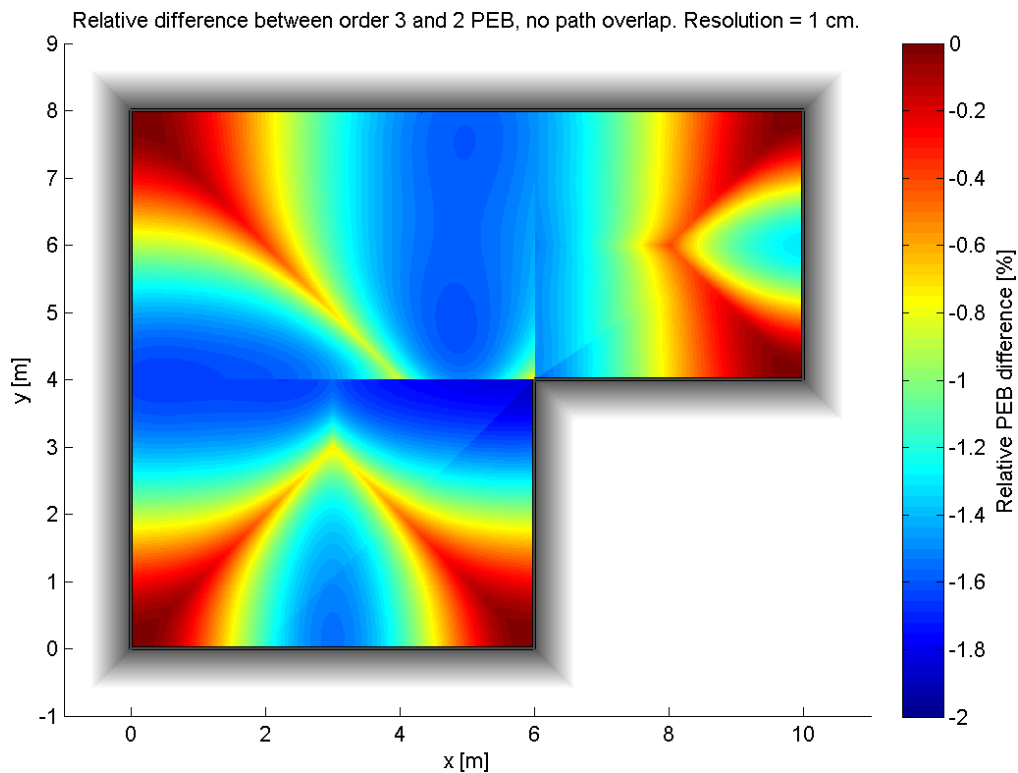


Figure 4.19: Relative PEB decline when adding third-order VAs to a monostatic indoor localization model. Path overlap is neglected. Take note that the scale is vastly smaller than in Figure 4.18.

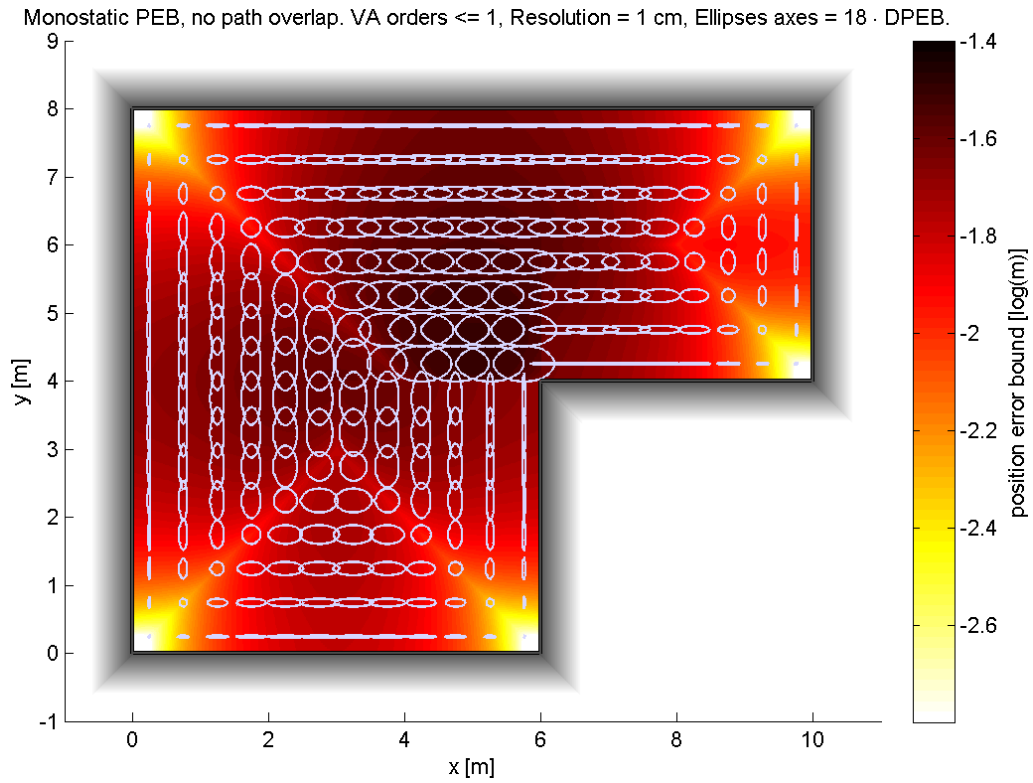


Figure 4.20: Error ellipses show the directivity of the PEB during first-order monostatic localization. Path overlap is neglected. Half-axes were enlarged by a factor of 18 for illustration purposes.

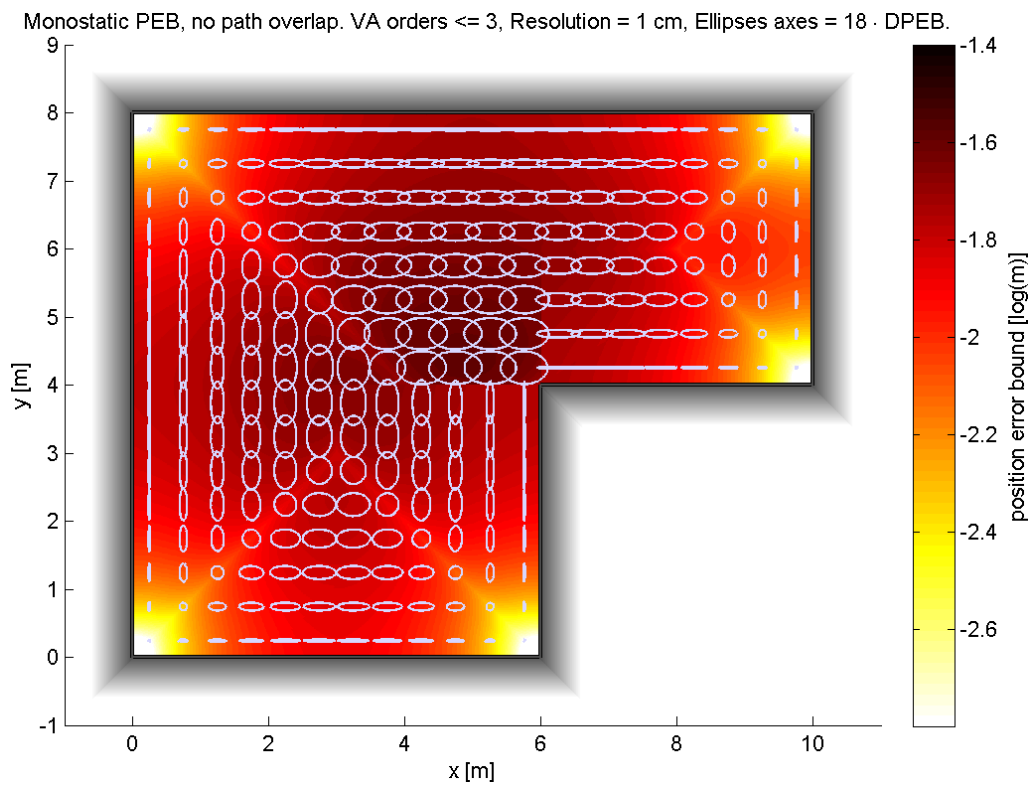


Figure 4.21: Error ellipses show the directivity of the PEB during third-order monostatic localization. Path overlap is neglected. Half-axes were enlarged by a factor of 18 for illustration purposes.

4.3.3 Results considering Path Overlap

Figure 4.22, 4.23, and 4.24 show the monostatic PEB over our exemplary room when considering path overlap for VAs up to order 1, 2, 3 respectively.

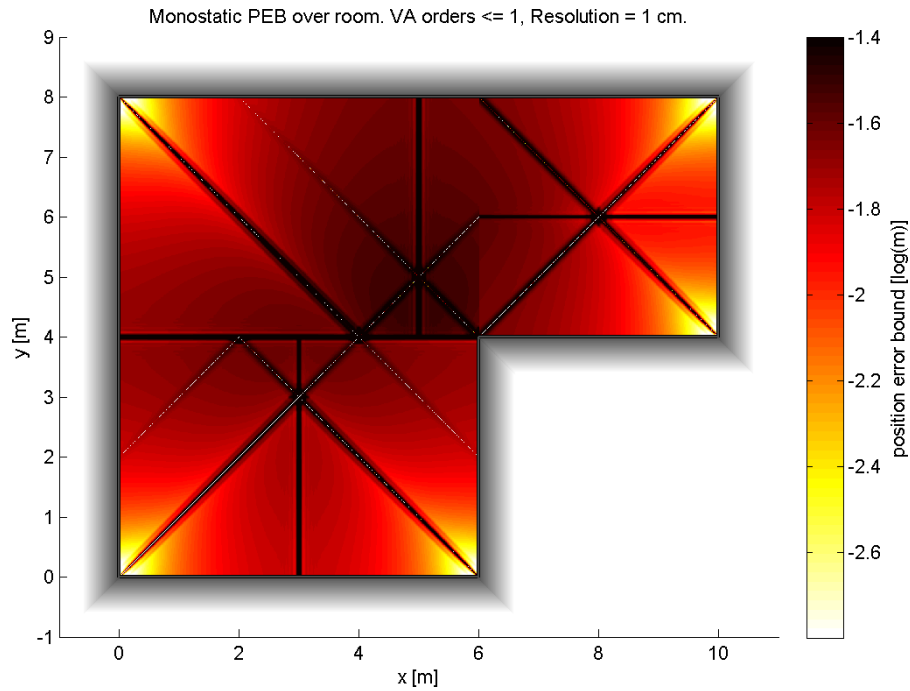


Figure 4.22: PEB of monostatic localization considering path overlap. First-order VAs are being used.

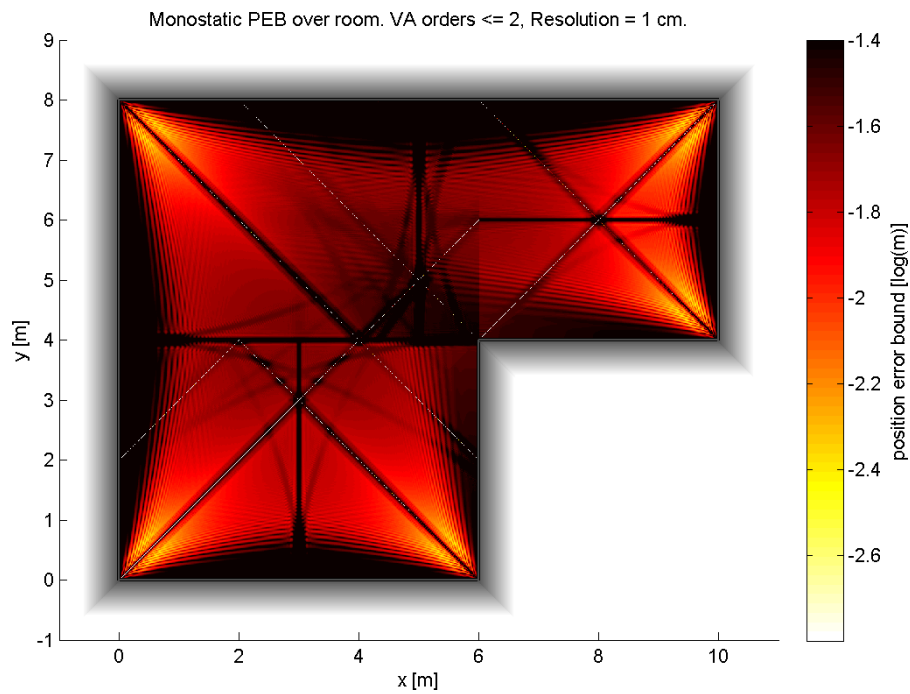


Figure 4.23: PEB of monostatic localization considering path overlap. VAs of order ≤ 2 are being used.

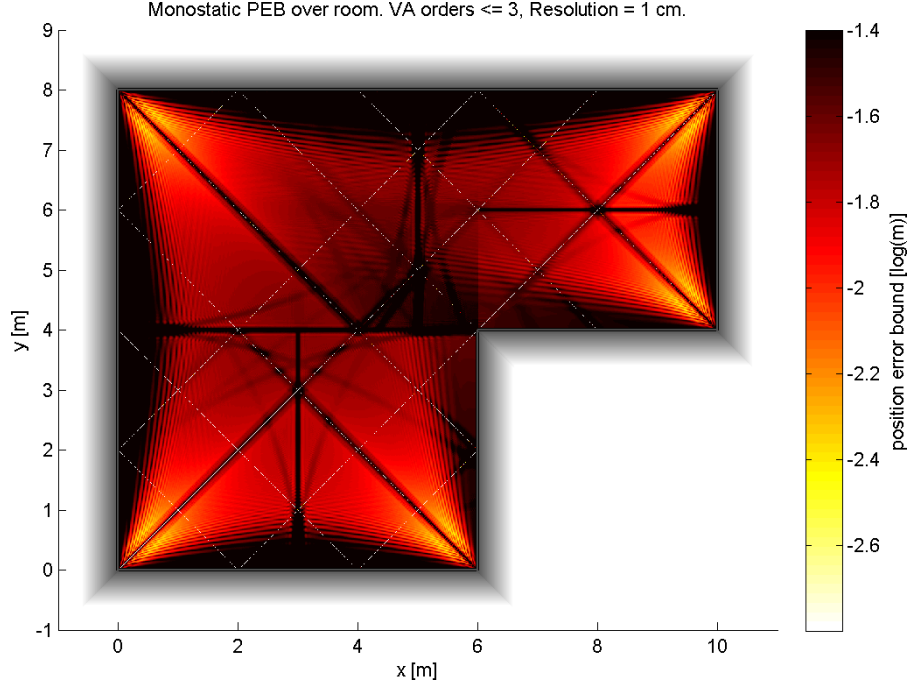


Figure 4.24: PEB of monostatic localization considering path overlap. VAs of order ≤ 3 are being used.

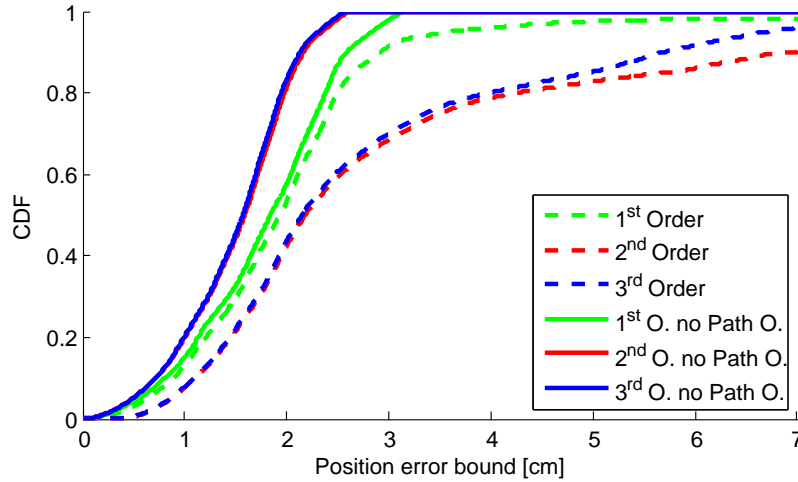


Figure 4.25: Cumulative distribution functions of the PEB for different monostatic localization assumptions.

The localization performance is on a large-scale similar to earlier results, although outage regions or at least regions of poor performance arise in areas of overlapping pulses. Pulses of single wall reflections overlap on the major symmetry axes of the room, best seen in Figure 4.22 and the 3D plot in Figure 4.27. The manifolds of path overlap from the addition of higher-order VAs are trickier though.

In Figure 4.23 and 4.24, we see a massive PEB increase close to walls. This is due to overlapping pulses from a second-order corner reflection and a first-order reflection on one of the corner walls. Let us calculate such a case: $\mathbf{p} = (x, y)^T$ is the agent position. $\mathbf{p}_{j,j}^{(k_c)} = (-x, -y)^T$ is the second-order VA about the lower-left corner at $(0, 0)^T$. $\mathbf{p}_{j,j}^{(k_f)} = (x, -y)^T$ is the first-order VA about the lower wall. The distances between VAs and the agent are $\|\mathbf{p}_{j,j}^{(k_f)} - \mathbf{p}\| = 2 \cdot y$ and $\|\mathbf{p}_{j,j}^{(k_c)} - \mathbf{p}\| = 2 \cdot \sqrt{x^2 + y^2}$ respectively. No path overlap occurs when those distances are at

least the pulse width apart:

$$\begin{aligned}
\|\mathbf{p}_{j,j}^{(k_c)} - \mathbf{p}\| &\geq \|\mathbf{p}_{j,j}^{(k_f)} - \mathbf{p}\| + c \cdot T_s \\
\sqrt{x^2 + y^2} &\geq y + \frac{c \cdot T_s}{2} \\
x &\geq \sqrt{c \cdot T_s \cdot \left(\frac{c \cdot T_s}{4} + y\right)}
\end{aligned} \tag{4.21}$$

With $T_s = 1$ ns, we get $c \cdot T_s = 0.3$ m. Let us compute some values

$$\begin{aligned}
y = 0 &\implies x \geq \frac{c \cdot T_s}{2} = 0.15 \text{ m} \\
y = 3 &\implies x \geq \sqrt{0.3 \text{ m} \cdot (0.075 \text{ m} + 4 \text{ m})} \approx 0.96 \text{ m} .
\end{aligned} \tag{4.22}$$

The red lines in Figure 4.26 show all occurring parabolas of type (4.21) for our exemplary room. The pattern matches the numerical results in Figure 4.23 and 4.24. Statement (4.22) is in accordance with the plots too, $\mathbf{p} = (3 \text{ m}, 0.96 \text{ m})^T$ sits at the border between the path-overlap outage region to the left and the normal operation region to the right.

In Figure 4.23 and 4.24, the fine patterns close to the big outage regions are just as well a result of the glancing intersection between corner reflection and wall reflection and depend on the characteristics of the used pulse. The side lobes of the autocorrelation of the raised-cosine pulse are the reason for the observable pattern.

Figure 4.23 suggests that second-order corner VAs cause even more complex patterns due to path overlap. We have a look at manifolds where the distance between a corner VA and a first-order VA of a non-neighboring wall are equal. As an example, we use the lower left corner VA at $\mathbf{p}_{j,j}^{(k_c)} = (-x, -y)^T$ once more, but now paired with the upper wall single reflection $\mathbf{p}_{j,j}^{(k_f)} = (x, 8 + (8 - y))^T$.

$$\begin{aligned}
\|\mathbf{p}_{j,j}^{(k_c)} - \mathbf{p}\| &= \|\mathbf{p}_{j,j}^{(k_f)} - \mathbf{p}\| \\
\sqrt{(x - (-x))^2 + (y - (-y))^2} &= \sqrt{(x - x)^2 + (16 - y - y)^2} \\
\cancel{A} \cdot x^2 + \cancel{A} y^2 &= \cancel{A} \cdot 8^2 - \cancel{A} \cdot 16y + \cancel{A} y^2 \\
y &= 4 - \left(\frac{x}{4}\right)^2
\end{aligned} \tag{4.23}$$

This exemplary strong path-overlap is observable in Figure 4.23 and is best seen in Figure 4.28: The parabola starts on the left wall at $(0, 4)^T$ (in the near-wall outage region), extends to $(3, 3.44)^T$ and ends on the lower-middle wall at $(6, 1.75)^T$. Figure 4.26 shows all manifolds of that kind as green lines. There, equations like (4.23) were used to predict the curves on their respective intervals of given VA visibility. The predictions are in full accordance with the numerical results. The numerical results also show that the practical impact of these tricky patterns is minor compared to the problematic outage regions near walls.

The described outage regions along walls are responsible for unexpected effects: In contrary to the neglected path overlap results, addition of third-order VAs now has a significant contribution to localization. This is explained by the overlap of first- and second-order reflections, making them useless near walls. There, non-neighbouring VAs of that kind usually provide minor RI, so what's left are the third-order VAs which now provide important cues in these areas. This results in an unexpected outcome when ranking the three different assumptions with the cumulative distribution function in Figure 4.25: Considering first-order MPCs results in the best

performance explained by smaller outage regions. An interesting observation is that third-order MPCs partly compensate the effect of path overlap, induced by second-order MPCs, even though third-order MPCs introduce further path overlap. This leads to a (slightly) better performance. Second and third are almost identical for PEBs ≤ 4 cm, but beyond that third-order is clearly superior.

The bottom line is that the consideration of higher-order VAs, on the one hand, introduces severe problems in some regions because of additional path overlap, but on the other hand may improve performance in previous outage regions.

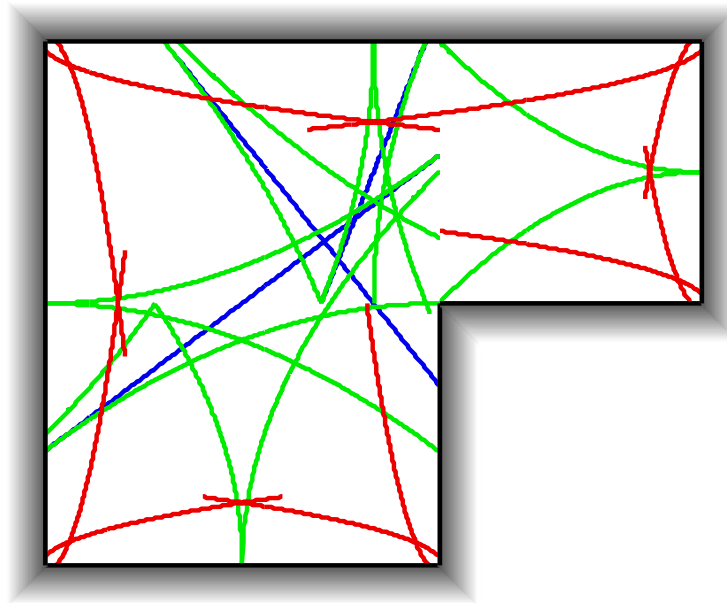


Figure 4.26: Predictions of all non-trivial path-overlap patterns during monostatic localization with VAs of order ≤ 2 . Red parabolas show boundaries of major outage regions close to walls because of a corner VA and a neighbouring first-order VA having similar delays there, cf. (4.21). Green parabolas show the center of path overlap grooves, they are owing to a corner VA and a non-neighboring first-order VA having equal delays, cf. (4.23). Blue lines show the non-trivial path overlap grooves stemming from two overlapping, non-neighboring corner VAs. The predictions accurately match the outcome in Figure 4.23 and the difference plot in Figure 4.28. We observe that central regions are especially prone to clusters of complex path-overlap patterns.

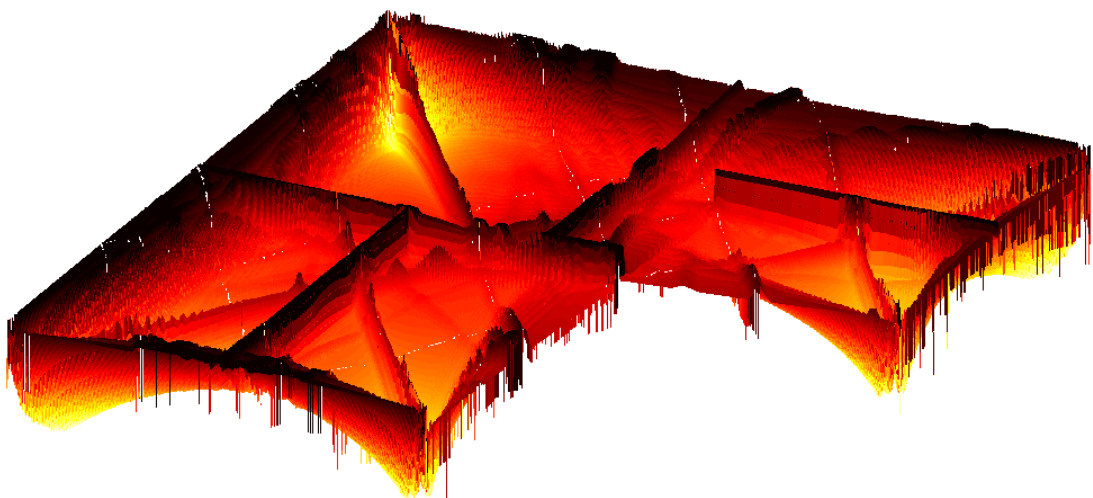


Figure 4.27: 3D plot of monostatic third-order PEB, cf. Figure 4.24.

Figures 4.28 and 4.29 show the relative change in PEB caused by the addition of second- and third-order VAs respectively and give visualizations of the introduced path-overlap patterns.

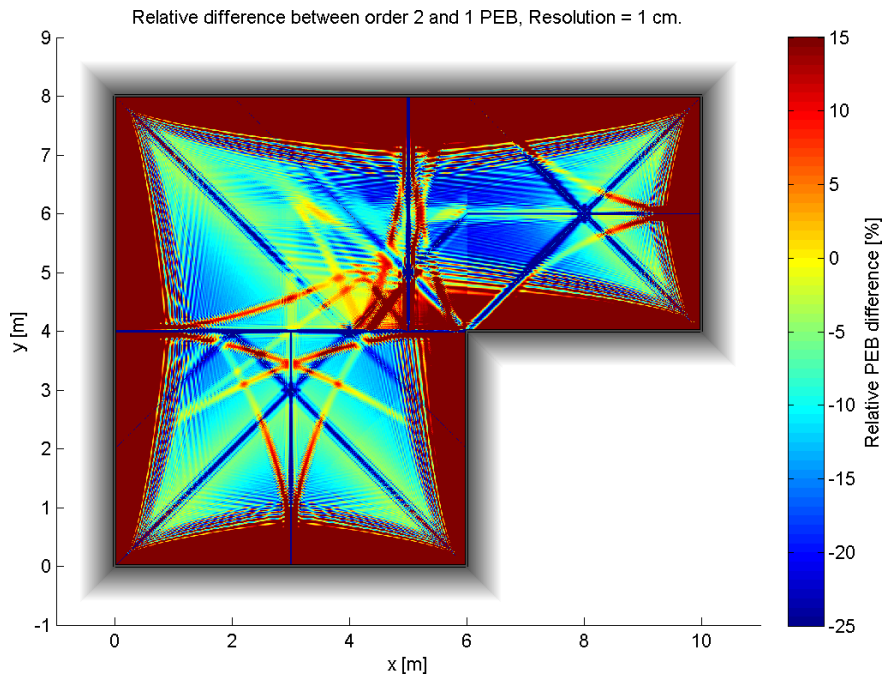


Figure 4.28: Relative PEB change when adding second-order VAs to a monostatic indoor localization model. Values close to walls go up to $\approx 500\%$ and are not properly considered by the color range. The path overlap patterns match the predictions in Figure 4.26.

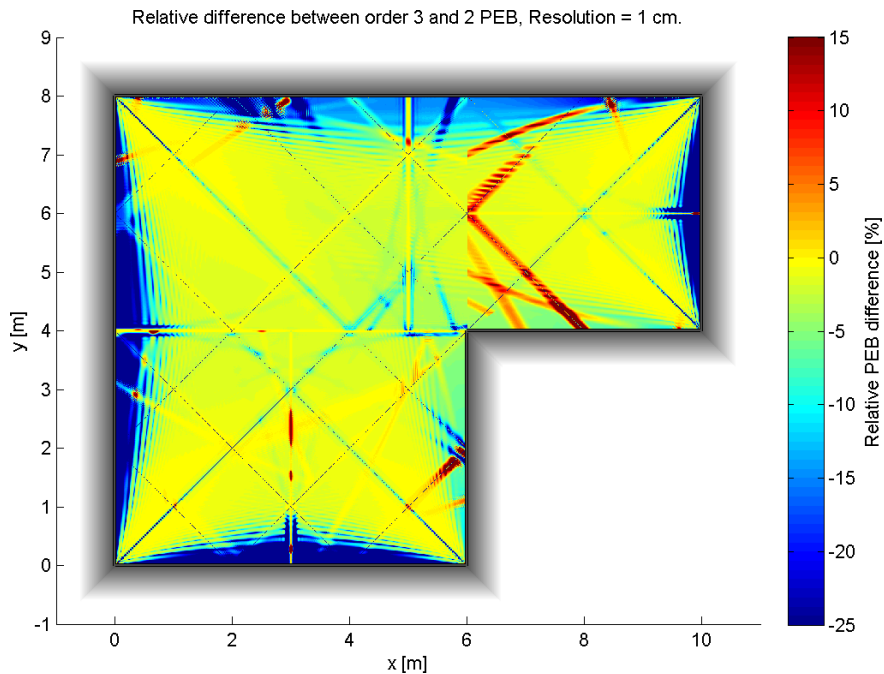


Figure 4.29: Relative PEB change when adding third-order VAs to a monostatic indoor localization model. Performance mostly improves, especially in the problematic wall-near regions. Merely some small strips suffer from performance impairment due to overlapping higher-order reflections.

Ellipses in Figure 4.30 and 4.31 illustrate directivity of the PEB. In comparison to the neglected path-overlap case in Figure 4.20 and 4.21, ellipses in central regions did not change significantly but got vastly deteriorated in positions where path overlap is an issue.

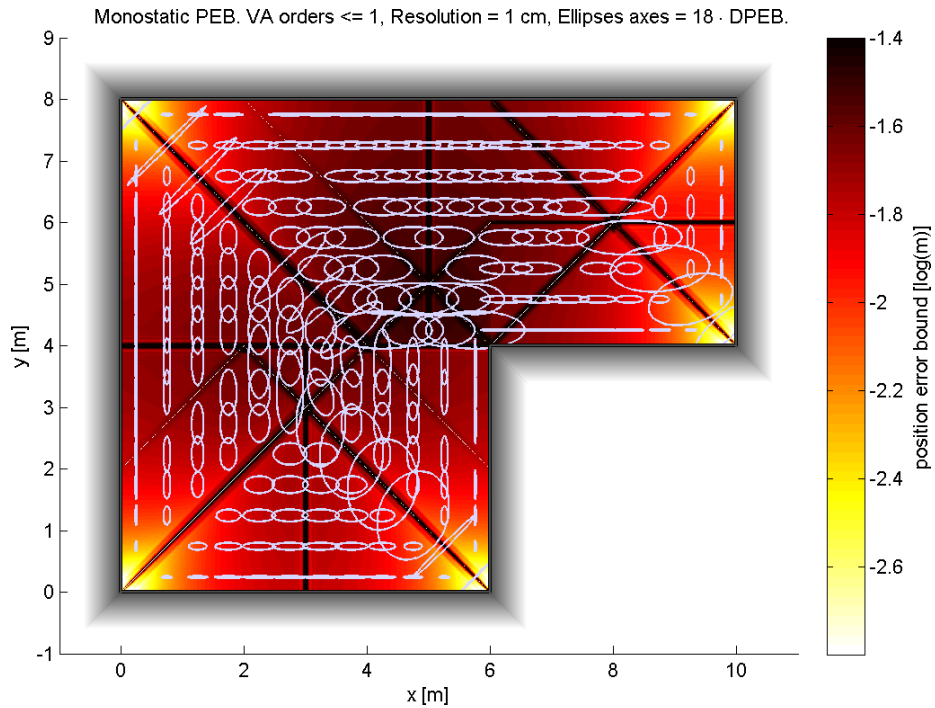


Figure 4.30: Error ellipses show the directivity of the PEB during first-order monostatic localization. Path overlap is considered. Half-axes were enlarged by a factor of 18 for illustration purposes.

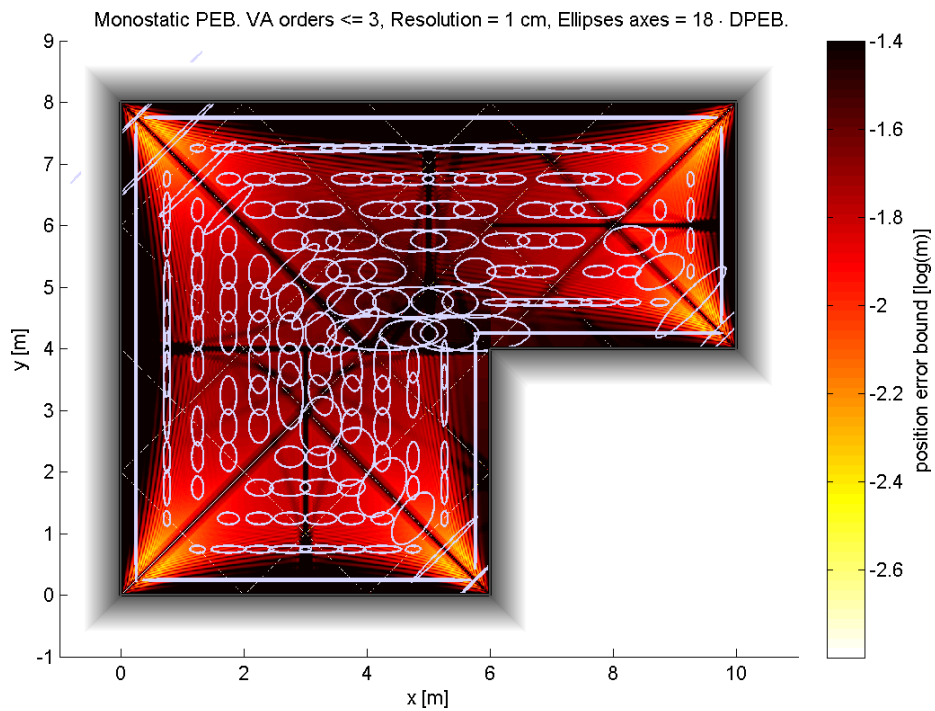


Figure 4.31: Error ellipses show the directivity of the PEB during third-order monostatic localization. Path overlap is considered. Half-axes were enlarged by a factor of 18 for illustration purposes.

5

Cooperative Localization

In this chapter, we examine the cooperative scenario that was outlined in Section 2.1. A total of M mobile agents are located in an indoor environment and perform all monostatic and bistatic measurements. \mathbf{p}_m and \mathbf{p}_j are the receiver (RX) and transmitter (TX) agent positions of the current transmission, where $1 \leq m, j \leq M$. The cooperative idea is to estimate all agent positions $\mathbf{p}_1, \dots, \mathbf{p}_M$ jointly from the entirety of measurements. Due to diffuse multipath (DMP) and noisy measurements, the joint position estimate is subject to uncertainty. Therefore, we derive the Cramér-Rao lower bound (CRLB) as a means to quantify and study this uncertainty.

5.1 Cooperative CRLB Derivation

As a prerequisite, we define a stack vector of all received signals

$$\mathbf{r} := (\mathbf{r}_{1,1}^T, \mathbf{r}_{1,2}^T, \dots, \mathbf{r}_{1,M}^T, \mathbf{r}_{2,1}^T, \dots, \mathbf{r}_{M,M-1}^T, \mathbf{r}_{M,M}^T)^T \quad (5.1)$$

that serves as observation for estimating $\boldsymbol{\theta}$. We recall stack vectors (2.7) (2.8) of all delays and amplitudes within one transmission from the j -th to the m -th agent

$$\begin{aligned} \boldsymbol{\tau}_{m,j} &:= \left(\tau_{m,j}^{(1)}, \dots, \tau_{m,j}^{(K_{m,j})} \right)^T \\ \boldsymbol{\alpha}_{m,j} &:= \left(\alpha_{m,j}^{(1)}, \dots, \alpha_{m,j}^{(K_{m,j})} \right)^T \end{aligned}$$

with dimensionality $\boldsymbol{\tau}_{m,j} \in \mathbb{R}_+^{K_{m,j}}$, $\boldsymbol{\alpha}_{m,j} \in \mathbb{C}^{K_{m,j}}$. Additionally, we define "global" stack vectors

$$\mathbf{p} := (\mathbf{p}_1^T, \dots, \mathbf{p}_M^T)^T \quad (5.2)$$

$$\boldsymbol{\tau} := (\boldsymbol{\tau}_{1,1}^T, \boldsymbol{\tau}_{1,2}^T, \dots, \boldsymbol{\tau}_{1,M}^T, \boldsymbol{\tau}_{2,1}^T, \dots, \boldsymbol{\tau}_{M,M-1}^T, \boldsymbol{\tau}_{M,M}^T)^T \quad (5.3)$$

$$\boldsymbol{\alpha} := (\boldsymbol{\alpha}_{1,1}^T, \boldsymbol{\alpha}_{1,2}^T, \dots, \boldsymbol{\alpha}_{1,M}^T, \boldsymbol{\alpha}_{2,1}^T, \dots, \boldsymbol{\alpha}_{M,M-1}^T, \boldsymbol{\alpha}_{M,M}^T)^T \quad (5.4)$$

where $\mathbf{p} \in \mathbb{R}^{2M}$, $\boldsymbol{\tau} \in \mathbb{R}_+^K$, $\boldsymbol{\alpha} \in \mathbb{C}^K$ and $K := \sum_m \sum_j K_{m,j}$ is the total number of multipath components (MPCs).

The cooperative parameter vector $\boldsymbol{\theta}$ is composed of all agent positions (obviously our main interest in a localization problem) and the MPC amplitudes of all transmissions as nuisance

parameters.

$$\boldsymbol{\theta} := (\mathbf{p}^T, \Re\boldsymbol{\alpha}^T, \Im\boldsymbol{\alpha}^T)^T \quad (5.5)$$

Like in Section 4.1, we transform the estimation problem to a signal parameter space

$$\boldsymbol{\psi} := (\boldsymbol{\tau}^T, \Re\boldsymbol{\alpha}^T, \Im\boldsymbol{\alpha}^T)^T \quad (5.6)$$

with dimensionality $\dim\boldsymbol{\psi} = 3K > \dim\boldsymbol{\theta} = 2M + 2K$.

We account for the distribution of observation \mathbf{r} with a joint log-likelihood function $\ln f(\mathbf{r}|\boldsymbol{\theta})$. Conditioned on $\boldsymbol{\theta}$, measurements $\mathbf{r}_{m,j}$ are independent [2], so

$$\ln f(\mathbf{r}|\boldsymbol{\theta}) = \ln \prod_{m=1}^M \prod_{j=1}^M f(\mathbf{r}_{m,j}|\boldsymbol{\theta}) = \sum_{m=1}^M \sum_{j=1}^M \ln f(\mathbf{r}_{m,j}|\boldsymbol{\theta}) .$$

Conditioned on the involved agent positions $\mathbf{p}_m, \mathbf{p}_j$ and amplitudes $\boldsymbol{\alpha}_{m,j}$ of the transmission in question, the single transmission likelihood function (LHF) is furthermore independent [2] of all other parameters in $\boldsymbol{\theta}$, i.e. $f(\mathbf{r}_{m,j}|\boldsymbol{\theta}) = f(\mathbf{r}_{m,j}|\mathbf{p}_m, \mathbf{p}_j, \boldsymbol{\alpha}_{m,j})$. For reasons explained in Footnote 19 of Section 4.1, we write $f(\mathbf{r}_{m,j}|\boldsymbol{\tau}_{m,j}, \boldsymbol{\alpha}_{m,j})$ instead and use LHF (2.5), which describes all monostatically or bistatically received signals within our model of the DMP channel and measurements impaired by additive white Gaussian noise (AWGN). Our ultimately used version of the joint log-LHF is

$$\ln f(\mathbf{r}|\boldsymbol{\psi}) = \sum_{m=1}^M \sum_{j=1}^M \ln f(\mathbf{r}_{m,j}|\boldsymbol{\tau}_{m,j}, \boldsymbol{\alpha}_{m,j}) . \quad (5.7)$$

5.1.1 FIM, Parameter Transformation and EFIM

Like in Section 4.1, we adopt the notation from [2] for Fisher information (FI) among some parameters \mathbf{x}, \mathbf{y} over the single transmission LHF (2.5)

$$\Phi_{m,j}(\mathbf{x}, \mathbf{y}) := \mathbb{E}_{\mathbf{r}_{m,j}|\boldsymbol{\tau}_{m,j}, \boldsymbol{\alpha}_{m,j}} \left\{ -\frac{\partial^2 \ln f(\mathbf{r}_{m,j}|\boldsymbol{\tau}_{m,j}, \boldsymbol{\alpha}_{m,j})}{\partial \mathbf{x} \partial \mathbf{y}^T} \right\} .$$

We further adopt an equivalent notation for use in cooperative derivations. We write

$$\Phi(\mathbf{x}, \mathbf{y}) := \mathbb{E}_{\mathbf{r}|\boldsymbol{\psi}} \left\{ -\frac{\partial^2 \ln f(\mathbf{r}|\boldsymbol{\psi})}{\partial \mathbf{x} \partial \mathbf{y}^T} \right\} . \quad (5.8)$$

for FI evaluated over the joint LHF (5.7). With the above notation, we can write Fisher information matrices (FIMs) for our parameter spaces $\boldsymbol{\theta}, \boldsymbol{\psi}$ as $\mathbf{J}_{\boldsymbol{\theta}} = \Phi(\boldsymbol{\theta}, \boldsymbol{\theta})$ and $\mathbf{J}_{\boldsymbol{\psi}} = \Phi(\boldsymbol{\psi}, \boldsymbol{\psi})$. These matrices are coupled by the parameter transformation rule (2.11)

$$\mathbf{J}_{\boldsymbol{\theta}} = \frac{\partial \boldsymbol{\psi}}{\partial \boldsymbol{\theta}} \cdot \mathbf{J}_{\boldsymbol{\psi}} \cdot \frac{\partial \boldsymbol{\psi}^T}{\partial \boldsymbol{\theta}} \quad (5.9)$$

where the Jacobian matrices²¹ have the structure (cf. Section 4.1)

$$\frac{\partial \boldsymbol{\psi}}{\partial \boldsymbol{\theta}} = \begin{pmatrix} \partial \boldsymbol{\tau} / \partial \mathbf{p} & \mathbf{0}_{2M \times 2K} \\ \mathbf{0}_{2K \times K} & \mathbf{I}_{2K \times 2K} \end{pmatrix} . \quad (5.10)$$

Again, the influence of room geometry is given by the Jacobian $\partial\boldsymbol{\tau}/\partial\mathbf{p}$ with structure

$$\frac{\partial\boldsymbol{\tau}}{\partial\mathbf{p}} = \begin{pmatrix} \frac{\partial\tau_{1,1}}{\partial\mathbf{p}_1} & \frac{\partial\tau_{1,2}}{\partial\mathbf{p}_1} & \dots & \frac{\partial\tau_{M,M}}{\partial\mathbf{p}_1} \\ \vdots & & & \vdots \\ \frac{\partial\tau_{1,1}}{\partial\mathbf{p}_M} & \frac{\partial\tau_{1,2}}{\partial\mathbf{p}_M} & \dots & \frac{\partial\tau_{M,M}}{\partial\mathbf{p}_M} \end{pmatrix} \in \mathbb{R}^{2M \times K}.$$

This matrix holds all spatial delay gradients in its large block structure. This is yet another reason why the analysis of these gradients was much needed in Chapter 3 to pave the way for CRLB derivations.

FIM \mathbf{J}_ψ has a $K \times K$ block structure

$$\mathbf{J}_\psi = \Phi(\boldsymbol{\psi}, \boldsymbol{\psi}) = \begin{pmatrix} \Phi(\boldsymbol{\tau}, \boldsymbol{\tau}) & \Phi(\boldsymbol{\tau}, \Re\boldsymbol{\alpha}) & \Phi(\boldsymbol{\tau}, \Im\boldsymbol{\alpha}) \\ \Phi(\boldsymbol{\tau}, \Re\boldsymbol{\alpha})^T & \Phi(\Re\boldsymbol{\alpha}, \Re\boldsymbol{\alpha}) & 0 \\ \Phi(\boldsymbol{\tau}, \Im\boldsymbol{\alpha})^T & 0 & \Phi(\Im\boldsymbol{\alpha}, \Im\boldsymbol{\alpha}) \end{pmatrix}. \quad (5.11)$$

For the same reasons as in Section 4.1 and [6], we have $\Phi(\Re\boldsymbol{\alpha}, \Im\boldsymbol{\alpha}) = \Phi(\Im\boldsymbol{\alpha}, \Re\boldsymbol{\alpha}) = \mathbf{0}$ and furthermore $\Phi(\Re\boldsymbol{\alpha}, \Re\boldsymbol{\alpha}) = \Phi(\Im\boldsymbol{\alpha}, \Im\boldsymbol{\alpha})$ holds.

We use block structures (5.10) and (5.11) in (5.9) and perform the matrix multiplications. This yields

$$\mathbf{J}_\theta = \begin{pmatrix} \frac{\partial\boldsymbol{\tau}}{\partial\mathbf{p}} \cdot \Phi(\boldsymbol{\tau}, \boldsymbol{\tau}) \cdot \frac{\partial\boldsymbol{\tau}^T}{\partial\mathbf{p}} & \frac{\partial\boldsymbol{\tau}}{\partial\mathbf{p}} \cdot \Phi(\boldsymbol{\tau}, \Re\boldsymbol{\alpha}) & \frac{\partial\boldsymbol{\tau}}{\partial\mathbf{p}} \cdot \Phi(\boldsymbol{\tau}, \Im\boldsymbol{\alpha}) \\ \Phi(\boldsymbol{\tau}, \Re\boldsymbol{\alpha})^T \cdot \frac{\partial\boldsymbol{\tau}^T}{\partial\mathbf{p}} & \Phi(\Re\boldsymbol{\alpha}, \Re\boldsymbol{\alpha}) & 0 \\ \Phi(\boldsymbol{\tau}, \Im\boldsymbol{\alpha})^T \cdot \frac{\partial\boldsymbol{\tau}^T}{\partial\mathbf{p}} & 0 & \Phi(\Im\boldsymbol{\alpha}, \Im\boldsymbol{\alpha}) \end{pmatrix}. \quad (5.12)$$

By the definition of $\boldsymbol{\theta}$, the upper left block of \mathbf{J}_θ is $\Phi(\mathbf{p}, \mathbf{p}) \in \mathbb{R}^{2M \times 2M}$. Thus, we calculate the equivalent Fisher information matrix (EFIM) $\mathbf{J}_\mathbf{p}$ in the same fashion as in Section 4.1. The EFIM fulfills

$$[\mathbf{J}_\theta^{-1}]_{2M \times 2M} = \mathbf{J}_\mathbf{p}^{-1}$$

so we can use the diagonal of the EFIM inverse $\mathbf{J}_\mathbf{p}^{-1}$ to obtain the position error bound (PEB) of the individual agent positions. Applying the Schur complement (2.12) yields

$$\begin{aligned} \mathbf{J}_\mathbf{p} = \frac{\partial\boldsymbol{\tau}}{\partial\mathbf{p}} \cdot \Phi(\boldsymbol{\tau}, \boldsymbol{\tau}) \cdot \frac{\partial\boldsymbol{\tau}^T}{\partial\mathbf{p}} &- \frac{\partial\boldsymbol{\tau}}{\partial\mathbf{p}} \cdot \Phi(\boldsymbol{\tau}, \Re\boldsymbol{\alpha}) \cdot \Phi(\Re\boldsymbol{\alpha}, \Re\boldsymbol{\alpha})^{-1} \cdot \Phi(\boldsymbol{\tau}, \Re\boldsymbol{\alpha})^T \cdot \frac{\partial\boldsymbol{\tau}^T}{\partial\mathbf{p}} \\ &- \frac{\partial\boldsymbol{\tau}}{\partial\mathbf{p}} \cdot \Phi(\boldsymbol{\tau}, \Im\boldsymbol{\alpha}) \cdot \Phi(\Im\boldsymbol{\alpha}, \Im\boldsymbol{\alpha})^{-1} \cdot \Phi(\boldsymbol{\tau}, \Im\boldsymbol{\alpha})^T \cdot \frac{\partial\boldsymbol{\tau}^T}{\partial\mathbf{p}}. \end{aligned}$$

²¹ Again, keep in mind that the Jacobian notation used in this thesis and in most of localization and radar literature is a transposed version of Jacobians defined in most basic mathematics texts.

Preliminary result for the EFIM of cooperative localization

$$\begin{aligned} \mathbf{J}_p &= \frac{\partial \boldsymbol{\tau}}{\partial \mathbf{p}} \cdot \left(\Phi(\boldsymbol{\tau}, \boldsymbol{\tau}) - \Psi^{(\mathfrak{R})} - \Psi^{(\mathfrak{S})} \right) \cdot \frac{\partial \boldsymbol{\tau}^T}{\partial \mathbf{p}} \\ \Psi^{(\mathfrak{R})} &:= \Phi(\boldsymbol{\tau}, \mathfrak{R}\boldsymbol{\alpha}) \cdot \Phi(\mathfrak{R}\boldsymbol{\alpha}, \mathfrak{R}\boldsymbol{\alpha})^{-1} \cdot \Phi(\boldsymbol{\tau}, \mathfrak{R}\boldsymbol{\alpha})^T \\ \Psi^{(\mathfrak{S})} &:= \Phi(\boldsymbol{\tau}, \mathfrak{S}\boldsymbol{\alpha}) \cdot \Phi(\mathfrak{S}\boldsymbol{\alpha}, \mathfrak{S}\boldsymbol{\alpha})^{-1} \cdot \Phi(\boldsymbol{\tau}, \mathfrak{S}\boldsymbol{\alpha})^T \end{aligned} \quad (5.13)$$

5.1.2 Simplifications for Dimensionality Reduction

When evaluating a block $\Phi(\boldsymbol{\tau}_{m,j}, \boldsymbol{\tau}_{m',j'})$ of $\Phi(\boldsymbol{\tau}, \boldsymbol{\tau})$, the following second-order derivative arises due to the definition of Φ in (5.8).

$$\begin{aligned} \Phi(\boldsymbol{\tau}_{m,j}, \boldsymbol{\tau}_{m',j'}) &= -\mathbb{E}_{\mathbf{r}|\boldsymbol{\psi}} \left\{ \frac{\partial^2 \ln f(\mathbf{r}|\boldsymbol{\psi})}{\partial \boldsymbol{\tau}_{m',j'} \partial \boldsymbol{\tau}_{m,j}^T} \right\} \\ &= -\mathbb{E}_{\mathbf{r}|\boldsymbol{\psi}} \left\{ \frac{\partial}{\partial \boldsymbol{\tau}_{m',j'}} \left(\frac{\partial}{\partial \boldsymbol{\tau}_{m,j}^T} \sum_{\tilde{m}=1}^M \sum_{\tilde{j}=1}^M \ln f(\mathbf{r}_{\tilde{m},\tilde{j}} | \boldsymbol{\tau}_{\tilde{m},\tilde{j}}, \boldsymbol{\alpha}_{\tilde{m},\tilde{j}}) \right) \right\} \\ &= -\mathbb{E}_{\mathbf{r}|\boldsymbol{\psi}} \left\{ \frac{\partial}{\partial \boldsymbol{\tau}_{m',j'}} \left(\frac{\partial}{\partial \boldsymbol{\tau}_{m,j}^T} \ln f(\mathbf{r}_{m,j} | \boldsymbol{\tau}_{m,j}, \boldsymbol{\alpha}_{m,j}) \right) \right\} \\ &= -\mathbb{E}_{\mathbf{r}|\boldsymbol{\psi}} \left\{ \delta_{m,m'} \cdot \delta_{j,j'} \cdot \frac{\partial^2 \ln f(\mathbf{r}_{m,j} | \boldsymbol{\tau}_{m,j}, \boldsymbol{\alpha}_{m,j})}{\partial \boldsymbol{\tau}_{m,j} \partial \boldsymbol{\tau}_{m,j}^T} \right\} \\ &= \delta_{m,m'} \cdot \delta_{j,j'} \cdot \Phi_{m,j}(\boldsymbol{\tau}_{m,j}, \boldsymbol{\tau}_{m,j}) \end{aligned}$$

The above expression is non-zero if and only if $m = m' \wedge j = j'$. Hence, FI over the joint LHF among measurement-specific quantities (given by m, j) either becomes zero if the quantities are from different measurements or reduces to FI over the single-measurement LHF (expressed by $\Phi_{m,j}$).

The equivalent simplifications hold for $\Phi(\boldsymbol{\tau}_{m,j}, \boldsymbol{\alpha}_{m',j'})$ and $\Phi(\boldsymbol{\alpha}_{m,j}, \boldsymbol{\alpha}_{m',j'})$. Thus, all blocks of \mathbf{J}_ψ in (5.11) have a block-diagonal structure

$$\begin{aligned} \Phi(\boldsymbol{\tau}, \boldsymbol{\tau}) &= \text{diag}(\Phi_{1,1}(\boldsymbol{\tau}_{1,1}, \boldsymbol{\tau}_{1,1}), \dots, \Phi_{1,M}(\boldsymbol{\tau}_{1,M}, \boldsymbol{\tau}_{1,M}), \Phi_{2,1}(\boldsymbol{\tau}_{2,1}, \boldsymbol{\tau}_{2,1}), \dots \\ &\quad \dots, \Phi_{M,M-1}(\boldsymbol{\tau}_{M,M-1}, \boldsymbol{\tau}_{M,M-1}), \Phi_{M,M}(\boldsymbol{\tau}_{M,M}, \boldsymbol{\tau}_{M,M})) \\ \Phi(\boldsymbol{\tau}, \mathfrak{R}\boldsymbol{\alpha}) &= \text{diag}(\Phi_{1,1}(\boldsymbol{\tau}_{1,1}, \mathfrak{R}\boldsymbol{\alpha}_{1,1}), \dots, \Phi_{M,M}(\boldsymbol{\tau}_{M,M}, \mathfrak{R}\boldsymbol{\alpha}_{M,M})) \\ \Phi(\mathfrak{R}\boldsymbol{\alpha}, \mathfrak{R}\boldsymbol{\alpha})^{-1} &= \text{diag}(\Phi_{1,1}(\mathfrak{R}\boldsymbol{\alpha}_{1,1}, \mathfrak{R}\boldsymbol{\alpha}_{1,1})^{-1}, \dots, \Phi_{M,M}(\mathfrak{R}\boldsymbol{\alpha}_{M,M}, \mathfrak{R}\boldsymbol{\alpha}_{M,M})^{-1}) \end{aligned}$$

where each diagonal block corresponds to a measurement $\mathbf{r}_{m,j}$. Statements made about $\mathfrak{R}\boldsymbol{\alpha}$ hold for $\mathfrak{S}\boldsymbol{\alpha}$ analogously. The product of three block-diagonal matrices $\Psi^{(\mathfrak{R})} = \Phi(\boldsymbol{\tau}, \mathfrak{R}\boldsymbol{\alpha}) \cdot \Phi(\mathfrak{R}\boldsymbol{\alpha}, \mathfrak{R}\boldsymbol{\alpha})^{-1} \cdot \Phi(\boldsymbol{\tau}, \mathfrak{R}\boldsymbol{\alpha})$ is block-diagonal as well, hence this also holds for $\Phi(\boldsymbol{\tau}, \boldsymbol{\tau}) - \Psi^{(\mathfrak{R})} - \Psi^{(\mathfrak{S})}$. We define

$$\begin{aligned} \Psi_{m,j}^{(\mathfrak{R})} &:= \Phi_{m,j}(\boldsymbol{\tau}_{m,j}, \mathfrak{R}\boldsymbol{\alpha}_{m,j}) \cdot \Phi_{m,j}(\mathfrak{R}\boldsymbol{\alpha}, \mathfrak{R}\boldsymbol{\alpha}_{m,j})^{-1} \cdot \Phi_{m,j}(\boldsymbol{\tau}_{m,j}, \mathfrak{R}\boldsymbol{\alpha}_{m,j})^T \\ \Psi_{m,j}^{(\mathfrak{S})} &:= \Phi_{m,j}(\boldsymbol{\tau}_{m,j}, \mathfrak{S}\boldsymbol{\alpha}_{m,j}) \cdot \Phi_{m,j}(\mathfrak{S}\boldsymbol{\alpha}, \mathfrak{S}\boldsymbol{\alpha}_{m,j})^{-1} \cdot \Phi_{m,j}(\boldsymbol{\tau}_{m,j}, \mathfrak{S}\boldsymbol{\alpha}_{m,j})^T \\ \Lambda_{m,j} &:= \Phi_{m,j}(\boldsymbol{\tau}_{m,j}, \boldsymbol{\tau}_{m,j}) - \Psi_{m,j}^{(\mathfrak{R})} - \Psi_{m,j}^{(\mathfrak{S})} \end{aligned}$$

and write the EFIM like

$$\begin{aligned} \mathbf{J}_{\mathbf{p}} &= \frac{\partial \boldsymbol{\tau}}{\partial \mathbf{p}} \cdot \text{diag}(\boldsymbol{\Lambda}_{1,1}, \dots, \boldsymbol{\Lambda}_{M,M}) \cdot \frac{\partial \boldsymbol{\tau}^T}{\partial \mathbf{p}} \\ &= \left(\frac{\partial \boldsymbol{\tau}_{1,1}}{\partial \mathbf{p}}, \dots, \frac{\partial \boldsymbol{\tau}_{M,M}}{\partial \mathbf{p}} \right) \cdot \begin{pmatrix} \boldsymbol{\Lambda}_{1,1} & & \mathbf{0} \\ & \ddots & \\ \mathbf{0} & & \boldsymbol{\Lambda}_{M,M} \end{pmatrix} \cdot \begin{pmatrix} \frac{\partial \boldsymbol{\tau}_{1,1}^T}{\partial \mathbf{p}} \\ \vdots \\ \frac{\partial \boldsymbol{\tau}_{M,M}^T}{\partial \mathbf{p}} \end{pmatrix} \end{aligned}$$

which reduces to a sum of contributions from individual measurements $\mathbf{r}_{m,j}$.

EFIM summation structure

$$\mathbf{J}_{\mathbf{p}} = \sum_{m=1}^M \sum_{j=1}^M \frac{\partial \boldsymbol{\tau}_{m,j}}{\partial \mathbf{p}} \cdot \boldsymbol{\Lambda}_{m,j} \cdot \frac{\partial \boldsymbol{\tau}_{m,j}^T}{\partial \mathbf{p}}. \quad (5.14)$$

The Jacobian $\partial \boldsymbol{\tau}_{m,j} / \partial \mathbf{p}$ is sparse because the only agent positions that $\boldsymbol{\tau}_{m,j}$ depends on are \mathbf{p}_m and \mathbf{p}_j . The remaining $M-2$ agent positions do not influence $\boldsymbol{\tau}_{m,j}$ and hence result in a vanishing derivative (for details see Chapter 3).²²

$$\frac{\partial \boldsymbol{\tau}_{m,j}}{\partial \mathbf{p}} = \left(\mathbf{0}, \dots, \mathbf{0}, \frac{\partial \boldsymbol{\tau}_{m,j}^T}{\partial \mathbf{p}_m}, \mathbf{0}, \dots, \mathbf{0}, \frac{\partial \boldsymbol{\tau}_{m,j}^T}{\partial \mathbf{p}_j}, \mathbf{0}, \dots, \mathbf{0} \right)^T \quad (5.15)$$

Only the m -th and j -th row blocks (dimension $2 \times K_{m,j}$ blocks) are non-zero. Thus, all summands of (5.14) are sparse as well. For convenience, we define a symbol for EFIM (5.14) summands

$$\mathbf{S}_{m,j} := \frac{\partial \boldsymbol{\tau}_{m,j}}{\partial \mathbf{p}} \cdot \boldsymbol{\Lambda}_{m,j} \cdot \frac{\partial \boldsymbol{\tau}_{m,j}^T}{\partial \mathbf{p}}.$$

The only non-zero blocks and thus contributions to EFIM $\mathbf{J}_{\mathbf{p}}$ of bistatic summands $\mathbf{S}_{m,j}$, $m \neq j$ are, on the one hand, the two off-diagonal blocks

$$[\mathbf{S}_{m,j}]_{2 \times 2, m, j} = \frac{\partial \boldsymbol{\tau}_{m,j}}{\partial \mathbf{p}_m} \cdot \boldsymbol{\Lambda}_{m,j} \cdot \frac{\partial \boldsymbol{\tau}_{m,j}^T}{\partial \mathbf{p}_j}, \quad [\mathbf{S}_{m,j}]_{2 \times 2, j, m} = \frac{\partial \boldsymbol{\tau}_{m,j}}{\partial \mathbf{p}_j} \cdot \boldsymbol{\Lambda}_{m,j} \cdot \frac{\partial \boldsymbol{\tau}_{m,j}^T}{\partial \mathbf{p}_m} \quad (5.16)$$

and on the other hand, the two on-diagonal blocks

$$[\mathbf{S}_{m,j}]_{2 \times 2, m, m} = \frac{\partial \boldsymbol{\tau}_{m,j}}{\partial \mathbf{p}_m} \cdot \boldsymbol{\Lambda}_{m,j} \cdot \frac{\partial \boldsymbol{\tau}_{m,j}^T}{\partial \mathbf{p}_m}, \quad [\mathbf{S}_{m,j}]_{2 \times 2, j, j} = \frac{\partial \boldsymbol{\tau}_{m,j}}{\partial \mathbf{p}_j} \cdot \boldsymbol{\Lambda}_{m,j} \cdot \frac{\partial \boldsymbol{\tau}_{m,j}^T}{\partial \mathbf{p}_j}. \quad (5.17)$$

Monostatic summands $\mathbf{S}_{j,j}$ contribute exclusively to on-diagonal EFIM blocks

$$[\mathbf{S}_{j,j}]_{2 \times 2, j, j} = \frac{\partial \boldsymbol{\tau}_{j,j}}{\partial \mathbf{p}_j} \cdot \boldsymbol{\Lambda}_{j,j} \cdot \frac{\partial \boldsymbol{\tau}_{j,j}^T}{\partial \mathbf{p}_j}. \quad (5.18)$$

This yields M monostatic and $4M(M-1)$ bistatic contributions, so a total of $4M(M-1) + M$.

The reverse question is: Which summands contribute to a given EFIM block? For off-diagonal

²² Equation (5.15) indicates $m < j$, but this is an arbitrary choice. Cases $m = j$ and $m > j$ occur as well.

result blocks $m \neq j$, we get

$$[\mathbf{J}_{\mathbf{p}}]_{2 \times 2, m, j} = f(\mathbf{S}_{m, j}, \mathbf{S}_{j, m}) = [\mathbf{S}_{m, j} + \mathbf{S}_{j, m}]_{2 \times 2, m, j} = [\mathbf{S}_{m, j}]_{2 \times 2, m, j} + [\mathbf{S}_{j, m}]_{2 \times 2, m, j} .$$

We apply (5.16) on the summands and get the following result.²³

Off-diagonal m, j -th EFIM block

$$[\mathbf{J}_{\mathbf{p}}]_{2 \times 2, m, j} = \frac{\partial \tau_{m, j}}{\partial \mathbf{p}_m} \cdot \boldsymbol{\Lambda}_{m, j} \cdot \frac{\partial \tau_{m, j}}{\partial \mathbf{p}_j}^T + \frac{\partial \tau_{j, m}}{\partial \mathbf{p}_m} \cdot \boldsymbol{\Lambda}_{j, m} \cdot \frac{\partial \tau_{j, m}}{\partial \mathbf{p}_j}^T \quad (5.19)$$

On-diagonal EFIM blocks on the other hand get contributions from all summands that involve agent j in some way.

$$[\mathbf{J}_{\mathbf{p}}]_{2 \times 2, j, j} = \left[\underbrace{\mathbf{S}_{j, j}}_{\text{Monostatic}} + \underbrace{\mathbf{S}_{1, j} + \dots + \mathbf{S}_{j-1, j} + \mathbf{S}_{j+1, j} + \dots + \mathbf{S}_{M, j}}_{\text{Agent } j \text{ was bistatic TX}} + \underbrace{\mathbf{S}_{j, 1} + \dots + \mathbf{S}_{j, j-1} + \mathbf{S}_{j, j+1} + \dots + \mathbf{S}_{j, M}}_{\text{Agent } j \text{ was bistatic RX}} \right]_{2 \times 2, j, j}$$

By proceeding in our established fashion and carefully substituting (5.17) and (5.18), we obtain an on-diagonal result.

On-diagonal j, j -th EFIM block

$$[\mathbf{J}_{\mathbf{p}}]_{2 \times 2, j, j} = \frac{\partial \tau_{j, j}}{\partial \mathbf{p}_j} \cdot \boldsymbol{\Lambda}_{j, j} \cdot \frac{\partial \tau_{j, j}}{\partial \mathbf{p}_j}^T + \sum_{\substack{m=1 \\ m \neq j}}^M \frac{\partial \tau_{m, j}}{\partial \mathbf{p}_j} \cdot \boldsymbol{\Lambda}_{m, j} \cdot \frac{\partial \tau_{m, j}}{\partial \mathbf{p}_j}^T + \sum_{\substack{m'=1 \\ m' \neq j}}^M \frac{\partial \tau_{j, m'}}{\partial \mathbf{p}_j} \cdot \boldsymbol{\Lambda}_{j, m'} \cdot \frac{\partial \tau_{j, m'}}{\partial \mathbf{p}_j}^T \quad (5.20)$$

The M on-diagonal blocks get $1 + 2(M - 1)$ contributions each while the $M(M - 1)$ off-diagonal blocks get 2 each. That is a total of $M + 2M(M - 1) + 2M(M - 1)$, which is equal to the $4M(M - 1) + M$ “produced” contributions calculated earlier. Production and consumption are necessarily balanced.

5.1.3 Alternative Representation

In Chapter 3 we learned about spatial delay gradients. The Jacobian is given by (3.28)

$$\left[\frac{\partial \tau_{m, j}}{\partial \mathbf{p}_\eta} \right]_{:, k} = \frac{\partial \tau_{m, j}^{(k)}}{\partial \mathbf{p}_\eta} = \frac{1}{c} \left(\delta_{m, \eta} \cdot \mathbf{e}(\phi_{m, j}^{(k)}) - \delta_{\eta, j} \cdot \mathbf{e}((-1)^{Q_{m, j}^{(k)}} \cdot \phi_{m, j}^{(k)} + 2\gamma_{m, j}^{(k)}) \right) \quad (5.21)$$

We define two matrices $\mathbf{R}_{m, j}, \mathbf{T}_{m, j} \in \mathbb{R}^{2 \times K_{m, j}}$ that hold the RX and TX dependent portions of

²³ When subscripts like j, m or j, m' occur in summations, we violate our own conventions by referring to a RX agent via index j . We accept this infringement for the sake of avoiding an introduction of further indices.

(5.21) respectively

$$\frac{\partial \boldsymbol{\tau}_{m,j}}{\partial \mathbf{p}_\eta} = \delta_{m,\eta} \cdot \mathbf{R}_{m,j} - \delta_{\eta,j} \cdot \mathbf{T}_{m,j}$$

$$[\mathbf{R}_{m,j}]_{:,k} := \frac{1}{c} \mathbf{e}(\phi_{m,j}^{(k)}) \quad (5.22)$$

$$[\mathbf{T}_{m,j}]_{:,k} := \frac{1}{c} \mathbf{e}((-1)^{Q_{m,j}^{(k)}} \cdot \phi_{m,j}^{(k)} + 2\gamma_{m,j}^{(k)}) \quad (5.23)$$

This turns off-diagonal EFIM blocks (5.19) into

$$[\mathbf{J}_\mathbf{p}]_{2 \times 2, m, j} = -\mathbf{R}_{m,j} \cdot \boldsymbol{\Lambda}_{m,j} \cdot \mathbf{T}_{m,j}^T - \mathbf{T}_{j,m} \cdot \boldsymbol{\Lambda}_{j,m} \cdot \mathbf{R}_{j,m}^T =: -\mathbf{C}_{m,j} \cdot$$

where we defined a matrix symbol $\mathbf{C}_{m,j}$. By inspection of the first summand of an on-diagonal EFIM block (5.20), we realize

$$\begin{aligned} \frac{\partial \boldsymbol{\tau}_{j,j}}{\partial \mathbf{p}_j} \cdot \boldsymbol{\Lambda}_{j,j} \cdot \frac{\partial \boldsymbol{\tau}_{j,j}^T}{\partial \mathbf{p}_j} &= (\mathbf{R}_{j,j} - \mathbf{T}_{j,j}) \cdot \boldsymbol{\Lambda}_{j,j} \cdot (\mathbf{R}_{j,j} - \mathbf{T}_{j,j})^T \\ &= \underbrace{\mathbf{R}_{j,j} \cdot \boldsymbol{\Lambda}_{j,j} \cdot \mathbf{R}_{j,j}^T + \mathbf{T}_{j,j} \cdot \boldsymbol{\Lambda}_{j,j} \cdot \mathbf{T}_{j,j}^T}_{\text{Combinable with summations}} - \underbrace{\mathbf{R}_{j,j} \cdot \boldsymbol{\Lambda}_{j,j} \cdot \mathbf{T}_{j,j}^T - \mathbf{T}_{j,j} \cdot \boldsymbol{\Lambda}_{j,j} \cdot \mathbf{R}_{j,j}^T}_{=-\mathbf{C}_{j,j}} \cdot \end{aligned}$$

The on-diagonal EFIM blocks (5.20) then become

$$[\mathbf{J}_\mathbf{p}]_{2 \times 2, j, j} = -\mathbf{C}_{j,j} + \sum_{m'=1}^M \mathbf{T}_{m',j} \cdot \boldsymbol{\Lambda}_{m',j} \cdot \mathbf{T}_{m',j}^T + \sum_{j'=1}^M \mathbf{R}_{j,j'} \cdot \boldsymbol{\Lambda}_{j,j'} \cdot \mathbf{R}_{j,j'}^T \cdot \quad (5.24)$$

All EFIM blocks are now entirely broken down and our desired figures of merit for assessment of localization performance, the CRLB of agent positions \mathbf{p}_j for all $1 \leq j \leq M$, can readily be obtained from on-diagonal elements of $\mathbf{J}_\mathbf{p}^{-1}$. The following section gives a compact version of the CRLB results.

5.2 Cooperative Cramér–Rao Lower Bound

5.2.1 Result

PEB and squared position error bound (SPEB) [2] of the j -th agent

$$\text{SPEB}(\mathbf{p}_j) = \text{tr} \left\{ [\mathbf{J}_{\mathbf{p}}^{-1}]_{2 \times 2, j, j} \right\}, \quad \text{PEB}(\mathbf{p}_j) = \sqrt{\text{SPEB}(\mathbf{p}_j)}. \quad (5.25)$$

Equivalent Fisher Information Matrix (EFIM)

$$\mathbf{J}_{\mathbf{p}} = \begin{pmatrix} \mathbf{F}_1^{\text{RX}} + \mathbf{F}_1^{\text{TX}} - \mathbf{C}_{1,1} & -\mathbf{C}_{1,2} & \cdots & -\mathbf{C}_{1,M} \\ -\mathbf{C}_{2,1} & \mathbf{F}_2^{\text{RX}} + \mathbf{F}_2^{\text{TX}} - \mathbf{C}_{2,2} & & -\mathbf{C}_{2,M} \\ \vdots & & \ddots & \\ -\mathbf{C}_{M,1} & -\mathbf{C}_{M,2} & & \mathbf{F}_M^{\text{RX}} + \mathbf{F}_M^{\text{TX}} - \mathbf{C}_{M,M} \end{pmatrix} \quad (5.26)$$

Accumulated ranging information (RI)

$$\mathbf{F}_m^{\text{RX}} = \sum_{j=1}^M \mathbf{R}_{m,j} \cdot \mathbf{\Lambda}_{m,j} \cdot \mathbf{R}_{m,j}^T \quad (5.27)$$

$$\mathbf{F}_j^{\text{TX}} = \sum_{m=1}^M \mathbf{T}_{m,j} \cdot \mathbf{\Lambda}_{m,j} \cdot \mathbf{T}_{m,j}^T \quad (5.28)$$

$$\mathbf{C}_{m,j} = \mathbf{R}_{m,j} \cdot \mathbf{\Lambda}_{m,j} \cdot \mathbf{T}_{m,j}^T + \mathbf{T}_{j,m} \cdot \mathbf{\Lambda}_{j,m} \cdot \mathbf{R}_{j,m}^T.$$

FI of MPC delays, impaired by path overlap

$$\begin{aligned} \mathbf{\Lambda}_{m,j} &= \Phi(\tau_{m,j}, \tau_{m,j}) - \Psi_{m,j}^{(\mathfrak{R})} - \Psi_{m,j}^{(\mathfrak{S})} \\ \Psi_{m,j}^{(\mathfrak{R})} &= \Phi_{m,j}(\tau_{m,j}, \mathfrak{R}\alpha_{m,j}) \cdot \Phi_{m,j}(\mathfrak{R}\alpha_{m,j}, \mathfrak{R}\alpha_{m,j})^{-1} \cdot \Phi_{m,j}(\tau_{m,j}, \mathfrak{R}\alpha_{m,j})^T \\ \Psi_{m,j}^{(\mathfrak{S})} &= \Phi_{m,j}(\tau_{m,j}, \mathfrak{S}\alpha_{m,j}) \cdot \Phi_{m,j}(\mathfrak{S}\alpha_{m,j}, \mathfrak{S}\alpha_{m,j})^{-1} \cdot \Phi_{m,j}(\tau_{m,j}, \mathfrak{S}\alpha_{m,j})^T. \end{aligned}$$

Quantities $\Phi_{m,j}(\tau_{m,j}, \tau_{m,j})$, $\Phi_{m,j}(\tau_{m,j}, \mathfrak{R}\alpha_{m,j})$, $\Phi_{m,j}(\tau_{m,j}, \mathfrak{S}\alpha_{m,j})$ and $\Phi_{m,j}(\mathfrak{R}\alpha_{m,j}, \mathfrak{R}\alpha_{m,j}) = \Phi_{m,j}(\mathfrak{S}\alpha_{m,j}, \mathfrak{S}\alpha_{m,j})$ contain FI among signal model parameters of a particular measurement $r_{m,j}(t)$. They are adopted from [6] where the same signal and channel model are employed. Formulas are given in (A.1), (A.2), (A.4) of Appendix A.1.

RX and TX dependent components (5.22), (5.23) of the spatial gradient of MPC delays $\tau_{m,j}$

$$\begin{aligned} [\mathbf{R}_{m,j}]_{:,k} &= \frac{1}{c} \mathbf{e}(\phi_{m,j}^{(k)}) \\ [\mathbf{T}_{m,j}]_{:,k} &= \frac{1}{c} \mathbf{e}((-1)^{Q_{m,j}^{(k)}} \cdot \phi_{m,j}^{(k)} + 2\gamma_{m,j}^{(k)}). \end{aligned}$$

Effective wall angle (3.26) of an MPC of order $Q_{m,j}^{(k)}$ with wall angles $\gamma_{m,j}^{(k,q)}$

$$\gamma_{m,j}^{(k)} = \sum_{q=1}^{Q_{m,j}^{(k)}} (-1)^{Q_{m,j}^{(k)}-q} \cdot \gamma_{m,j}^{(k,q)} .$$

$Q_{m,j}^{(k)}$ is the MPC order, i.e. number of reflections. $\phi_{m,j}^{(k)}$ is the angle of arrival (AoA).

5.2.2 Discussion

To the best of our knowledge, the occurring block matrices have, from a communications engineering point-of-view, the following contributions to EFIM (5.26).

- \mathbf{F}_m^{RX} holds RI about \mathbf{p}_m from all transmissions where agent m was the RX. This implicitly includes the monostatic transmission. The structure of \mathbf{F}_m^{RX} (5.27) is equal to results from [2, 6] where fixed anchor nodes were assumed. This suggests that \mathbf{F}_m^{RX} holds ideal positioning information in a sense that agent m allegedly received pulses from perfectly known TX positions \mathbf{p}_j .
- \mathbf{F}_j^{TX} is a direct benefit of cooperation: A pulse sent from j to m does not only help the RX estimate its position \mathbf{p}_m , but additionally the joint position estimation of cooperative localization passes back the information to \mathbf{p}_j . All such information drawn from measurements $\mathbf{r}_{m,j}$ at any RX m but transmitted from this particular agent j is collected in \mathbf{F}_j^{TX} . The similarity between the structure of \mathbf{F}_j^{TX} (5.28) and \mathbf{F}_m^{RX} (5.27) implies that \mathbf{p}_j and \mathbf{p}_m attain equivalent positioning information from a half-duplex transmission $\mathbf{p}_j \rightarrow \mathbf{p}_m$ in our cooperative framework.
- $\mathbf{C}_{j,j}$ (on-diagonal) is a monostatic cross term. Together with the j -th summands of \mathbf{F}_j^{RX} and \mathbf{F}_j^{TX} , it forms a monostatic contribution, cf. derivation steps (5.20) and (5.24). Equation (5.20) may often be a more intuitive expression for on-diagonal EFIM result blocks.
- $\mathbf{C}_{m,j}$ (off-diagonal) represents an important effect in anchorless localization that is not accounted for in \mathbf{F}_m^{RX} and \mathbf{F}_j^{TX} : The uncertainty about the TX position \mathbf{p}_j when drawing positioning information from a bistatic measurement $\mathbf{r}_{m,j}$ and also the uncertainty about RX position when returning the favour through cooperation. This obviously has a negative effect on localization performance, which will be examined in the numerical results below.
- $\mathbf{\Lambda}_{m,j}$ is the available Fisher information about MPC delays of transmission $\mathbf{p}_j \rightarrow \mathbf{p}_m$. When no path overlap occurs, i.e. when $\forall k \neq k' : |\tau_{m,j}^{(k)} - \tau_{m,j}^{(k')}| > T_s$ with effective pulse duration T_s , then $\mathbf{\Lambda}_{m,j} \approx \Phi(\boldsymbol{\tau}_{m,j}, \boldsymbol{\tau}_{m,j})$ [4]. When however pulses overlap, the information is considerably decreased by $\boldsymbol{\Psi}_{m,j}^{(\Re)}$ and $\boldsymbol{\Psi}_{m,j}^{(\Im)}$, which represent the impact of uncertainties in nuisance parameter estimation $\hat{\alpha}_{m,j}^{(k)}$ on the crucial delay estimation $\hat{\tau}_{m,j}^{(k)}$. For details see Section 2.4 and [31].

A fine property of EFIM structure (5.26) is that it does not distinguish between monostatic and bistatic transmissions: Every agent transmits to and receives from M agents. The fact that in $M - 1$ of M times RX and TX are physically different agents and one time they are colocated is secondary in our result. This shows that the contributions from monostatic and bistatic measurements are fundamentally equal, just the geometry matrices and the technical parameters deep within the EFIM structure determine their individual contributions to position estimation. Those technical parameters include the lack of monostatic line of sight (LOS) paths with typically high signal-to-interference-plus-noise ratio (SINR) as well as the potentially amplified or damped RI contribution from monostatic MPCs due to the geometry-dependent agent

position sensitivity of MPC delays, cf. (4.16). Likewise, as shown in Section 4.2, many types of monostatic MPCs are worthless for localization while bistatic MPCs are not known to suffer from such problems [6, 17].

The monostatic EFIM (4.11) is actually just a corollary of the cooperative EFIM (5.26): Let the number of agents $M = 1$, then $1 \leq j \leq M \implies j = 1$, $\mathbf{p}_j = \mathbf{p}$, and $\mathbf{J}_{\mathbf{p}_j} = \mathbf{J}_{\mathbf{p}} \in \mathbb{R}^{2 \times 2}$. We use the preliminary cooperative EFIM expression (5.20) and get

$$\begin{aligned} \mathbf{J}_{\mathbf{p}_j} = \mathbf{J}_{\mathbf{p}} &= [\mathbf{J}_{\mathbf{p}}]_{2 \times 2, j, j} = \frac{\partial \boldsymbol{\tau}_{j, j}}{\partial \mathbf{p}_j} \cdot \boldsymbol{\Lambda}_{j, j} \cdot \frac{\partial \boldsymbol{\tau}_{j, j}^T}{\partial \mathbf{p}_j} + \sum_{\substack{m=1 \\ m \neq j}}^M \dots + \sum_{\substack{m'=1 \\ m' \neq j}}^M \dots \\ &= \frac{\partial \boldsymbol{\tau}_{j, j}}{\partial \mathbf{p}_j} \cdot \boldsymbol{\Lambda}_{j, j} \cdot \frac{\partial \boldsymbol{\tau}_{j, j}^T}{\partial \mathbf{p}_j} + \sum_{\substack{m=1 \\ m \neq 1}}^1 \dots + \sum_{\substack{m'=1 \\ m' \neq 1}}^1 \dots \end{aligned}$$

The sums are empty and thus zero. The remaining term is exactly the EFIM of monostatic localization (4.11). \square

Assuming channel reciprocity and consistent k -indexing of MPCs, we could argue that $\boldsymbol{\Lambda}_{m, j} = \boldsymbol{\Lambda}_{j, m}$. This does not pave the way for immediate simplifications though, since there is no simple relation between the AoAs and angles of departure (AoDs) of two reverse high-order MPCs. Thus, the bordering geometry matrices \mathbf{T} and \mathbf{R} in (5.27) and (5.28) are not combinable and \mathbf{F}_j^{TX} and \mathbf{F}_m^{RX} are inherently different. In localization schemes without multipath-assistance and a focus on the LOS component [2], such simplifications are possible due to the simple reciprocity property (3.34) of LOS path delay gradients.

EFIM (5.26) can be written as RI (non-interrelated between agents) minus the influence of bistatic TX and (because of cooperation) RX position uncertainties.

$$\mathbf{J}_{\mathbf{p}} = \text{diag}(\mathbf{F}_1^{\text{RX}} + \mathbf{F}_1^{\text{TX}} - \mathbf{C}_{1,1}, \dots, \mathbf{F}_M^{\text{RX}} + \mathbf{F}_M^{\text{TX}} - \mathbf{C}_{M,M}) - \mathbf{C}_{\text{Offdiag}}$$

where $\mathbf{C}_{\text{Offdiag}} \in \mathbb{R}^{2M \times 2M}$ is defined as $[\mathbf{C}_{\text{Offdiag}}]_{2 \times 2, m, j} := (1 - \delta_{m, j}) \cdot \mathbf{C}_{m, j}$. We define a naive EFIM that ignores the adverse effect of $\mathbf{C}_{\text{Offdiag}}$ on the localization performance

$$\mathbf{J}_{\text{Naive}} := \text{diag}(\mathbf{F}_1^{\text{RX}} + \mathbf{F}_1^{\text{TX}} - \mathbf{C}_{1,1}, \dots, \mathbf{F}_M^{\text{RX}} + \mathbf{F}_M^{\text{TX}} - \mathbf{C}_{M,M})$$

which informally²⁴ results in a loose, overly optimistic bound

$$\text{PEB}(\mathbf{p}_j) \geq \sqrt{\text{tr}\{[\mathbf{J}_{\mathbf{p}}^{-1}]_{2 \times 2, j, j}\}} \geq \sqrt{\text{tr}\{[\mathbf{J}_{\text{Naive}}^{-1}]_{2 \times 2, j, j}\}} = \sqrt{\text{tr}\{(\mathbf{F}_j^{\text{RX}} + \mathbf{F}_j^{\text{TX}} - \mathbf{C}_{j, j})^{-1}\}}. \quad (5.29)$$

While this loose bound is too ignorant towards important influences to qualify as a performance bound for engineering, it still is an interesting figure that can easily be computed on-the-fly for the study of the influence of bistatic uncertainties $\mathbf{C}_{m, j}$ on the PEB. In the numerical results below, we will observe in which situations the loose bound is close or radically different to the CRLB (5.25).

²⁴ We do not give a proof that EFIM $\mathbf{J}_{\text{Naive}}$ results in a strict lower bound that is more loose than the CRLB, but numerical results strongly suggest so for all numerically stable positions. A formal proof could be done by showing $\mathbf{J}_{\mathbf{p}}^{-1} \geq \mathbf{J}_{\text{Naive}}^{-1}$, i.e. $\mathbf{J}_{\mathbf{p}}^{-1} - \mathbf{J}_{\text{Naive}}^{-1}$ is a positive semidefinite matrix, cf. [2, 4, 12].

5.3 Cooperative Numerical Results

In this section, we compute meaningful numerical results of cooperative localization using Matlab. The approach is vastly similar to Section 4.3, so we do not explain all the details here. We assume the same channel and pulse, with the restriction to 1st and 2nd order VAs. In each scenario, there is a specified number of cooperating agents of which one is moving and the others are temporarily resting. For every position of the moving agent, we compute the cooperative PEB given by EFIM (5.26), the naive cooperative bound (5.29), the monostatic PEB given by EFIM (4.11) (i.e. the monostatic portion of (5.20)), and the bistatic PEB assuming fixed anchors at the resting nodes. The EFIM for this bistatic situation is given by the bistatic RX part of (5.20), or in detail

$$\mathbf{J}_{\mathbf{p}_m}^{\text{Bistatic}} = \sum_{\substack{j=1 \\ j \neq m}}^M \mathbf{R}_{m,j} \cdot \Lambda_{m,j} \cdot \mathbf{R}_{m,j}^T.$$

For all plots other than the monostatic ones, the resting agent positions are illustrated as green dots.

5.3.1 $M = 3$ Cooperation over a simple Room

We look at a scenario with two resting nodes at $\mathbf{p}_2 = (9 \text{ m}, 4.5 \text{ m})^T$ and $\mathbf{p}_3 = (5.6 \text{ m}, 0.75 \text{ m})^T$ while agent \mathbf{p}_1 moves around the room. All nodes have a-priori unknown position. Even though Co-MINT estimates all positions $\mathbf{p} = (\mathbf{p}_1^T, \mathbf{p}_2^T, \mathbf{p}_3^T)^T$, we only observe the position estimate $\hat{\mathbf{p}}_1$ of the moving agent.

Figure 5.1 shows the monostatic PEB, which is equivalent to an earlier result in Figure 4.23. Figure 5.2 is the bistatic PEB assuming anchors, whose outcome complies with numerical results in [6]. The cooperative PEB in Figure 5.4 is a very pleasant result: All over the room, cooperative position estimation performs very well. It beats the monostatic and bistatic approaches and combines the advantages to compensate for their individual weaknesses. The area of poorest performance is close to the left wall, where a well-studied path overlap pattern heavily impairs monostatic localization and the far distance to the resting nodes dampens bistatic contributions due to free-space path loss.

Figure 5.3 shows the spatial evolution of the naive cooperative PEB. For most positions, it is indistinguishable to the CRLB in 5.4, although areas close to the resting nodes have a lower naive bound. Also, the naive bound does not suffer from the fine pattern of reduced performance that the CRLB plot shows in the close vicinity of resting nodes. Figure 5.5 illustrates the relative difference and shows that CRLB and naive bounds are of the same order of magnitude, the biggest difference in our example being only about 25%. With the exception of numerically instable positions, the naive bound is always smaller than the CRLB.

Figure 5.6 gives the cumulative distribution function of the different PEBs and shows how cooperative localization outperforms its monostatic and bistatic equivalents with flying colours.

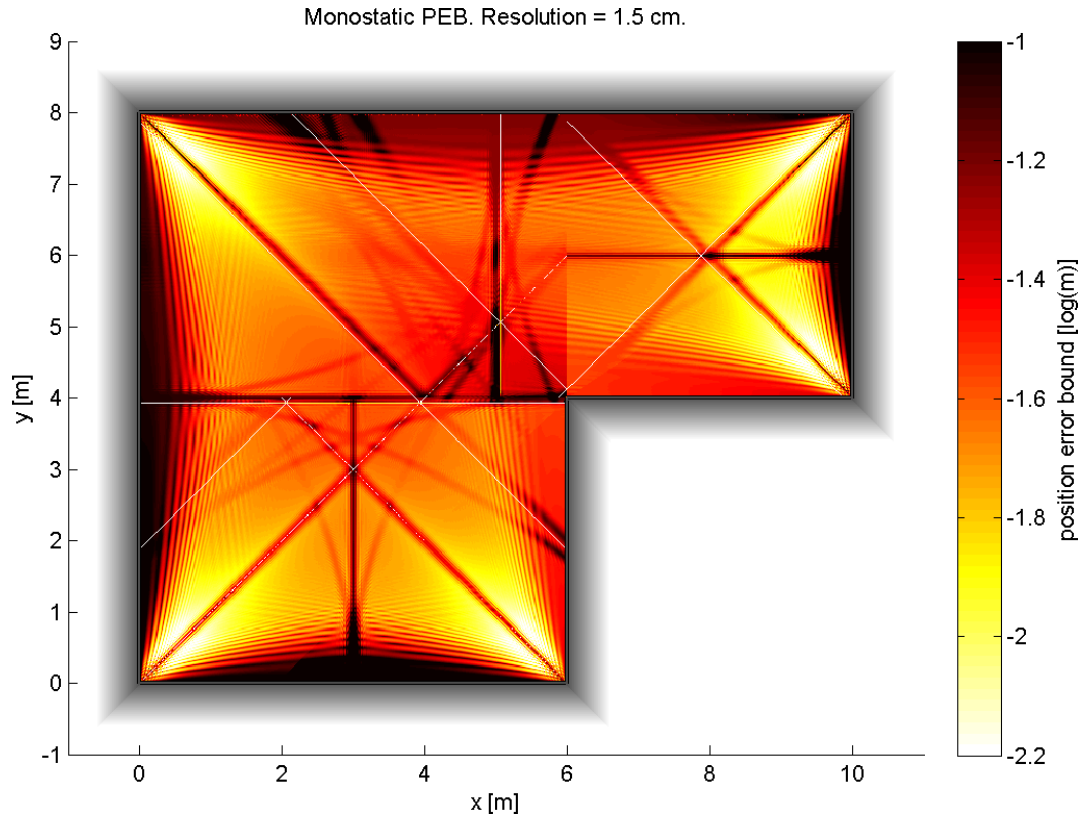


Figure 5.1: PEB of second-order monostatic localization, cf. Figure 4.23.

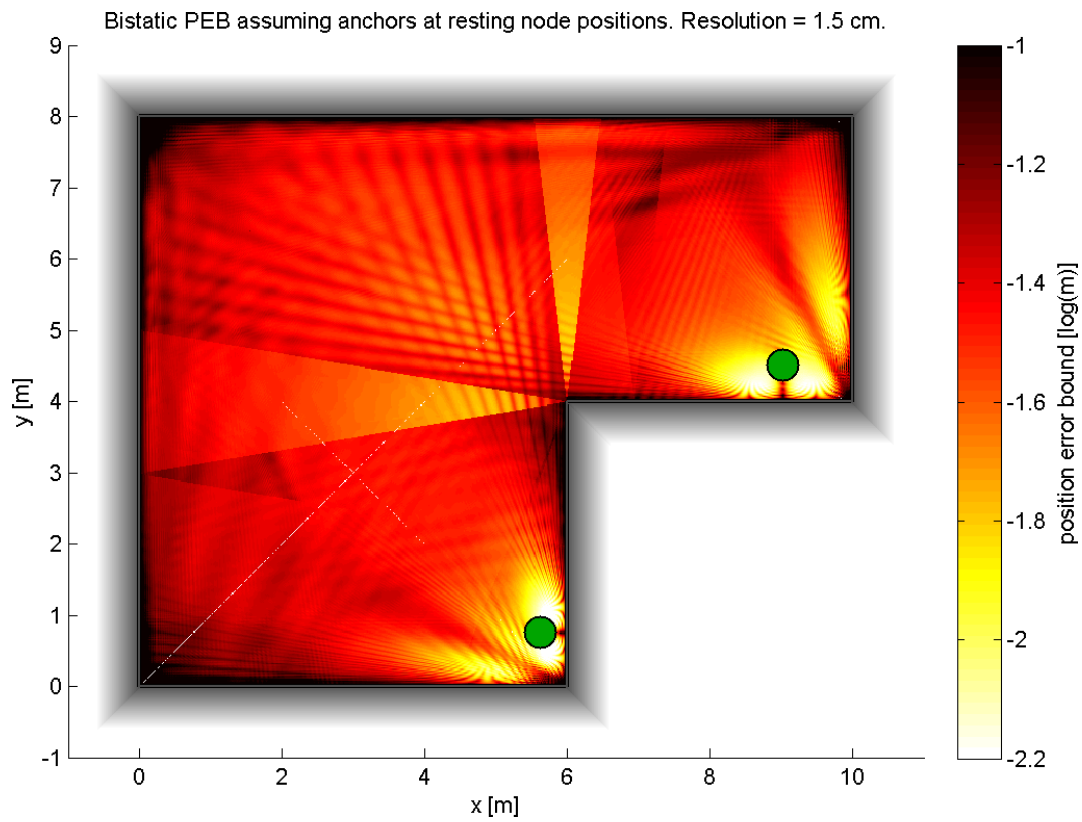


Figure 5.2: PEB of second-order bistatic multipath-assisted localization assuming anchors at the positions of the shown resting nodes.

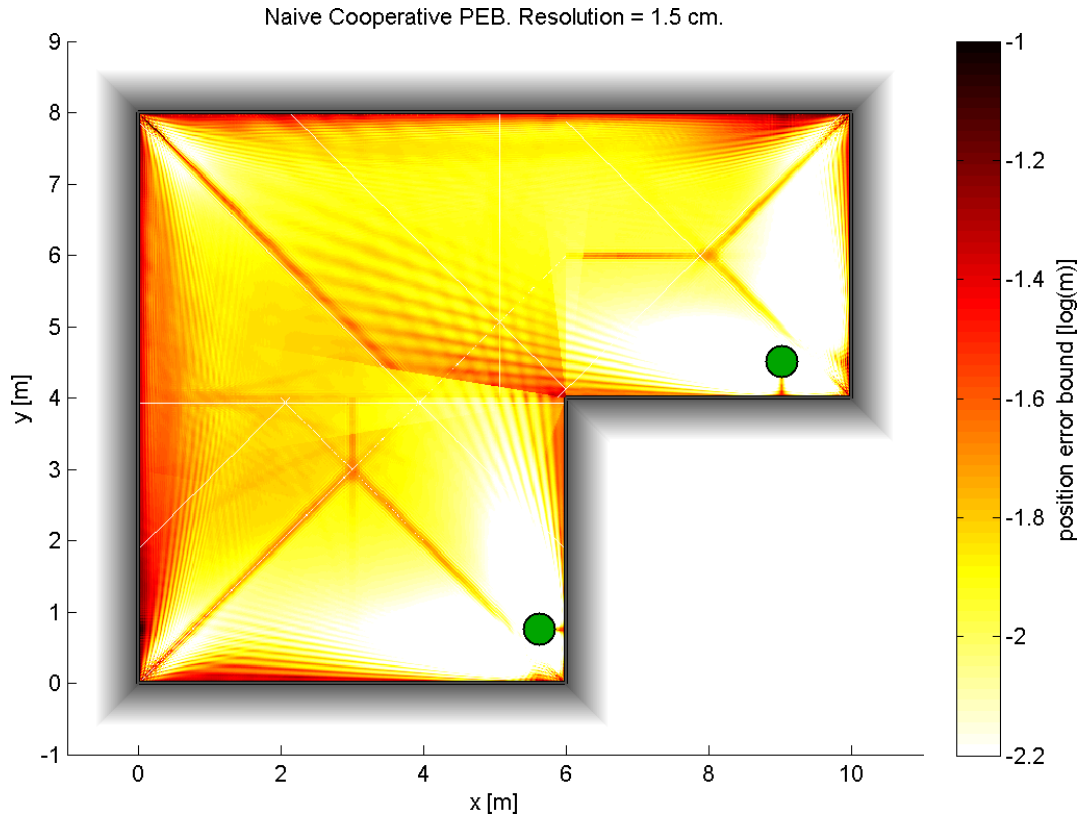


Figure 5.3: Naive cooperative PEB as defined in (5.29). This results is vastly similar to Figure 5.4, merely some areas close to the resting nodes visibly show better performance.

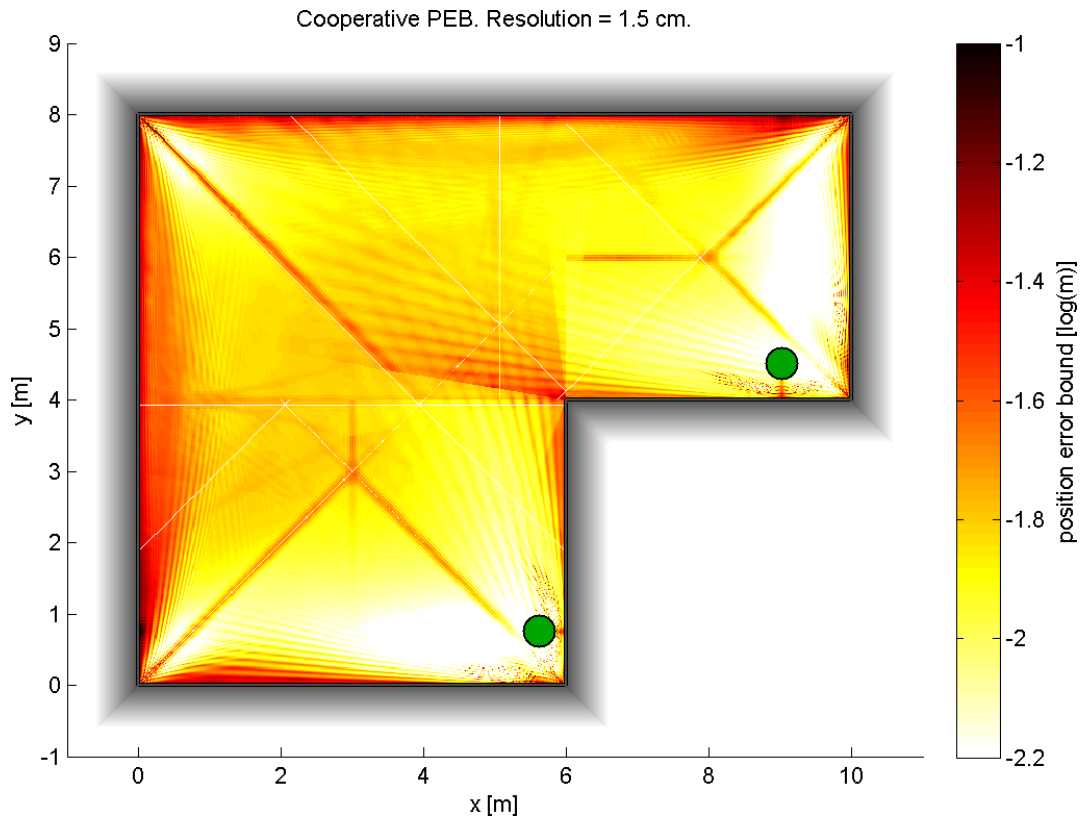


Figure 5.4: Cooperative PEB of a mobile agent in a simple room with two shown resting agents.

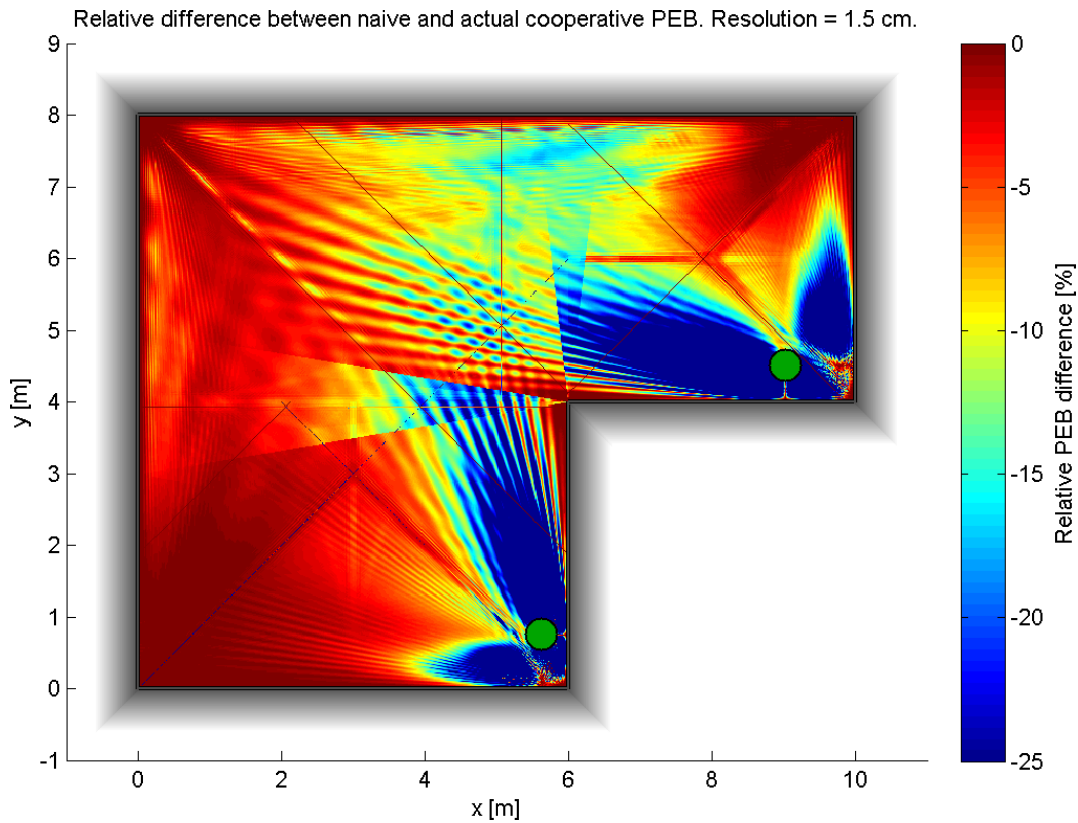


Figure 5.5: Relative difference between actual and naive cooperative PEBs from Figure 5.4 and 5.3. The blue regions show areas where the RX and TX position uncertainties during bistatic measurements have a significant impact. The red regions on the other hand show where said influence is irrelevant.

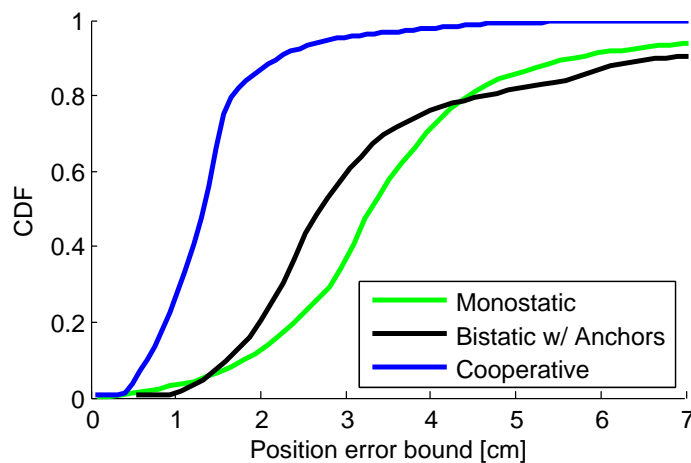


Figure 5.6: Cumulative distribution function of the different PEBs for the shown $M = 3$ cooperative localization scenario.

5.3.2 $M = 2$ Cooperation over a contorted Room

This example is similar to the previous, but now we deal with just a single resting node $\mathbf{p}_2 = (2 \text{ m}, 1.5 \text{ m})^T$ and a slightly more complex room layout with a bistatic outage region at the lower right. Figure 5.7 and 5.8 show the monostatic and bistatic performances. Figure 5.9 gives the cooperative PEB. Cooperative and monostatic performances are equal at bistatic outage positions. Figure 5.10 shows the deviations in the naive bound due to bistatic uncertainties.

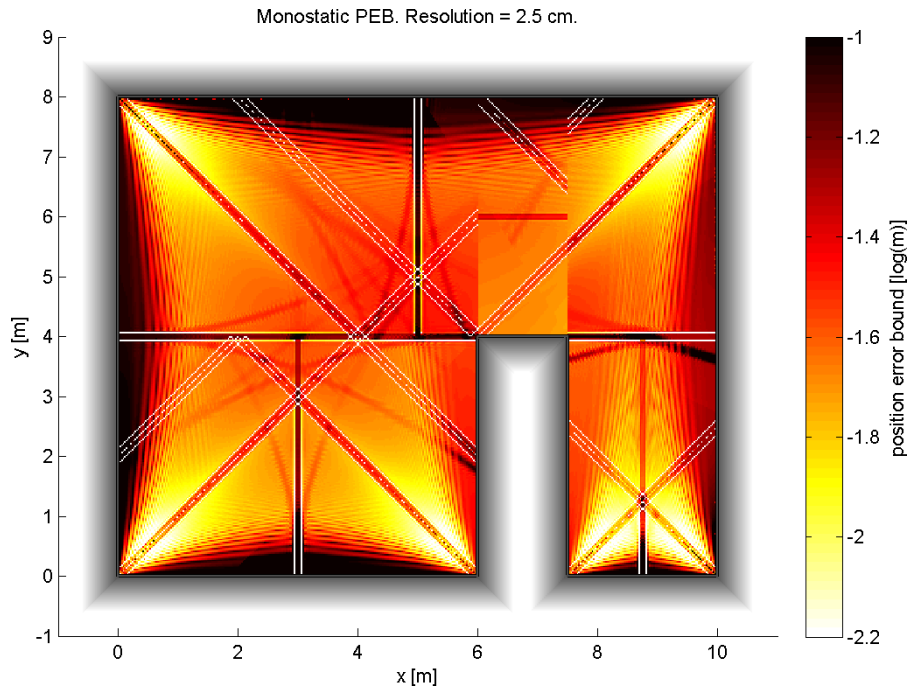


Figure 5.7: Monostatic PEB of a mobile agent in a contorted room.

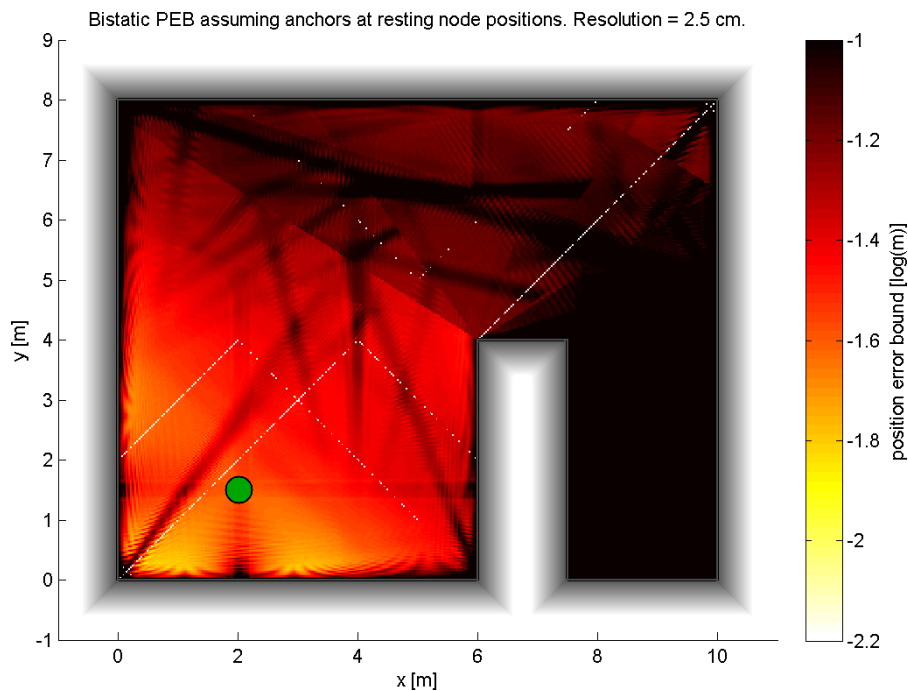


Figure 5.8: Bistatic PEB assuming an anchor at the resting agent position in a contorted room.

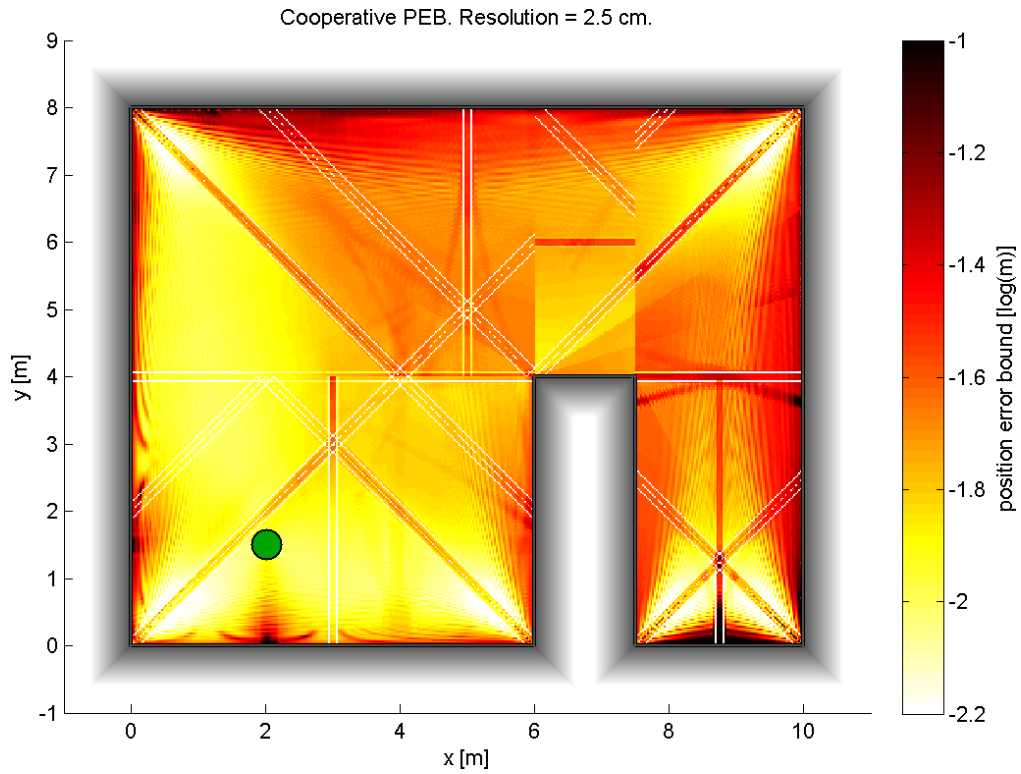


Figure 5.9: Cooperative PEB of a mobile agent and a shown resting agent in a contorted room.

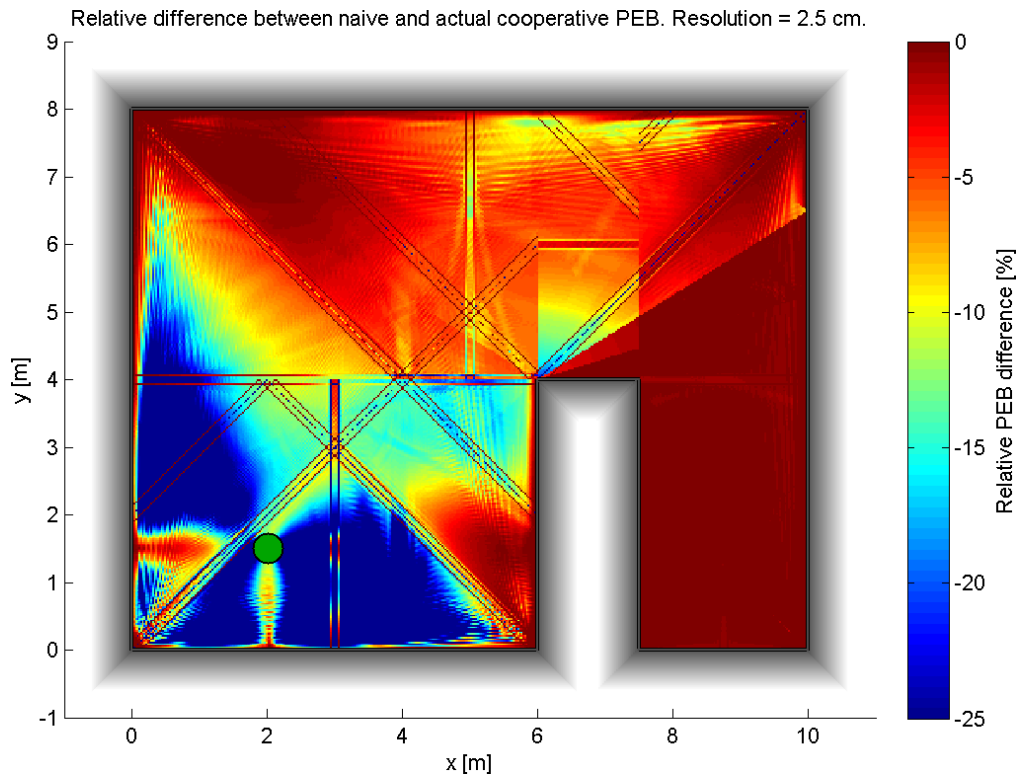


Figure 5.10: Relative difference between actual and naive cooperative PEBs. The blue regions are areas of significant bistatic uncertainty impact, while the bistatic outage region on the lower right is not affected at all.

5.3.3 M = 3 Cooperation over an involved Trajectory

In this example, we investigate an involved room with two resting nodes $\mathbf{p}_2 = (8 \text{ m}, 18.5 \text{ m})^T$ and $\mathbf{p}_3 = (12 \text{ m}, 10.5 \text{ m})^T$ and an agent \mathbf{p}_1 that moves along a trajectory. Figure 5.11 gives a detailed sketch of the arrangement where some distinct trajectory positions are marked. Again, all three agent positions are unknown a-priori.

Figure 5.12 shows enlarged error ellipses at many points of the trajectory. The ellipses nicely illustrate influences of monostatic and bistatic contributions on PEB directivity.

The different PEBs for cooperative $\hat{\mathbf{p}}_1$ estimation are shown in Figure 5.13. The cooperative PEB is at all times smaller than the monostatic and bistatic ones while the naive cooperative PEB is smaller than the actual cooperative PEB. The difference between the latter two is largest at positions of significant bistatic contributions.

Figure 5.14 shows the evolution of CRLBs of cooperative $\hat{\mathbf{p}}_1$, $\hat{\mathbf{p}}_2$, $\hat{\mathbf{p}}_3$ estimation in the same plot. Both resting nodes settle at a stationary PEB when $\hat{\mathbf{p}}_1$ is out of reach and thus not involved in any significant bistatic transmissions. When $\hat{\mathbf{p}}_1$ is close to a resting node though, the performances of the moving and the resting node improve. What is especially interesting is that their PEBs are almost equal when the nodes are in close vicinity of each other.

As \mathbf{p}_1 moves along the trajectory, the following situations arise:

- A-B: Not a single bistatic MPC reaches the mobile agent \mathbf{p}_1 , localization is purely monostatic. Cooperative, naive cooperative, and monostatic bounds are identical.
- B-C: Bistatic non line of sight (NLOS) paths between \mathbf{p}_2 and \mathbf{p}_1 occur, but it is only shortly before reaching C that the signal-to-noise ratio (SNR) of these paths becomes sufficient for meaningful contribution. This effect is best seen in the plot of error ellipses, whose major half-axes are smaller in the middle of B-D compared to the middle of A-B.
- C-F: \mathbf{p}_1 has LOS connection to \mathbf{p}_2 . The bistatic PEB performs rather poorly because of a lack of directional diversity in its relevant MPCs. Yet the bistatic contributions provide valuable horizontal position information, which monostatic contributions lack because of significant free-space path loss on the long line between D and E. The cooperative PEB has a local maximum when \mathbf{p}_1 is closest to \mathbf{p}_2 because relevant bistatic contributions are purely vertical there.
- F: LOS connection between \mathbf{p}_1 and \mathbf{p}_3 suddenly sets in and causes a vast drop in the bistatic PEB and thus also a slight increase of cooperative localization performance.
- G: LOS between \mathbf{p}_1 and \mathbf{p}_2 is lost and causes a jump in the bistatic PEB, but the cooperative PEB is barely affected because of said bistatic connection was already heavily damped by free-space path loss.
- G-I: This passage is similar to the C-F situation.

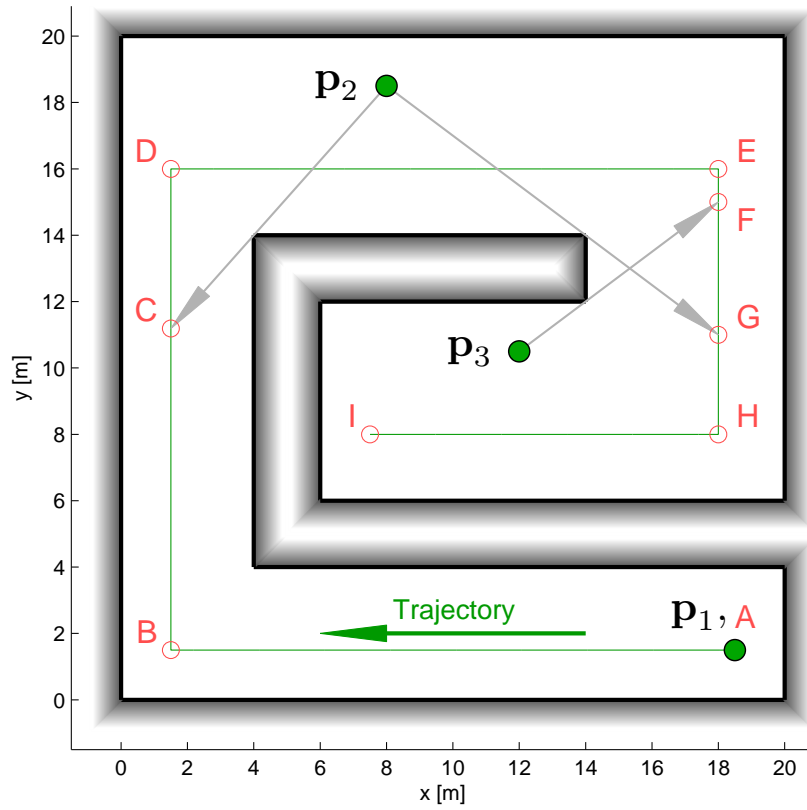


Figure 5.11: Agent p_1 travels through a complex indoor environment on a given trajectory. Resting nodes p_2 and p_3 allow for cooperative anchorless localization. Distinct trajectory points are marked with letters.

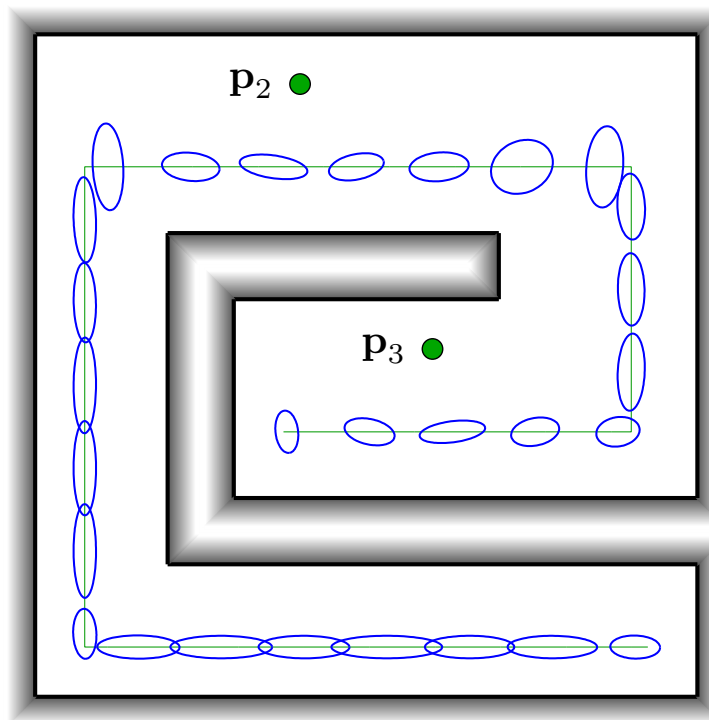


Figure 5.12: Enlarged (factor 50) error ellipses show directivity of the cooperative PEB.

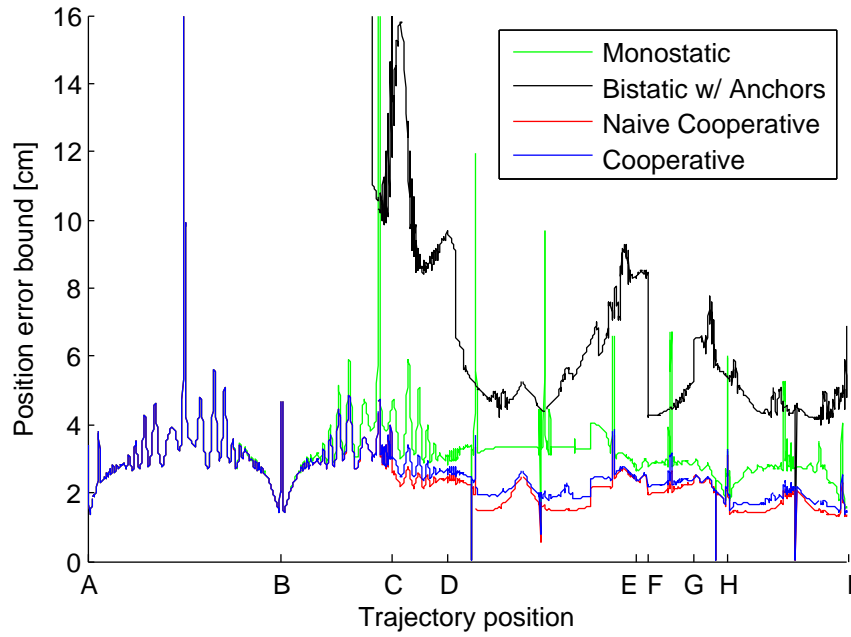


Figure 5.13: Several lower bounds for the position estimate $\hat{\mathbf{p}}_1$ of the moving agent.

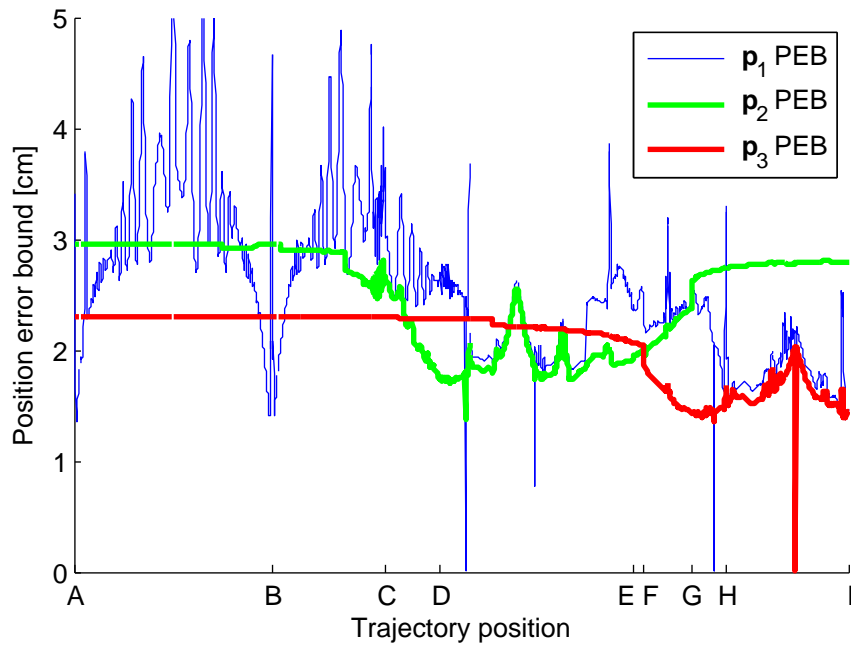


Figure 5.14: CRLBs of cooperative position estimates $\hat{\mathbf{p}}_1$, $\hat{\mathbf{p}}_2$, $\hat{\mathbf{p}}_3$ according to EFIM (5.26).

6

Conclusions

6.1 Summary

This thesis gives a thorough analysis of the performance limits of the cooperative multipath-assisted indoor navigation and tracking (Co-MINT) approach and all of its building blocks and intricacies.

- We introduced a notational framework that enables a mathematical treatment of multipath-assisted cooperative localization in diffuse multipath (DMP) and additive white Gaussian noise (AWGN).
- Gradients of multipath delays w.r.t. receiver (RX) and transmitter (TX) positions were identified as the central figures of room geometry influence on localization performance. Therefore, we developed a linear algebraic theory of virtual anchors (VAs) and introduced the notion of effective wall angle of a multipath component (MPC), a simple quantity that accounts for the influence of all walls involved in the reflection path of said MPC. Using the effective wall angle, we gave a concise general formula for spatial delay gradients.
- Because of its significance for Co-MINT, we obtained the Cramér-Rao lower bound (CRLB) for monostatic localization by deriving the corresponding equivalent Fisher information matrix (EFIM). The result is decomposed into the influence of room geometry via spatial delay gradients and Fisher information (FI) between signal model quantities estimated from the received signal. The latter is heavily impaired when pulses overlap.
- Since monostatic MPCs have very specific properties, we analytically investigated the contributions to localization for several arrangements and reflection orders.
- Numerical results of the monostatic position error bound (PEB) show that the approach has the potential to perform well but often suffers from severe path overlap problems.
- After a lengthy derivation, we obtained the CRLB of Co-MINT, which was the ultimate goal of this thesis. A well-structured EFIM shows the monostatic and bistatic contributions and the performance decrease due to position uncertainties during bistatic measurements. For a single agent, the result becomes equivalent to the monostatic EFIM.

- Numerical results of cooperative localization demonstrate how Co-MINT incorporates the benefits of monostatic and bistatic localization to compensate for their individual disadvantages. Results of three exemplary indoor arrangements shed light on many characteristics of the approach. CRLB values show that Co-MINT, despite being a very flexible approach, definitely has potential for accurate performance.

6.2 Outlook

The theoretical capabilities of Co-MINT are evident due to this thesis and the practicability was shown by Fröhle [16], but it is a long and winding road to a robust system that actually comes close to the derived CRLB. Implementation raises a lot of issues like node synchronisation, cooperation, data exchange, information loss due to unavoidably working with signal metrics rather than ideal continuous-time signals, feasibility and convergence of estimation algorithms, multimodal likelihood functions (LHFs), association of received signal peaks to the MPC model and tracking via Kalman filters. All of these problems are topics of ongoing research in several branches of information and communication technology, so at this point in time it is very hard to judge the feasibility of flexible and affordable Co-MINT implementations that perform robustly in the various fields of application.

Further theoretical progress could be possible within the presented mathematical framework of the Co-MINT CRLB. For instance, applying results from the algebraic field of the Euclidean group to the VA construction process could yield further insights and would probably enable a straightforward extension to three-dimensional case. Additionally, studying reciprocity properties of bistatic multipaths could allow for simplifications in the cooperative EFIM.

A

Appendix

A.1 Fisher Information among Signal Model Parameters

The following formulas denote matrices containing Fisher information (FI) among signal model parameters of a particular received signal $r_{m,j}(t)$. They are taken from [6] where the same signal model was used.

FI among propagation delays of multipath components (MPCs):

$$\begin{aligned} [\Phi_{m,j}(\boldsymbol{\tau}_{m,j}, \boldsymbol{\tau}_{m,j})]_{k,k'} &= \mathbb{E}_{\mathbf{r}|\boldsymbol{\theta}} \left\{ -\frac{\partial^2 \ln f(\mathbf{r}_{m,j} | \boldsymbol{\tau}_{m,j}, \boldsymbol{\alpha}_{m,j})}{\partial \tau_{m,j}^{(k)} \partial \tau_{m,j}^{(k')}} \right\} \\ &= \frac{2}{N_0} \cdot \Re \left(\alpha_{m,j}^{(k)} (\alpha_{m,j}^{(k')})^* \right) \cdot w_{m,j}^{(k)} w_{m,j}^{(k')} \cdot \frac{\partial^2 R_s(\tau_{m,j}^{(k)} - \tau_{m,j}^{(k')})}{\partial \tau_{m,j}^{(k)} \partial \tau_{m,j}^{(k')}} \end{aligned} \quad (\text{A.1})$$

FI among path amplitudes of MPCs (equal for \Re and \Im):

$$\begin{aligned} [\Phi_{m,j}(\Re \boldsymbol{\alpha}_{m,j}, \Re \boldsymbol{\alpha}_{m,j})]_{k,k'} &= [\Phi_{m,j}(\Im \boldsymbol{\alpha}_{m,j}, \Im \boldsymbol{\alpha}_{m,j})]_{k,k'} \\ &= \mathbb{E}_{\mathbf{r}|\boldsymbol{\theta}} \left\{ -\frac{\partial^2 \ln f(\mathbf{r}_{m,j} | \boldsymbol{\tau}_{m,j}, \boldsymbol{\alpha}_{m,j})}{\partial \Re \alpha_{m,j}^{(k)} \partial \Re \alpha_{m,j}^{(k')}} \right\} = \frac{2}{N_0} \cdot w_{m,j}^{(k)} w_{m,j}^{(k')} \cdot R_s(\tau_{m,j}^{(k)} - \tau_{m,j}^{(k')}) \end{aligned} \quad (\text{A.2})$$

FI among propagation delay and path amplitude of MPCs:

$$\begin{aligned} [\Phi_{m,j}(\boldsymbol{\tau}_{m,j}, \Re \boldsymbol{\alpha}_{m,j})]_{k,k'} &= \mathbb{E}_{\mathbf{r}|\boldsymbol{\theta}} \left\{ -\frac{\partial^2 \ln f(\mathbf{r}_{m,j} | \boldsymbol{\tau}_{m,j}, \boldsymbol{\alpha}_{m,j})}{\partial \tau_{m,j}^{(k)} \partial \Re \alpha_{m,j}^{(k')}} \right\} \\ &= \frac{2}{N_0} \cdot \Re \alpha_{m,j}^{(k)} \cdot w_{m,j}^{(k)} w_{m,j}^{(k')} \cdot \frac{\partial R_s(\tau_{m,j}^{(k)} - \tau_{m,j}^{(k')})}{\partial \tau_{m,j}^{(k)}} \\ [\Phi_{m,j}(\boldsymbol{\tau}_{m,j}, \Im \boldsymbol{\alpha}_{m,j})]_{k,k'} &= \frac{2}{N_0} \cdot \Im \alpha_{m,j}^{(k)} \cdot w_{m,j}^{(k)} w_{m,j}^{(k')} \cdot \frac{\partial R_s(\tau_{m,j}^{(k)} - \tau_{m,j}^{(k')})}{\partial \tau_{m,j}^{(k)}} \end{aligned} \quad (\text{A.3})$$

We used the autocorrelation function $R_s(\tau)$ of the transmitted signal pulse [6]

$$R_s(\tau) = \int_{\mathbb{R}} s(t)s(t-\tau)dt . \quad (\text{A.4})$$

A.2 Proof: Magnitude times Direction Form of Monostatic Gradient (3.32)

We can transform the initial formula

$$\frac{\partial \tau_{j,j}^{(k)}}{\partial \mathbf{p}_j} = \frac{1}{c} \left(\mathbf{e} \left(\phi_{j,j}^{(k)} \right) - \mathbf{e} \left((-1)^{L_{j,j}^{(k)}} \cdot \phi_{j,j}^{(k)} + 2\gamma_{j,j}^{(k)} \right) \right)$$

into a form that gives a product of magnitude times unity vector as result. We are observing one fixed MPC and therefore temporarily drop the $\square_{j,j}^{(k)}$ indexing for clarity:

$$\frac{\partial \tau}{\partial \mathbf{p}_j} = \frac{1}{c} \left(\mathbf{e}(\phi) - \mathbf{e}((-1)^L \cdot \phi + 2\gamma) \right)$$

By applying the basic theorems [32] for subtraction of trigonometric functions

$$\begin{aligned} \cos(u) - \cos(v) &= 2\sin\left(\frac{v+u}{2}\right)\sin\left(\frac{v-u}{2}\right) \\ \sin(u) - \sin(v) &= 2\cos\left(\frac{u+v}{2}\right)\sin\left(\frac{u-v}{2}\right) \end{aligned}$$

to each dimension, we can further transform this to

$$\begin{aligned} \frac{\partial \tau}{\partial \mathbf{p}_j} &= \frac{1}{c} \begin{pmatrix} \cos(\phi) - \cos((-1)^L \phi + 2\gamma) \\ \sin(\phi) - \sin((-1)^L \phi + 2\gamma) \end{pmatrix} \\ &= \frac{1}{c} \begin{pmatrix} 2\sin\left(\frac{1}{2} \left(((-1)^L + 1) \phi + 2\gamma \right) \right) \sin\left(\frac{1}{2} \left(((-1)^L - 1) \phi + 2\gamma \right) \right) \\ 2\cos\left(\frac{1}{2} \left(((-1)^L + 1) \phi + 2\gamma \right) \right) \sin\left(-\frac{1}{2} \left(((-1)^L - 1) \phi + 2\gamma \right) \right) \end{pmatrix} \\ &= \frac{2}{c} \sin\left(\frac{(-1)^L - 1}{2} \cdot \phi + \gamma\right) \cdot \begin{pmatrix} \sin\left(\frac{(-1)^L + 1}{2} \cdot \phi + \gamma\right) \\ -\cos\left(\frac{(-1)^L + 1}{2} \cdot \phi + \gamma\right) \end{pmatrix} \\ &= \frac{2}{c} \sin\left(\frac{(-1)^L - 1}{2} \cdot \phi + \gamma\right) \cdot \underbrace{\begin{pmatrix} 0 & 1 \\ -1 & 0 \end{pmatrix}}_{=\mathbf{Rot}(-\frac{\pi}{2})} \mathbf{e}\left(\frac{(-1)^L + 1}{2} \cdot \phi + \gamma\right) \\ &= \frac{2}{c} \sin\left(\gamma + \frac{(-1)^L - 1}{2} \cdot \phi\right) \cdot \mathbf{e}\left(\gamma - \frac{\pi}{2} + \frac{(-1)^L + 1}{2} \cdot \phi\right) \\ &= \frac{2}{c} \sin\left(\gamma - \mathbb{1}_{2\mathbb{Z}+1}(L) \cdot \phi\right) \cdot \mathbf{e}\left(\gamma - \frac{\pi}{2} + \mathbb{1}_{2\mathbb{Z}}(L) \cdot \phi\right) \end{aligned}$$

where we used indicator functions to distinguish between even and odd orders L . An obvious case-by-case analysis yields the convenient formula (in full notation again)

$$\frac{\partial \tau_{j,j}^{(k)}}{\partial \mathbf{p}_j} = \begin{cases} \frac{2}{c} \sin\left(\gamma_{j,j}^{(k)}\right) \cdot \mathbf{e}\left(\gamma_{j,j}^{(k)} + \phi_{j,j}^{(k)} - \frac{\pi}{2}\right) & \text{if } L_{j,j}^{(k)} \text{ is even} \\ \frac{2}{c} \sin\left(\gamma_{j,j}^{(k)} - \phi_{j,j}^{(k)}\right) \cdot \mathbf{e}\left(\gamma_{j,j}^{(k)} - \frac{\pi}{2}\right) & \text{if } L_{j,j}^{(k)} \text{ is odd} \end{cases} .$$

Bibliography

- [1] G. Fischer, *Lineare Algebra*, ser. Vieweg-Studium : Grundkurs Mathematik. Vieweg, 2005.
- [2] Y. Shen, H. Wymeersch, and M. Win, “Fundamental limits of wideband localization - Part II: Cooperative networks,” *Information Theory, IEEE Transactions on*, vol. 56, no. 10, pp. 4981–5000, 2010.
- [3] M. Win and H. Wymeersch, “High-definition location-awareness,” <https://docs.google.com/file/d/0B2eVVx8g6qeGcndqZjZSZ2dqTzQ/>, IEEE Communications Society, IEEE WCNC 2009 tutorial talk, April 2009, [Online; accessed 19-Dec-2013].
- [4] Y. Shen and M. Win, “Fundamental limits of wideband localization; Part I: A general framework,” *Information Theory, IEEE Transactions on*, vol. 56, no. 10, pp. 4956–4980, 2010.
- [5] J. Karedal, S. Wyne, P. Almers, F. Tufvesson, and A. Molisch, “A measurement-based statistical model for industrial ultra-wideband channels,” *Wireless Communications, IEEE Transactions on*, vol. 6, no. 8, pp. 3028–3037, 2007.
- [6] K. Witrals and P. Meissner, “Performance bounds for multipath-assisted indoor navigation and tracking (MINT),” in *Communications (ICC), 2012 IEEE International Conference on*, 2012, pp. 4321–4325.
- [7] A. Molisch, “Ultra-wide-band propagation channels,” *Proceedings of the IEEE*, vol. 97, no. 2, pp. 353–371, 2009.
- [8] L. Yang and G. Giannakis, “Ultra-wideband communications: An idea whose time has come,” *Signal Processing Magazine, IEEE*, vol. 21, no. 6, pp. 26–54, 2004.
- [9] P. Meissner and K. Witrals, “Analysis of position-related information in measured UWB indoor channels,” in *Antennas and Propagation (EUCAP), 2012 6th European Conference on*, 2012, pp. 6–10.
- [10] J. Andersen, J. Nielsen, G. Pedersen, G. Bauch, and M. Herdin, “Room electromagnetics,” *Antennas and Propagation Magazine, IEEE*, vol. 49, no. 2, pp. 27–33, 2007.
- [11] A. Richter, *Estimation of Radio Channel Parameters: Models and Algorithms*. ISLE, 2005.
- [12] Y. Shen and M. Win, “Fundamental limits of wideband localization accuracy via Fisher information,” in *Wireless Communications and Networking Conference, 2007. WCNC 2007. IEEE*, 2007, pp. 3046–3051.
- [13] —, “On the use of multipath geometry for wideband cooperative localization,” in *Global Telecommunications Conference, 2009. GLOBECOM 2009. IEEE*, 2009, pp. 1–6.
- [14] Y. Kuang, K. Astrom, and F. Tufvesson, “Single antenna anchor-free UWB positioning based on multipath propagation,” in *Communications (ICC), 2013 IEEE International Conference on*, June 2013, pp. 5814–5818.

- [15] P. Meissner, T. Gigl, and K. Witrisal, "UWB sequential Monte Carlo positioning using virtual anchors," in *Indoor Positioning and Indoor Navigation (IPIN), 2010 International Conference on*, Sept 2010, pp. 1–10.
- [16] M. Froehle, E. Leitinger, P. Meissner, and K. Witrisal, "Cooperative multipath-assisted indoor navigation and tracking (Co-MINT) using UWB signals," in *Communications Workshops (ICC), 2013 IEEE International Conference on*, 2013, pp. 16–21.
- [17] P. Meissner and K. Witrisal, "Multipath-assisted single-anchor indoor localization in an office environment," in *Systems, Signals and Image Processing (IWSSIP), 2012 19th International Conference on*, 2012, pp. 22–25.
- [18] P. Meissner, E. Leitinger, M. Lafer, and K. Witrisal, "Real-Time Demonstration System for Multipath-Assisted Indoor Navigation and Tracking (MINT)," in *IEEE ICC 2014 Workshop on Advances in Network Localization and Navigation (ANLN)*, 2014, accepted.
- [19] E. Leitinger, M. Froehle, P. Meissner, and K. Witrisal, "Multipath-Assisted Maximum-Likelihood Indoor Positioning using UWB Signals," in *IEEE ICC 2014 Workshop on Advances in Network Localization and Navigation (ANLN)*, 2014, accepted.
- [20] F. Montorsi, S. Mazuelas, G. Vitetta, and M. Win, "On the performance limits of map-aware localization," *Information Theory, IEEE Transactions on*, vol. 59, no. 8, pp. 5023–5038, 2013.
- [21] S. Van de Velde, H. Wymeersch, P. Meissner, K. Witrisal, and H. Steendam, "Cooperative multipath-aided indoor localization," in *Wireless Communications and Networking Conference (WCNC), 2012 IEEE*, April 2012, pp. 3107–3111.
- [22] Y. Shen, S. Mazuelas, and M. Win, "Network navigation: Theory and interpretation," *Selected Areas in Communications, IEEE Journal on*, vol. 30, no. 9, pp. 1823–1834, 2012.
- [23] S. Kay, *Fundamentals of Statistical Signal Processing: Estimation Theory. Volume 1*, ser. Prentice Hall signal processing series. Prentice Hall PTR, 1993.
- [24] H. Godrich, A. Haimovich, and R. Blum, "Target localization accuracy gain in MIMO radar-based systems," *Information Theory, IEEE Transactions on*, vol. 56, no. 6, pp. 2783–2803, 2010.
- [25] C. Ruedisser, "The impact of clock offset on multipath-assisted indoor localization," Master's thesis, Graz University of Technology, 2014.
- [26] R. Liepins, "Acoustic source localization with a single microphone using reflected signals," Master's thesis, Graz University of Technology, 2013.
- [27] H. Van Trees, *Detection, Estimation, and Modulation Theory*, ser. Detection, Estimation, and Modulation Theory. Wiley, 2004, no. Teil 1.
- [28] P. Bello, "Characterization of randomly time-variant linear channels," *Communications Systems, IEEE Transactions on*, vol. 11, no. 4, pp. 360–393, 1963.
- [29] A. Molisch, *Wireless Communications*, ser. Wiley - IEEE. Wiley, 2010.
- [30] M. Lafer, "Real-time multipath-assisted indoor tracking and feature detection," Master's thesis, Graz University of Technology, 2014.

- [31] Y. Shen and M. Win, “Effect of path-overlap on localization accuracy in dense multipath environments,” in *Communications, 2008. ICC '08. IEEE International Conference on*, 2008, pp. 4197–4202.
- [32] H. Bartsch, *Taschenbuch mathematischer Formeln*. Fachbuchverl. Leipzig im Carl-Hanser-Verlag, 2007.
- [33] H. Coxeter, *Introduction to Geometry*, ser. Wiley Classics Library. Wiley, 1989.